Distribution Agreement

In presenting this thesis or dissertation as a partial fulfillment of the requirements for an advanced degree from Emory University, I hereby grant to Emory University and its agents the non-exclusive license to archive, make accessible, and display my thesis or dissertation in whole or in part in all forms of media, now or hereafter known, including display on the world wide web. I understand that I may select some access restrictions as part of the online submission of this thesis or dissertation. I retain all ownership rights to the copyright of the thesis or dissertation. I also retain the right to use in future works (such as articles or books) all or part of this thesis or dissertation.

Signature:

_____ _____

Rachel B. Kozlowski Date

Effect of Site-Specific Heating on Enzyme Catalysis

By

Rachel B. Kozlowski

Doctor of Philosophy

Chemistry

_____

R. Brian Dyer

Advisor

_____

Vincent Conticello

Committee Member

_____

James Kindt

Committee Member

Accepted:

_____

Lisa A. Tedesco, Ph.D.

Dean of the James T. Laney School of Graduate Studies

_____

Date

Effect of Site-Specific Heating on Enzyme Catalysis

By

Rachel B. Kozlowski

B.S., Campbell University, 2014

Advisor: R. Brian Dyer, Ph.D.

An abstract of

A dissertation submitted to the Faculty

of the James T. Laney School of Graduate Studies of Emory University

in partial fulfillment of the requirements for the degree of

Doctor of Philosophy

in Chemistry

2020

Abstract

Effect of Site-Specific Heating on Enzyme Catalysis

By Rachel B. Kozlowski

Enzymes are nature's catalysts. All enzymes have an energy landscape, and they lower those activation barriers to accelerate rates under biological temperature, pH, and concentrations. Enzymes have both static and dynamic components. Static "snapshots" of enzymes can be obtained with x-ray crystallography or cryo-electron microscopy to observe how the enzyme is folded, but a structural component alone cannot predict how enzymes move during catalysis. Although the contribution of protein motions to enzymatic catalysis has been heavily studied, experimental evidence reporting on the exact role of enzyme dynamics in catalysis is lacking. We seek to understand if dynamic motions in enzymes during catalysis represent preferred energy pathways. To interrogate the connection between enzyme catalytic motions and preferred energy pathways, dihydrofolate reductase (DHFR), which has a known network of coupled motions, is conjugated to gold nanoparticles (AuNPs). Enzyme activity is monitored as a function of the protein attachment site (distance to/from the network of coupled motions) on the AuNP, as well as of the timescale of laser pulsing. DHFR activity when attached to the AuNP close to the network (on the FG loop) is accelerated when excited by the pulsed lasers. When attached near the cofactor binding site network residue E101 (on an Alpha Helix), turnover is accelerated to a lesser extent. There is a greater degree of acceleration with fs pulsed laser than with ns pulses in both mutants. There is no rate acceleration when the AuNP is attached to DHFR away from the network (Distal Mutant) or via the histidine tag (also away from the network). There is no rate acceleration observed for any DHFR-AuNP attachment site with the continuous wave excitation. When the excitation timescale is fast enough, the heat flow into the protein affects the enzyme motions in catalysis, which are likely the motions involved in the search for reactive conformations, and the heat eventually thermalizes after these motions take place. This dissertation demonstrates a useful methodology for studying protein motions in enzyme catalysis, allowing us to investigate energy pathways in catalysis.

Effect of Site-Specific Heating on Enzyme Catalysis

By

Rachel B. Kozlowski

B.S., Campbell University, 2014

Advisor: R. Brian Dyer, Ph.D.

A dissertation submitted to the Faculty

of the James T. Laney School of Graduate Studies of Emory University

in partial fulfillment of the requirements for the degree of

Doctor of Philosophy

in Chemistry

2020

Acknowledgements:

To Micah, for your unwavering support throughout the years and driving me to continue moving forward.

To my friends Amanda, Tamra, and Cassie, for being a source of encouragement and reminding me that life is not all about graduate school.

To my family, for being there for me, loving me, and supporting me always.

To my lab colleagues, for your discussions and support.

To Brian Dyer, for helping me grow and develop into the scientist (and person) I am today.

Table of Contents

List of Figures

List of Tables

Chapter 1 – Introduction

Section 1-1: Enzyme Dynamics, Catalysis, and Motions

Enzymes are nature's catalysts; they are proteins that quickly catalyze chemical reactions that normally would require extreme conditions. Catalysts increase the rate of a reaction, which is performed by both synthetic catalysts and enzymes. Synthetic catalysts operate under quite extreme conditions: high temperature, low pH, high concentrations, or high-pressure conditions. Enzymes catalyze chemical reactions under biological conditions, including ambient temperature, neutral pH, low concentrations, and atmospheric pressure.[1, 2]

In general, enzymes catalyze reactions 7-9 orders of magnitude faster than the respective reaction would occur free in solution.[3, 4] Enzymes work by lowering the activation barrier of the reaction of interest. Commonly, a standard reaction coordinate using transition state theory is imagined when thinking about enzyme catalysis (**Figure 1.1**). Transition state theory is 2-dimensional, accounting only for the energy and reaction coordinate.[5] Peak minima represent low energy states during enzymatic catalysis, and peak maxima represent energy barriers to achieve catalysis. This 2D depiction of energy over the course of catalysis shows the quantitative value for the observed energy barriers. This is known as transition state theory, which is the basis for rational design of enzymes.

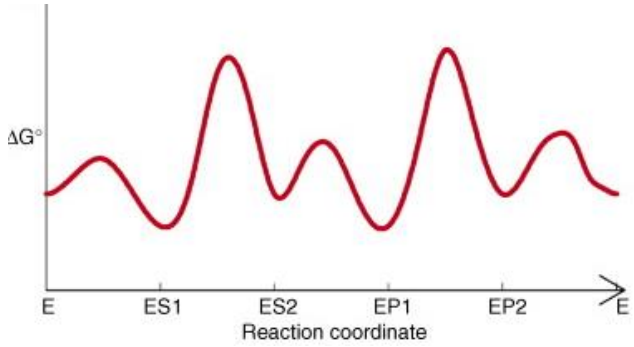

Figure 1.1: 2-Dimensional Energy Landscape.

A standard 2-dimensional energy landscape showing the coordinate of reactants to intermediates to products. This diagram shows the reaction energy versus the reaction coordinate.[6]

When looking at past and current attempts at designing enzymes, it is clear that transition state theory does not completely describe the landscape of enzyme catalysis.[7-9] For example, in *de novo* enzyme design, enzymes are rationally designed to perform a specific function. The idea is that if we know and understand the structure of enzymes and their theoretical catalytic mechanism, then we should be able to design an enzyme that catalyzes the reaction of interest with relatively similar catalytic efficiency. Computationally designed enzymes to catalyze many reactions, including Diels-Alder reactions,[7] Kemp elimination,[8] and retro-aldol reactions,[9] have been explored. In each of these studies, the rate of reactions with the computationally designed enzymes were far less efficient than even the slowest of naturally occurring enzymes.[4, 7-9] So, what is missing? Why can we not create efficient enzymes based on structural knowledge and catalytic mechanism alone? Enzymes are inherently flexible and dynamic biomolecules. During catalysis, enzymes are constantly changing conformations on all timescales from femtoseconds to even seconds (**Figure 1.2**).[10-20] The current computational programs have

not yet been able to successfully predict enzyme motions. In order to effectively design enzymes, we must first understand enzyme dynamics and investigate the limitations of the standard 2-dimensional reaction coordinate.

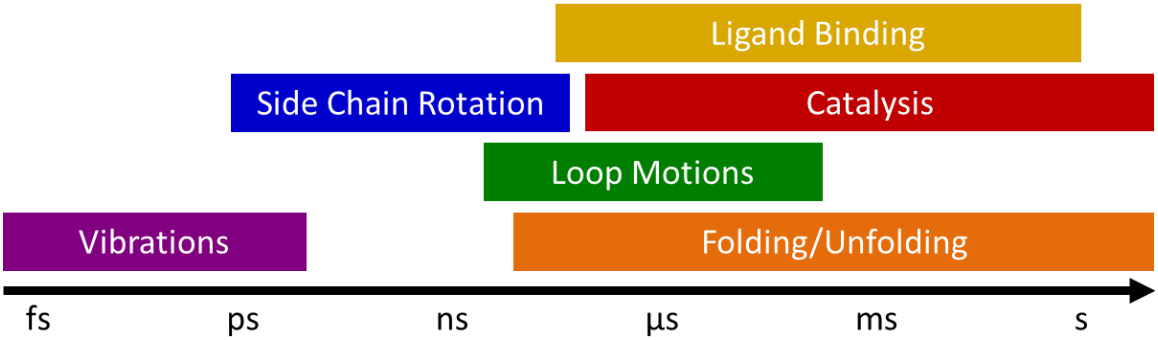

Figure 1.2: Timescales of Motions in Enzymes.

During catalysis, there are many types of enzyme motions over all timescales. The fastest motions are vibration, occurring on the femtosecond to picosecond timescale. Other motions leading up to catalysis, such as side chain rotation, ligand binding, folding and unfolding, and loop motions, occur on the picosecond to seconds timescale.

It is clear that a 2-dimensional reaction coordinate does not account for conformational changes in the enzyme and substates during protein motion. To describe reaction coordinates more accurately, a 3-dimensional reaction coordinate can be exploited (**Figure 1.3**).[6, 11, 21] Because protein motions and conformational changes of the enzyme during catalysis can affect the energetic mechanism of catalysis, the catalytic pathways are better represented with this multidimensional energy landscape. This type of energy landscape demonstrates that there are both local and absolute minima and maxima. Enzyme catalysis involves a search for reactive conformations, where the enzyme has to move and

change conformationally in order to accept the cofactor and substrate reactants and turn them over to products.[1, 12] Not every enzyme conformation results in the most efficient rate of reaction, as the enzyme can get stuck in a local minimum of energy. Therefore, these preferred energy pathways demonstrate that enzymes themselves must be dynamic in nature, as they change conformations and optimize their structure to best catalyze reactions.[22]

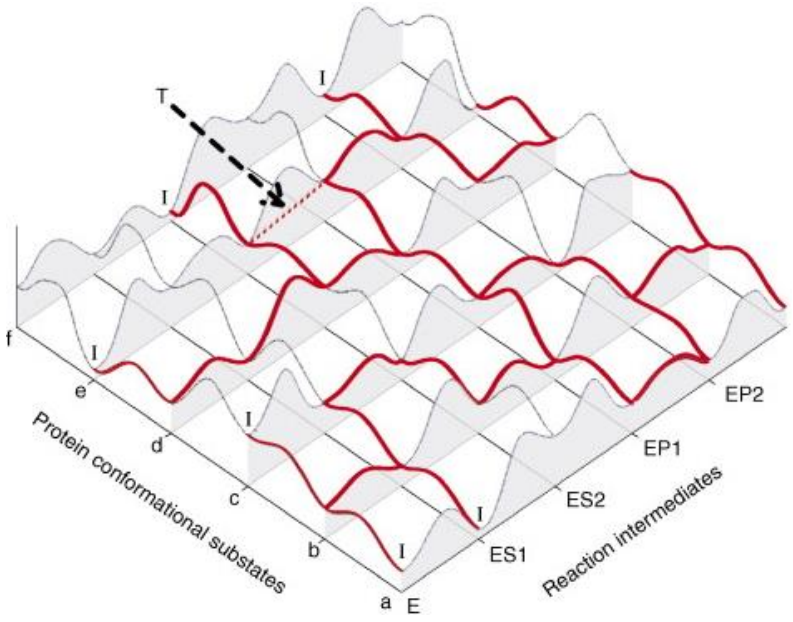

Figure 1.3: Multidimensional Energy Landscape.

An example of a 3-dimensional energy landscape showing a network for potential routes to catalyze the reaction of reactants to intermediates to products. A 2-dimensional energy landscape only considers the energy itself and the reaction coordinate. The 3-dimensional energy landscape also considers the conformations of the enzyme and the potential substates during catalysis.

There are two types of motions in proteins that affect catalysis: Motions directly related to the chemistry step, and motions that facilitate the approach to the transition state. In the first type, the motions are dependent on the transition state chemistry that the enzyme catalyzes. For enzymes that undergo small atom transfers, such as hydride and other atom transfers, the motions modulate the donor and acceptor distance across the transition state on the femtosecond to picosecond timescale.[21-23] Other enzymes catalyze bond breaking at the transition state, so the motions are coupled to this bond breaking step.[21, 22] In both cases, these motions are inherently directly coupled to catalysis on ultrafast timescales. In the second type of motions, the motions are involved in the search for the reactive conformation.[1, 12, 24] These motions are slower, on the nanosecond to microsecond timescale, and they modulate the population of Michaelis state conformations rather than directly coupled to catalysis. These motions affect catalysis downstream, rather than directly.[1, 12, 24] To study preferred energy pathways in enzymes, we use dihydrofolate reductase (DHFR) as a model system. The structure of DHFR has been extensively researched, and several groups have postulated that the motions in DHFR are coupled to catalysis. However, the evidence for this idea of coupled motions is indirect, and the view is not accepted by everyone.

Section 1-2: Dihydrofolate Reductase

Section 1-2.1: Overview of Enzyme and Function

Dihydrofolate reductase (DHFR) catalyzes the reduction of the substrate 7,8-dihydrofolate (DHF) to 5,6,7,8-tetrahydrofolate (THF) through the oxidation of the

cofactor nicotinamide adenine dinucleotide phosphate (NADPH) to $NADP^+$ (**Figure 1.4**). Catalysis occurs via the hydride transfer from NADPH to DHF and a concomitant proton transfer.[11-14, 17-20, 25-27] This process is the main source of cellular THF, which supports the production of purine nucleotide bases, thymidylate, and consequently amino acids.[17, 19] Excessive THF in cells causes a rapid proliferation of cells that causes many types of diseases, including cancer, bacterial infections, rheumatoid arthritis, and malaria.[13, 17, 18, 26, 27] Thus, DHFR has become a drug target, where drugs such as methotrexate have been developed to inhibit the enzyme and stop the production of THF and therefore DNA synthesis.[18, 28, 29]

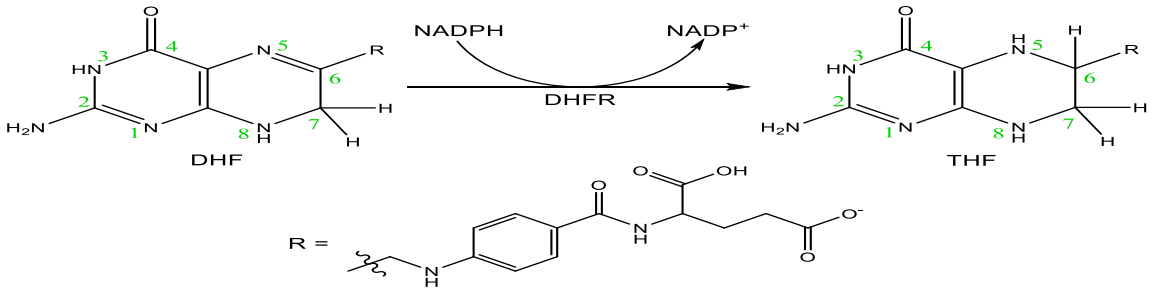

Figure 1.4: DHFR Reaction Scheme.

DHFR catalyzes the reaction of DHF to THF through the oxidation of the cofactor NADPH to $NADP^+$.

In this dissertation, we use *E. coli* DHFR, which is the variant used in the studies involving the network of coupled motions.[10, 26] DHFR is a small, flexible enzyme with 160 amino acid residues that form eight β-sheets (βA through βH) and four α-helices that are connected by three loops that form the catalytic subdomain.[17, 18] The loops in DHFR are the most flexible portions of the protein and are postulated to move the most during

catalysis through crystallographic structures of starting and intermediate states. The three loops, shown in **Figure 1.5**, are termed the Met20 loop, βF-βG loop (known as the FG loop), and βG-βH loop (known as the GH loop). The Met20 loop is named after its center methionine residue at position 20. This loop has the largest conformational changes in the protein, as it opens and closes over the active site during catalysis. The FG loop connects the 6th (F) and 7th (G) β-sheets. Lastly, the GH loop connects the 7th (G) and 8th (H) β-sheets.[17, 18, 30]

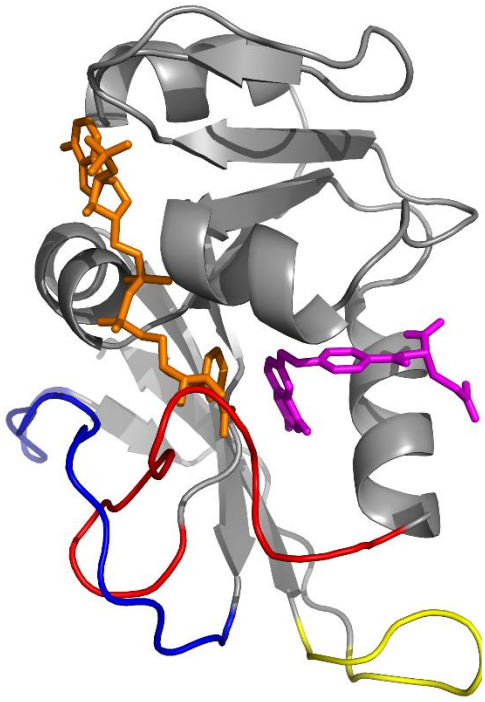

Figure 1.5: DHFR Structure.

The structure of DHFR. The three loops are highlighted here. Red = Met20 loop. Blue = FG loop. Yellow = GH loop. The cofactor and substrate are shown in their respective binding pockets. Orange = NADPH. Pink = DHF. PDB: 1RX2.

Section 1-2.2: Catalytic Cycle

The three loops in DHFR are important for enzyme catalysis, as they are flexible and have large conformational changes.[18] During the catalytic cycle, the Met20 loop undergoes the largest conformational changes. There are three conformations during DHFR catalysis, and they are all designated based on the conformation of the Met20 loop: open, closed, and occluded (**Figure 1.6**).[30, 31] The open conformation describes the enzyme free in solution with no substrate or cofactor bound in the binding pockets. In this conformation, the Met20 loop is completely open, ready to accept the ligands in the active site. Once the ligands bind to DHFR, catalysis begins, and the enzyme conformationally changes between the closed and occluded states of the enzyme.[18]

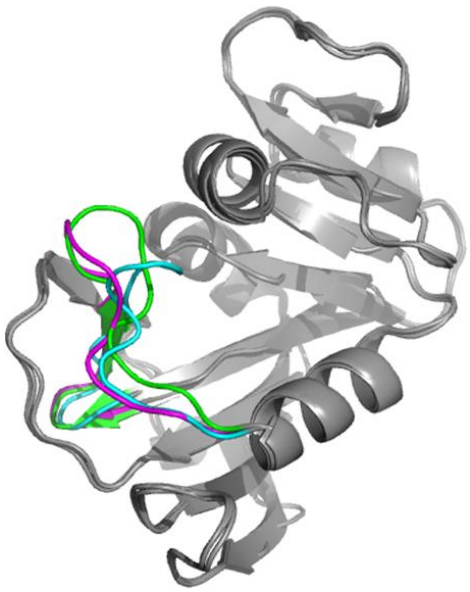

Figure 1.6: DHFR Conformations During Catalysis.

DHFR undergoes conformational changes during catalysis, and the conformation change of the Met20 loop is the largest structural change in the enzyme. Pink = Open, Green = Closed, and Blue = Occluded. PDB codes – Open: 1RA9; Closed: 1RX2; Occluded: 1RX7.

X-ray crystallographic studies have shown that there are five major intermediates that the enzyme cycles through during catalysis (**Figure 1.7**).[14, 18] The conformation of the protein is dictated by the ligands bound or unbound in the binding sites, including NADPH, $NADP^+$, DHF, and THF. When the reactant substrate DHF and cofactor NADPH bind in the active site, the enzyme adopts the closed conformation. In this closed conformation, the loop is closed over the active site, preventing the cofactor from unbinding. When DHFR reduces the substrate DHF to THF and oxidizes the cofactor NADPH to $NADP^+$, the enzyme changes to the occluded conformation. Here, the loop shifts to sterically hinder the cofactor nicotinamide ring from binding to the active site, thus causing the reacted $NADP^+$ to unbind from the active site. New, unreacted cofactor binds in the NADPH binding pocket, which then causes the product, THF, to be released and a conformational change to occur, going from the occluded conformation back to the closed conformation. This allows new, unreacted substrate to bind, cycling back to the start of the catalytic cycle. The rate-limiting step of the catalytic cycle is the product (THF) release step.[14, 18, 20, 32]

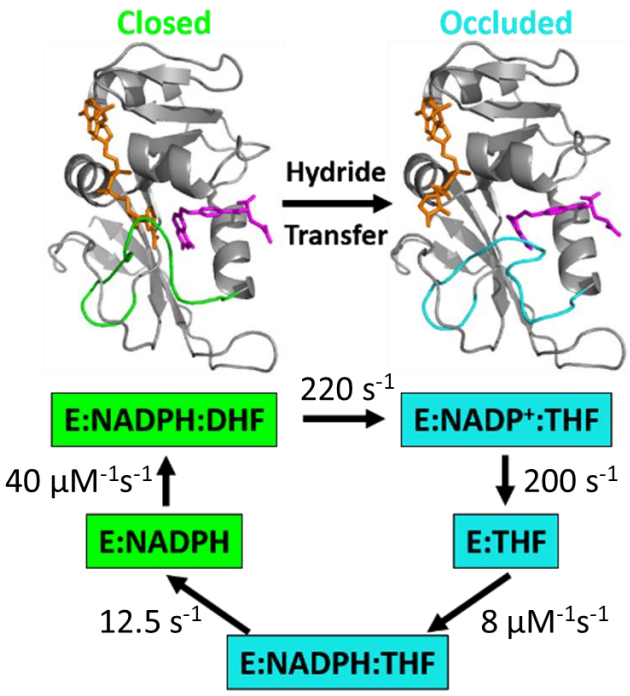

Figure 1.7: Catalytic Cycle of DHFR.

DHFR interconverts between the closed and occluded conformations during enzymatic catalysis. The conformation depends on the types of ligands bound or unbound. The Met20 loop is highlighted in the structure. Orange structure = NADPH, pink structure = DHF.

The activity of DHFR can be monitored spectroscopically by following the oxidation of NADPH to $NADP^+$. The UV/Vis absorbance spectra of the reduced and oxidized forms of the cofactor are shown in **Figure 1.8**. The reduced form of the cofactor, NADPH, has two clear peaks in the UV/Vis absorbance spectrum: One at 260 nm and one at 340 nm. When NADPH is oxidized to form $NADP^+$, the peak at 340 nm disappears completely, and the peak at 260 nm grows in stronger. Thus, the absorbance at 340 nm can be monitored over time to watch the 340 nm absorbance decay as NADPH is oxidized to $NADP^+$.

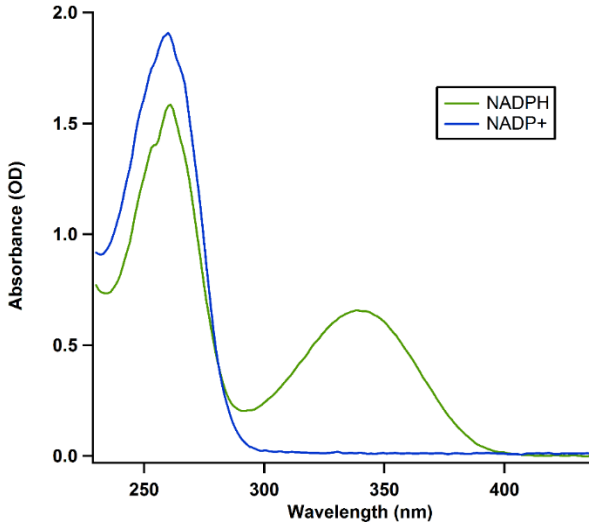

Figure 1.8: UV/Vis Absorbance Spectra of NADPH and $NADP^+$.

Reduced cofactor, NADPH, has clear absorbance peaks centered at 260 nm and 340 nm. When NADPH is oxidized to $NADP^+$, the 260 nm peak grows in more, and the 340 nm peak disappears.

Section 1-2.3: Networks of Coupled Motions

Molecular Dynamics (MD) simulations and mutational studies have indirectly shown that there are motions across the enzyme that are coupled to each other during catalysis.[12, 26, 33] Mutations directly on any of these residues changes the motions such that they become catalytically unfavorable, thus halting the activity of the enzyme. For example, when G121 is mutated to any other amino acid residue, DHFR has no or minimal activity.[25, 31, 34, 35] Additionally, increasing the rigidity of the Met20 loop with a diproline mutation (N23PP) causes activity "knock-out".[10, 25] The "knock-out" mutant of DHFR was determined to stop millisecond fluctuations in the protein using heteronuclear single-quantum correlation (HSQC). HSQC looks at the correlation between ^1H and ^{15}N chemical shifts in amino acid residues. In WT DHFR, HSQC spectra of the closed and occluded states show a different correlation between residues postulated to be part of the network of

coupled motions (**Figure 1.9a**). Conversely, the HSQC spectra of the N23PP/S148A "knock-out" mutant demonstrate that there is very little to no difference in correlation between the closed and occluded states (**Figure 1.9b**). This indicates that there is no shift from the closed to the occluded conformation throughout the chemical step of catalysis in the "knock-out" mutant of DHFR.[10]

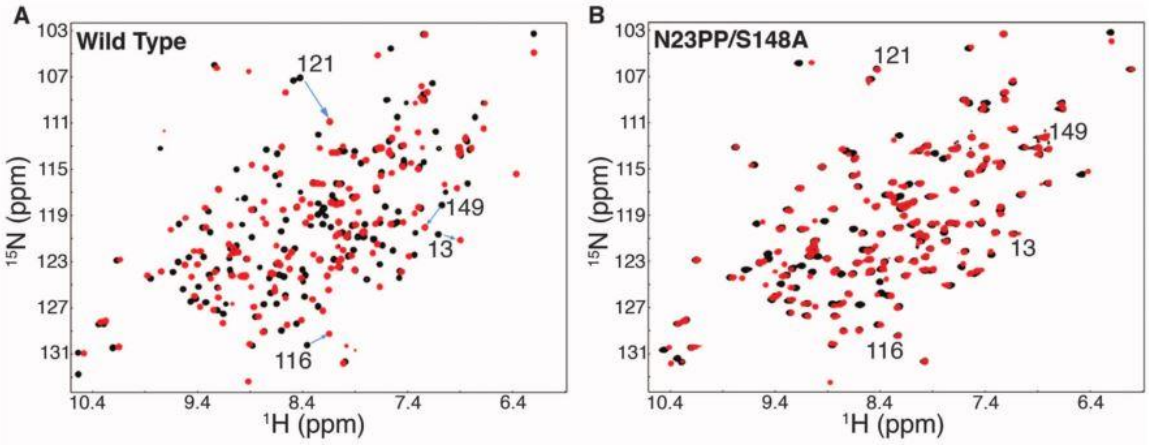

Figure 1.9: HSQC NMR of DHFR and "Knock-Out Mutant".

a. HSQC spectrum of WT DHFR. **b.** HSQC spectrum of "knock-out" mutant. As the hydride transfer step takes place, there is a change from the closed to the occluded state in WT DHFR. However, there is no conformation change seen in the "knock-out" mutant with the HSQC NMR studies.[10]

However, not all parties agree on the interpretation of the results from the "knock-out" mutant studies. The second hypothesis is led by Warshel, et al., which states that the catalytic function of DHFR does not depend on enzyme dynamics. Here, the claim is that electrostatic preorganization leads to the catalytic effects.[2, 15, 36-38] This has been studied with computational efforts using empirical valence bond (EVB) simulations. EVB

simulations examine the activation barrier of WT DHFR and DHFR mutants, which are then related to the catalytic effects on the enzyme (**Figure 1.10**).

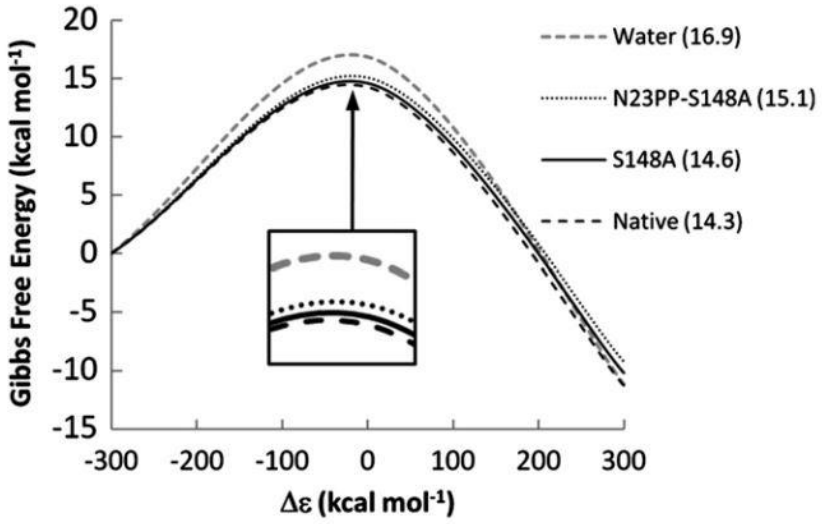

Figure 1.10: Average EVB Free-Energy Profiles.

The average EVB free-energy profiles for a reference reaction (water), WT DHFR (Native), the "knock-out" mutant (N23PP-S148A), and an S148A mutant. The values in the parenthesis represent the activation barrier in kcal/mol.[15]

EVB simulations show that the mutation effect from the "knock-out" mutant on catalysis is likely due to the free-energy reorganization change rather than protein dynamics. The free-energy barrier for WT DHFR is 14.3 kcal/mol, which is slightly lower than the free-energy barrier for the N23PP-S148A mutant of 15.1 kcal/mol (**Figure 1.10**). This slight difference in free-energy barrier was interpreted to be large enough to indicate that the effect of the mutation was likely caused by free-energy change instead of dynamic effects.[15] While there is controversy on the mechanism of this "knock-out" process, it is clear that certain residues in DHFR impact catalysis.[10, 15, 16, 26, 39]

In DHFR, MD simulations and mutational studies have postulated that the network of coupled motions coupled to catalysis involve the active site residue I14 and the distal residues M42, G121, and F125.[26, 35, 39-41] MD simulations are used to determine the correlation of motions on a timescale of 10 ns (**Figure 1.11**).[26] Here, the correlated residues are observed over a select time period of 10 ns. The residues that show negative correlation are moving at the same time, but they are moving in opposite directions. Conversely, the residues showing positive correlation are moving in the same direction at the same point in time. The correlation of the residues is a correlation of motions at the same time, not necessarily during catalysis itself. However, these MD simulations allow the ability of determining which residues might be coupled during catalysis, and thus which residues should be further studied to determine the components of the network of coupled motions in DHFR.[12, 26]

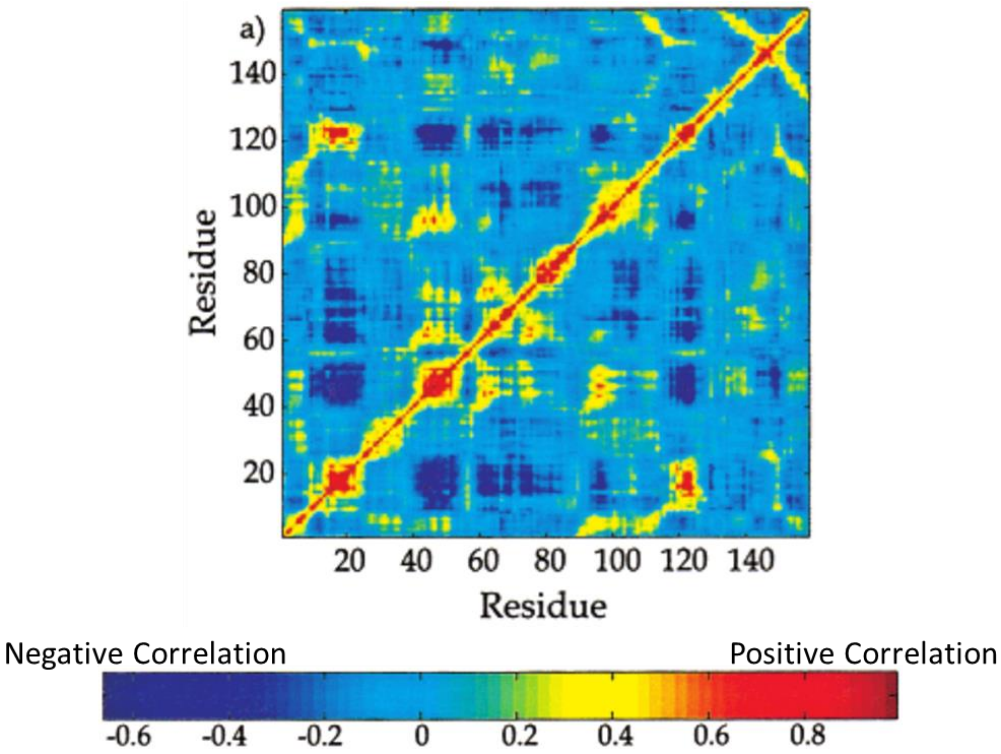

Figure 1.11: Molecular Dynamics Simulation of DHFR.

MD simulations show which residues are correlated in time over a simulation time of 10 ns. Dark blue spots represent negative correlation, where the residues are moving in opposite directions from each other at the same time. Bright red spots represent positive correlation, where the residues are moving in the same direction at the same time.[12]

Experimentally, residues predicted to be correlated via MD simulations can be further investigated with mutational studies and temperature-dependent kinetic isotope effects. For example, G121 and I14 were thought to be part of this network of coupled motions.[35] Single mutants were designed (G121V and I14A), as well as a double mutant (G121V-I14A). Temperature-dependent Arrhenius plots of the intrinsic kinetic isotope effects (KIEs) were made and used to examine the additive effect of the activation energies (**Figure 1.12**). In these studies, NADPH is labeled with either H (hydrogen) or T (tritium) at the 4R position.[35, 41]

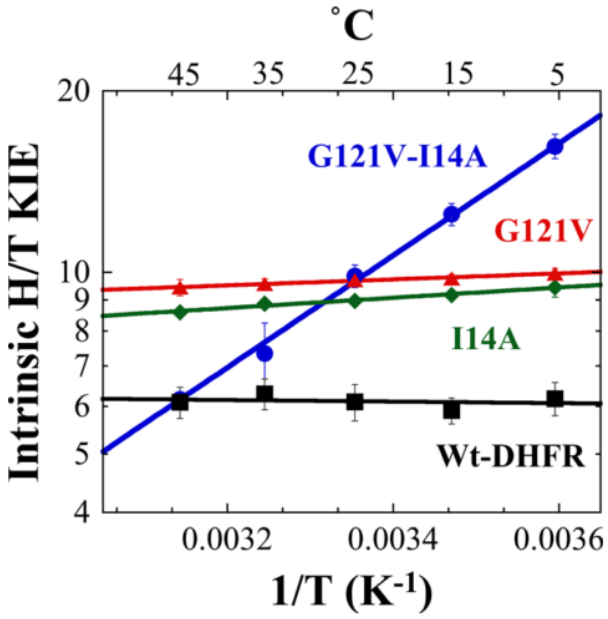

Figure 1.12: Temperature-Dependent KIEs.

Mutational studies and temperature-dependent Arrhenius plots of the intrinsic KIEs. Black is WT DHFR. Green and red are the single mutants of the residues of interest, I14A and G121V. Blue is the double mutant, G121V-I14A.[35]

A typical Arrhenius analysis plots the natural log of the rate of reaction versus the inverse of the temperature, where the slope is proportional to the activation energy:

$$ln(k) = \frac{1}{T} \cdot \frac{-\Delta E_a}{R} + ln(A)$$

Here, the analysis is performed with the below equation:

$$\ln(KIE) = ln\left(\frac{k_l}{k_h}\right) = \frac{1}{T} \cdot \frac{-\left(E_{a,l} - E_{a,h}\right)}{R} + ln\left(\frac{A_l}{A_h}\right)$$

The rate constants k_l and k_h represent the rate constants of light NADPH (H labeled) and heavy NADPH (T labeled). The constant A is the pre-exponential factor. WT DHFR has essentially no intrinsic KIE when monitoring the temperature dependence, and the single mutants (G121V and I14A) have minimal KIE as well. This means that the activation energy of the light reaction is approximately the same as the activation energy of the heavy reaction, which is also approximately the same activation energy as WT DHFR. However, when looking at the difference in rate for heavy and light NADPH with the double mutant (G121V-I14A), a very large KIE is observed over the measured temperature range. This means that the activation energy of the light reaction is much lower than the activation energy of the heavy reaction. This synergistic effect of activation energy seen for the potential correlation of G121 and I14, indirectly confirms that both of these residues are likely part of the network of coupled motions in DHFR.[35, 41]

The network of coupled motions in DHFR is postulated to be coupled to catalysis, particularly correlated to the hydride transfer reaction. Thus, it is possible that inputting energy, in the form of heat, close to this network will cause an acceleration in enzyme activity. The network of coupled motions is a way by which the energy on distal parts of the protein can be funneled to the active site, where the reaction is catalyzed. Adding energy into proteins excites vibrations, such as local bond vibrations or collective motions of loops.[42-44] Consequently, adding heat site-specifically near the network of coupled motions could excite vibrations that occur during catalysis and allow the protein to access more conformations and thus more reactive ones, speeding up the rate of catalysis. This site-specific addition of heat can be accomplished by conjugating the enzyme to a biologically compatible heater molecule, such as gold nanoparticles.

Section 1-3: Gold Nanoparticles

Gold nanoparticles (AuNPs) are of particular interest in biological and biomedical applications due to their biocompatibility, ability to be surface functionalized, and can be used as a delivery vehicle. [45-56] AuNPs are biocompatible due to their inert nature in the body. Drugs, proteins, and other molecules can be conjugated to AuNPs, and the AuNPs can be delivered into the body safely. [51-53] This conjugation is possible due to the AuNP's ability to be surface functionalized. AuNPs are synthesized with many types of capping ligands, including citrate, thiols, phosphines, amines, polyethylene glycol chains, and carboxylates (**Figure 1.13**).[57, 58] AuNPs are very commonly synthesized via the citrate reduction method, which caps the AuNPs with citrate.[59] Citrate is a very weak binding ligand that allows simple displacement through addition of a compound containing a thiol, which will strongly outcompete AuNP binding sites due to the covalent bonding of gold and sulfur.[60, 61]

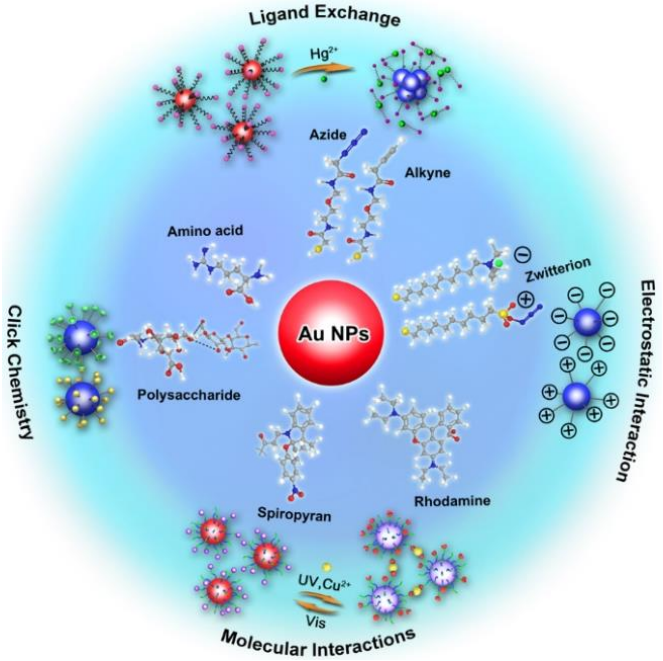

Figure 1.13: Types of Surface Chemistry for AuNP Functionalization.

In addition to citrate, there are many capping ligands to allow the functionalization of AuNPs. This allows for the binding of small molecules and has application in biochemical analysis.[58]

Further, AuNPs have strong optical absorption and short-lived excited states, and, therefore, are highly efficient at converting light into heat on short timescales. This efficiency is due to the surface plasmon resonance (SPR) property of AuNPs, which is the collective oscillation of electrons on the nanoparticle surface.[61, 62] SPR absorbance of AuNPs is dependent on the size of the particle and the dielectric constant of the functionalized molecule on the AuNP surface. In spherical 50 nm AuNPs or smaller, the SPR absorbance band is centered in the green region (520-550 nm) of the visible spectrum. Above 50 nm diameter, the SPR band redshifts to over 550 nm and higher (**Figure 1.14a**).[55] The SPR band greatly redshifts, into the near IR, with nanomaterials such as nanorods

(AuNRs), which are elongated nanospheres; the larger the aspect ratio (rod length to seed diameter), the redder the SPR peak (**Figure 1.14b**).[61]

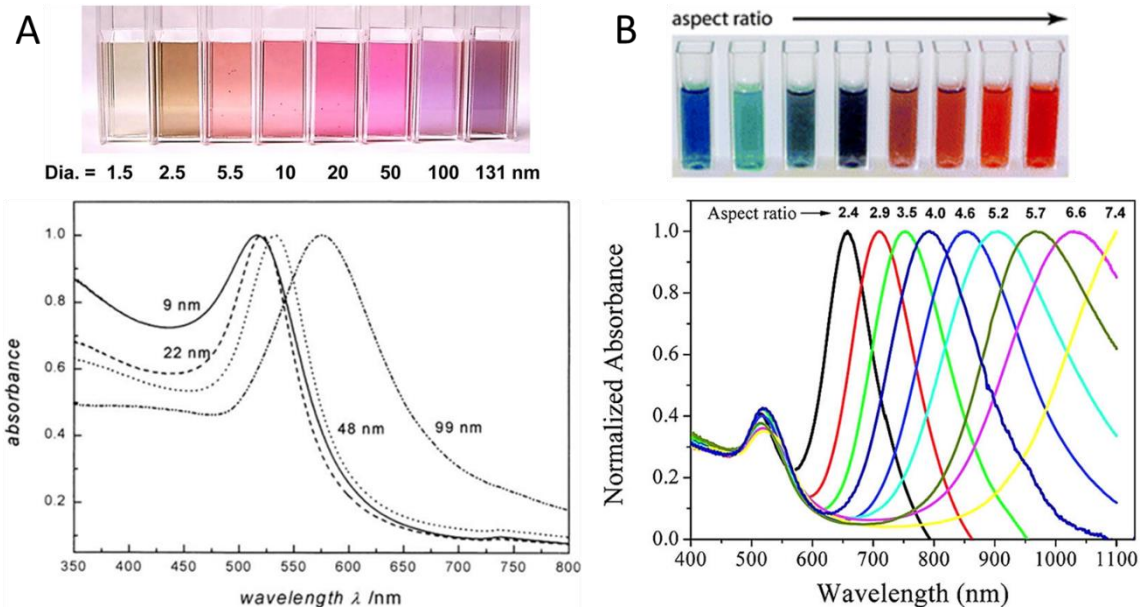

Figure 1.14: UV/Vis Absorption Spectra of Various AuNPs and AuNRs.

A. Samples and UV/Vis absorption spectra of AuNPs of various diameters. Very small AuNPs are much more brown in color than larger AuNPs. The 5-50 nm regime is most widely used, and these AuNPs are all pink in color. The SPR band for all small AuNPs (up to 50 nm in diameter) is between 520 and 550 nm. As AuNPs get larger, their SPR band greatly redshifts, and the 100 nm diameter AuNPs have an SPR band centered close to 600 nm.[55] **B.** AuNRs are elongated AuNPs, and their colors vary much more widely than different diameters of nanospheres. There are two SPR bands in AuNRs, one for the seed diameter, and one of the length of the AuNR. The smaller peak around 530 nm is the SPR band for the seed diameter. The much larger and far redshifted SPR band is for the AuNR length. This SPR band shifts into the near IR and further. The longer the AuNR in comparison to the seed diameter (higher aspect ratio), the more redshifted the SPR band.[61]

Section 1-4: Bioconjugation of Proteins and Gold Nanoparticles

Section 1-4.1: Methods of Bioconjugation

There are many methods for attaching proteins to AuNPs (**Figure 1.15**).[61] The two most common types of protein bioconjugation to AuNPs are electrostatic interactions and covalent bonding. The first method uses electrostatic interactions to adsorb the protein to the AuNP surface (**Figure 1.15i**). This is a noncovalent bonding mechanism, and the interactions are specific to the type of capping ligand on the AuNP and the charge of the protein. Examples of electrostatic interactions are hydrogen bonding, Van der Waals, or hydrophobic interactions.[63-65] Electrostatic interactions are not specific, so the protein interacts with the AuNP in many different orientations. The protein can rotate to different orientations, and the protein can also adopt different conformations depending on the protein's structure and surface charge.

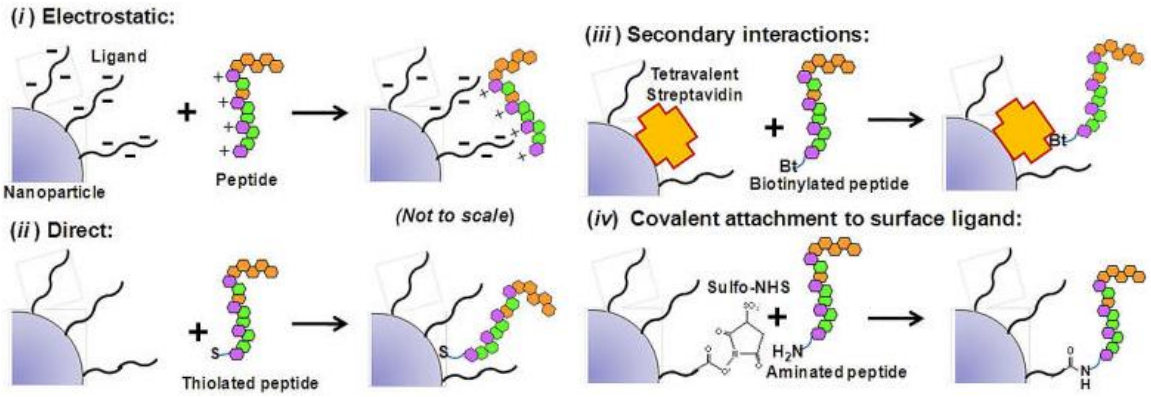

Figure 1.15: Common Methods for Protein-AuNP Bioconjugation.

Proteins are bioconjugated to AuNPs using several different methods. The most common methods are electrostatic interactions (i) and covalent bonding directly to the AuNP surface (ii).[61]

The second type of protein bioconjugation method is covalent binding (**Figure 1.15ii**).[61] Proteins can be covalently bound to AuNPs if the protein contains a functional group that can covalently bind to gold or the capping ligand on the AuNP.[66-69] A common method for covalent attachment is through the use of a surface exposed cysteine residue, either intrinsic to the protein or engineered. Covalent binding is site-specific, as the sulfur of the thiol covalently binds to the surface of the AuNP with a bond strength of 40-50 kcal/mol.[70] This type of conjugation to beneficial because it allows for the control of protein orientation and ensures that the active site will not be blocked or facing the AuNP surface. Covalent conjugation also allows for a tighter bond between the protein and the AuNP.[61]

Section 1-4.2: Characterization of Protein-Gold Nanoparticle Conjugates

Many different techniques have been applied to characterize protein-AuNP conjugates, and these techniques can be broken into 4 main types: Scattering techniques, thermal analysis, microscopy, and spectroscopy (**Figure 1.16**).[71]

Figure 1.16: Experimental Methods for Protein-AuNP Bioconjugates.

There are four broad types of techniques currently used to characterize protein-AuNP conjugates.[71]

The scattering techniques include Dynamic Light Scattering (DLS), differential centrifugal sedimentation (DCS), and zeta potential analysis. These techniques can be used to determine the size of the particle and conjugate, as well as the charge of the AuNPs, which gives information regarding the stability and properties of the protein-AuNP conjugates.[68, 72] Thermal gravimetric analysis (TGA) is a technique that monitors mass differences over changes in temperature. TGA can be used to determine the number of ligands on the AuNP surface, but the process is extremely sample consumptive, requiring 1-10 mg of sample for each run. Further, the technique also relies on assumptions and a model of the AuNP shape. Microscopy methods such as transmission electron microscopy (TEM), scanning tunneling microscopy (STM), and atomic force microscopy (AFM) are generally far less sample consumptive. However, these methods are not quantitative regarding the amount of ligand on the AuNP surface.[71]

The spectroscopic methods include UV/Vis absorption spectroscopy, infrared (IR) spectroscopy, nuclear magnetic resonance (NMR), electron spin resonance (ESR), and circular dichroism (CD). Of these techniques, UV/Vis absorption is by far the most common method to characterize protein-AuNP bioconjugates.[55, 61, 68, 71-74] As described earlier in Section 1-3, AuNPs have a SPR band. This band is sensitive to the AuNP size, AuNP shape, and the dielectric constant of the capping molecules. For example, AuNPs capped by citrate have a different SPR band than AuNPs capped by protein. This shift in the SPR band is easily and commonly detected through UV/Vis absorption spectroscopy.[71]

Section 1-5: Energy Flow from AuNPs to Proteins Through Photoexcitation

Photoexcitation of AuNPs provides high amounts of energy to be dissipated to the surrounding solution, including bioconjugated enzyme (**Figure 1.17**).[75] When AuNPs are photoexcited with resonant photons (at the SPR band), the electrons on the surface of the AuNP start resonating, which results in a rapid non-equilibrium heating. Electron-electron scattering results in relaxation on the sub-picosecond timescale, rapidly increasing the surface temperature of the gold.[76, 77] Electron-phonon coupling causes energy exchange between the previously excited electrons and the lattice phonons. This nonradiative decay process converts electronic excitation to vibrational energy through the excited phonons. Coupling of phonons with the solvent or capping ligand, including protein vibrations, causes cooling of the AuNP surface. Finally, after several hundred picoseconds post photoexcitation, phonon-phonon coupling results in heat dissipation from the lattice to the surroundings.[75]

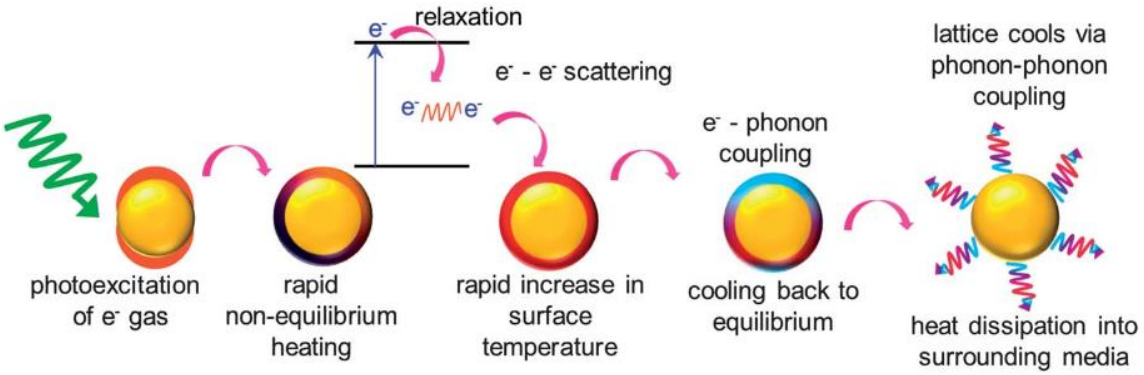

Figure 1.17: Photothermal Characteristics of AuNPs.

The stepwise process of heat dissipation from a photoexcitation resonant with the SPR band of an AuNP. AuNPs are photoexcited with optical light, and they convert the optical energy to thermal energy, which is eventually dissipated to the surroundings.[75]

For the system described in this dissertation, a 527 nm photon contains an energy of 227 kJ/mol, while the activation barrier of DHFR is approximately 75 kJ/mol (see Section 5-2.1). Of course, a lot of the photon's energy is dissipated into the surroundings, but we hypothesize that the enzyme can couple the energy to DHFR's active site via the network of coupled motions. The timescale of excitation and enzyme motions will dictate the heating effects, as the heat must be input into the enzyme on a timescale comparable or faster than the enzyme motions themselves so that excitation of the coupled motions outcompete the energy dissipation. Since energy dissipation in proteins is known to occur on a timescale of at least 100s of ps[42, 78-80] and the MD simulations on DHFR show that correlated motions exist on a timescale of up to at least 10 ns,[12] the laser excitation here must be on a similar timescale. Another consideration is the timescale of energy dissipation from the AuNPs, which is known to have a timescale of 10s of ps to 400 ps depending on the size of the AuNP or gold nanorod and the capping ligands. For an enzyme-15 nm AuNP system, the energy dissipation time will likely be on the slower end of the range.

In general, all proteins have an energy landscape,[6, 14, 21] and the usual implication of rate acceleration is a consequence of lowering the transition barrier. However, if the catalytic landscape is rough, such that there are multiple peaks and valleys, some of the population could become trapped in local minima that have high barriers to reaction. The input of heat into a specific part of the enzyme structure might help transfer the population to more reactive conformations, or basins on the landscape from which the transition barrier is much lower. Thus, if this is the case, we are speeding up the search for reactive

conformations by pushing the system from trapped unreactive state by the site-specific addition of energy.

Section 1-6: Chapter 1 References

1. Nagel, Z. D.; Klinman, J. P., Tunneling and dynamics in enzymatic hydride transfer. *Chem. Rev.* **2006,** *106* (8), 3095-3118.

2. Warshel, A.; Sharma, P. K.; Kato, M.; Xiang, Y.; Liu, H. B.; Olsson, M. H. M., Electrostatic basis for enzyme catalysis. *Chem. Rev.* **2006,** *106* (8), 3210-3235.

3. Wolfenden, R.; Snider, M. J., The Depth of Chemical Time and the Power of Enzymes as Catalysts. *Accounts Chem Res* **2001,** *34* (12), 938-945.

4. Bar-Even, A.; Noor, E.; Savir, Y.; Liebermeister, W.; Davidi, D.; Tawfik, D. S.; Milo, R., The Moderately Efficient Enzyme: Evolutionary and Physicochemical Trends Shaping Enzyme Parameters. *Biochemistry* **2011,** *50* (21), 4402-4410.

5. Callender, R.; Dyer, R. B., The Dynamical Nature of Enzymatic Catalysis. *Acc. Chem. Res.* **2015,** *48* (2), 407-413.

6. Swint-Kruse, L.; Fisher, H. F., Enzymatic reaction sequences as coupled multiple traces on a multidimensional landscape. *Trends Biochem. Sci.* **2008,** *33* (3), 104-112.

7. Siegel, J. B.; Zanghellini, A.; Lovick, H. M.; Kiss, G.; Lambert, A. R.; Clair, J. L. S.; Gallaher, J. L.; Hilvert, D.; Gelb, M. H.; Stoddard, B. L.; Houk, K. N.; Michael, F. E.; Baker, D., Computational Design of an Enzyme Catalyst for a Stereoselective Bimolecular Diels-Alder Reaction. *Science* **2010,** *329* (5989), 309-313.

8. Rothlisberger, D.; Khersonsky, O.; Wollacott, A. M.; Jiang, L.; DeChancie, J.; Betker, J.; Gallaher, J. L.; Althoff, E. A.; Zanghellini, A.; Dym, O.; Albeck, S.; Houk, K. N.; Tawfik, D. S.; Baker, D., Kemp elimination catalysts by computational enzyme design. *Nature* **2008,** *453* (7192), 190-5.

9. Jiang, L.; Althoff, E. A.; Clemente, F. R.; Doyle, L.; Rothlisberger, D.; Zanghellini, A.; Gallaher, J. L.; Betker, J. L.; Tanaka, F.; Barbas, C. F.; Hilvert, D.; Houk, K. N.; Stoddard, B. L.; Baker, D., De novo computational design of retro-aldol enzymes. *Science* **2008,** *319* (5868), 1387-1391.

10. Bhabha, G.; Lee, J.; Ekiert, D. C.; Gam, J.; Wilson, I. A.; Dyson, H. J.; Benkovic, S. J.; Wright, P. E., A dynamic knockout reveals that conformational fluctuations influence the chemical step of enzyme catalysis. *Science* **2011,** *332* (6026), 234-238.

11. Hammes-Schiffer, S.; Benkovic, S. J., Relating protein motion to catalysis. *Annu. Rev. Biochem.* **2006,** *75*, 519-541.

12. Radkiewicz, J. L.; Brooks III, C. L., Protein Dynamics in Enzymatic Catalysis: Exploration of Dihydrofolate Reductase. *J. Am. Chem. Soc.* **2000,** *122*, 225-231.

13. Wang, Z.; Singh, P.; Czekster, C. M.; Kohen, A.; Schramm, V. L., Protein Mass-Modulated Effects in the Catalytic Mechanism of Dihydrofolate Reductase: Beyond Promoting Vibrations. *J. Am. Chem. Soc.* **2014,** *136* (23), 8333-8341.

14. Boehr, D. D.; McElheny, D.; Dyson, H. J.; Wright, P. E., The dynamic energy landscape of dihydrofolate reductase catalysis. *Science* **2006,** *313* (5793), 1638-42.

15. Adamczyk, A. J.; Cao, J.; Kamerlin, S. C. L.; Warshel, A., Catalysis by dihydrofolate reductase and other enzymes arises from electrostatic preorganization, not conformational motions. *Proc. Natl. Acad. Sci. U.S.A.* **2011,** *108* (34), 14115-14120, S14115/1-S14115/8.

16. Loveridge, E. J.; Behiry, E. M.; Guo, J.; Allemann, R. K., Evidence that a dynamic knockout' in Escherichia coli dihydrofolate reductase does not affect the chemical step of catalysis. *Nat. Chem.* **2012,** *4* (4), 292-297.

17. Fierke, C. A.; Johnson, K. A.; Benkovic, S. J., Construction and evaluation of the kinetic scheme associated with dihydrofolate reductase from Escherichia coli. *Biochemistry* **1987,** *26* (13), 4085-92.

18. Sawaya, M. R.; Kraut, J., Loop and subdomain movements in the mechanism of Escherichia coli dihydrofolate reductase: crystallographic evidence. *Biochemistry* **1997,** *36* (3), 586-603.

19. Oyeyemia, O. A.; Sours, K. M.; Leeb, T.; Resing, K. A.; Ahnb, N. G.; Klinman, J. P., Temperature dependence of protein motions in a thermophilic dihydrofolate reductase and its relationship to catalytic efficiency. *Proc. Natl. Acad. Sci. U.S.A.* **2010,** *107*, 10074-10079.

20. Luk, L. Y. P.; Loveridge, E. J.; Allemann, R. K., Protein motions and dynamic effects in enzyme catalysis. *Phys. Chem. Chem. Phys.* **2015,** *17*, 30817-30827.

21. Benkovic, S. J.; Hammes, G. G.; Hammes-Schiffer, S., Free-energy landscape of enzyme catalysis. *Biochemistry* **2008,** *47* (11), 3317-3321.

22. Klinman, J. P.; Kohen, A., Hydrogen tunneling links protein dynamics to enzyme catalysis. *Annu. Rev. Biochem.* **2013,** *82*, 471-496.

23. Singh, P.; Abeysinghe, T.; Kohen, A., Linking Protein Motion to Enzyme Catalysis. *Molecules* **2015,** *20* (1), 1192-1209.

24. Wang, L.; Goodey, N. M.; Benkovic, S. J.; Kohen, A., The role of enzyme dynamics and tunnelling in catalysing hydride transfer: studies of distal mutants of dihydrofolate reductase. *Philos T Roy Soc B* **2006,** *361* (1472), 1307-1315.

25. Fan, Y.; Cembran, A.; Ma, S.; Gao, J., Connecting Protein Conformational Dynamics with Catalytic Function As Illustrated in Dihydrofolate Reductase. *Biochemistry* **2013,** *52*, 2036-2049.

26. Agarwal, P. K.; Billeter, S. R.; Rajagopalan, P. T. R.; Benkovic, S. J.; Hammes-Schiffer, S., Network of Coupled Promoting Motions in Enzyme Catalysis. *Proc. Natl. Acad. Sci. U.S.A.* **2002,** *99*, 2794-2799.

27. Arora, K.; Brooks, C. L., III, Multiple intermediates, diverse conformations, and cooperative conformational changes underlie the catalytic hydride transfer reaction of dihydrofolate reductase. *Top. Curr. Chem.* **2013,** *337* (Dynamics in Enzyme Catalysis), 165-188.

28. Williams, J. W.; Morrison, J. F.; Duggleby, R. G., Methotrexate, a high-affinity pseudosubstrate of dihydrofolate reductase. *Biochemistry* **1979,** *18* (12), 2567-73.

29. R, F. P.; J, W. R., Methotrexate assay by enzymatic inhibition, with use of centrifugal analyzer. *Clin. Chem.* **1977,** *23* (11), 2139-2141.

30. Arora, K.; Brooks, C. L., Functionally Important Conformations of the Met20 Loop in Dihydrofolate Reductase are Populated by Rapid Thermal Fluctuations. *JACS* **2009,** *131* (15), 5642-5647.

31. Boehr, D. D.; Schnell, J. R.; McElheny, D.; Bae, S.-H.; Duggan, B. M.; Benkovic, S. J.; Dyson, H. J.; Wright, P. E., A distal mutation perturbs dynamic amino acid networks in dihydrofolate reductase. *Biochemistry* **2013,** *52* (27), 4605-4619.

32. Venkitakrishnan, R. P.; Zaborowski, E.; McElheny, D.; Benkovic, S. J.; Dyson, H. J.; Wright, P. E., Conformational changes in the active site loops of dihydrofolate reductase during the catalytic cycle. *Biochemistry* **2004,** *43* (51), 16046-16055.

33. Rod, T. H.; Charles L. Brooks, I., How Dihydrofolate Reductase Facilitates Protonation of Dihydrofolate. *J. Am. Chem. Soc.* **2003,** *125*, 8718-8719.

34. Gekko, K.; Kunori, Y.; Takeuchi, H.; Ichihara, S.; Kodama, M., Point mutations at glycine-121 of Escherichia coli dihydrofolate reductase: important roles of a flexible loop in the stability and function. *J. Biochem.* **1994,** *116* (1), 34-41.

35. Singh, P.; Francis, K.; Kohen, A., Network of Remote and Local Protein Dynamics in Dihydrofolate Reductase Catalysis. *ACS Catal.* **2015,** *5* (5), 3067-3073.

36. Olsson, M. H. M.; Parson, W. W.; Warshel, A., Dynamical contributions to enzyme catalysis: Critical tests of a popular hypothesis. *Chem. Rev.* **2006,** *106* (5), 1737-1756.

37. Pisliakov, A. V.; Cao, J.; Kamerlin, S. C. L.; Warshel, A., Enzyme millisecond conformational dynamics do not catalyze the chemical step. *Proc. Natl. Acad. Sci. U.S.A.* **2009,** *106* (41), 17359-17364.

38. Warshel, A.; Bora, R. P., Perspective: Defining and quantifying the role of dynamics in enzyme catalysis. *J Chem Phys* **2016,** *144* (18), 180901.

39. Agarwal, P. K., Role of Protein Dynamics in Reaction Rate Enhancement by Enzymes. *J. Am. Chem. Soc.* **2005,** *127* (43), 15248-15256.

40. Agarwal, P. K.; Billeter, S. R.; Rajagopalan, P. T. R.; Benkovic, S. J.; Hammes-Schiffer, S., Network of Coupled Promoting Motions in Enzyme Catalysis. *Proc. Natl. Acad. Sci. U.S.A.* **2002,** *99*, 2794-2799.

41. Singh, P.; Sen, A.; Francis, K.; Kohen, A., Extension and Limits of the Network of Coupled Motions Correlated to Hydride Transfer in Dihydrofolate Reductase. *JACS* **2014,** *136* (6), 2575-2582.

42. Leitner, D. M., Energy flow in proteins. *Annu. Rev. Phys. Chem.* **2008,** *59*, 233-59.

43. Leitner, D. M., Vibrational energy transfer in helices. *Phys. Rev. Lett.* **2001,** *87* (18).

44. Lian, T.; Locke, B.; Kholodenko, Y.; Hochstrasser, R. M., Energy Flow from Solute to Solvent Probed by Femtosecond IR Spectroscopy: Malachite Green and Heme Protein Solutions. *J. Phys. Chem.* **1994,** *98* (45), 11648-11656.

45. Ghosh, P.; Han, G.; De, M.; Kim, C. K.; Rotello, V. M., Gold nanoparticles in delivery applications. *Adv. Drug Del. Rev.* **2008,** *60* (11), 1307-1315.

46. Medintz, I. L.; Uyeda, H. T.; Goldman, E. R.; Mattoussi, H., Quantum dot bioconjugates for imaging, labelling and sensing. *Nature Mater.* **2005,** *4*, 435-446.

47. Grzelczak, M. P.; Danks, S. P.; Klipp, R. C.; Belic, D.; Zaulet, A.; Kunstmann-Olsen, C.; Bradley, D. F.; Tsukuda, T.; Viñas, C.; Teixidor, F.; Abramson, J. J.; Brust, M., Ion Transport across Biological Membranes by Carborane-Capped Gold Nanoparticles. *ACS Nano* **2017,** *11* (12), 12492-12499.

48. Jain, P. K.; Lee, K. S.; El-Sayed, I. H.; El-Sayed, M. A., Calculated Absorption and Scattering Properties of Gold Nanoparticles of Different Size, Shape, and Composition: Applications in Biological Imaging and Biomedicine. *J. Phys. Chem. B* **2006,** *110* (14), 7238-7248.

49. Hutter, E.; Maysinger, D., Gold-nanoparticle-based biosensors for detection of enzyme activity. *Trends Pharmacol. Sci.* **2013,** *34* (9), 497-507.

50. Zong, J.; Cobb, S. L.; Cameron, N. R., Peptide-functionalized gold nanoparticles: versatile biomaterials for diagnostic and therapeutic applications. *Biomater. Sci.* **2017,** *5*, 872-886.

51. Dreaden, E. C.; Austin, L. A.; Mackey, M. A.; El-Sayed, M. A., Size matters: gold nanoparticles in targeted cancer drug delivery. *Ther. Deliv.* **2012,** *3* (4), 457-478.

52. Zhou, J.; Patel, T. R.; Sirianni, R. W.; Strohbehn, G.; Zheng, M.-Q.; Duong, N.; Schafbauer, T.; Huttner, A. J.; Huang, Y.; Carson, R. E.; Zhang, Y.; Sullivan, D. J., Jr.; Piepmeier, J. M.; Saltzman, W. M., Highly penetrative, drug-loaded nanocarriers improve treatment of glioblastoma. *Proc. Natl. Acad. Sci. U.S.A.* **2013,** *110* (29), 11751-11756.

53. Alkilany, A. M.; Thompson, L. B.; Boulos, S. P.; Sisco, P. N.; Murphy, C. J., Gold nanorods: Their potential for photothermal therapeutics and drug delivery, tempered by the complexity of their biological interactions. *Adv. Drug Del. Rev.* **2012,** *64* (2), 190-199.

54. Sharma, P.; Brown, S.; Walter, G.; Santra, S.; Moudgil, B., Nanoparticles for bioimaging. *Adv. Colloid Interface Sci.* **2006,** *123-126*, 471-485.

55. Dreaden, E. C.; Alkilany, A. M.; Huang, X.; Murphy, C. J.; El-Sayed, M. A., The golden age: gold nanoparticles for biomedicine. *Chem. Soc. Rev.* **2012,** *41* (7), 2740-2779.

56. Ditzler, L. R.; Sen, A.; Gannon, M. J.; Kohen, A.; Tivanski, A. V., Self-Assembled Enzymatic Monolayer Directly Bound to a Gold Surface: Activity and Molecular Recognition Force Spectroscopy Studies. *J. Am. Chem. Soc.* **2011,** *133* (34), 13284-13287.

57. Daniel, M.-C.; Astruc, D., Gold Nanoparticles: Assembly, Supramolecular Chemistry, Quantum-Size-Related Properties, and Applications toward Biology, Catalysis, and Nanotechnology. *Chem. Rev. (Washington, DC, U. S.)* **2004,** *104* (1), 293-346.

58. Chen, Y.; Xianyu, Y.; Jiang, X., Surface Modification of Gold Nanoparticles with Small Molecules for Biochemical Analysis. *Acc. Chem. Res.* **2017,** *50* (2), 310-319.

59. Hill, H. D.; Mirkin, C. A., The bio-barcode assay for the detection of protein and nucleic acid targets using DTT-induced ligand exchange. *Nat. Protocols* **2006,** *1* (1), 324-336.

60. Kozlowski, R.; Ragupathi, A.; Dyer, R. B., Characterizing the Surface Coverage of Protein–Gold Nanoparticle Bioconjugates. *Bioconjug. Chem.* **2018,** *29* (8), 2691-2700.

61. Sapsford, K. E.; Algar, W. R.; Berti, L.; Gemmill, K. B.; Casey, B. J.; Oh, E.; Stewart, M. H.; Medintz, I. L., Functionalizing Nanoparticles with Biological Molecules: Developing Chemistries that Facilitate Nanotechnology. *Chem. Rev. (Washington, DC, U. S.)* **2013,** *113* (3), 1904-2074.

62. Govorov, A. O.; Richardson, H. H., Generating heat with metal nanoparticles. *Nano Today* **2007,** *2* (1), 30-38.

63. Vilanova, O.; Mittag, J. J.; Kelly, P. M.; Milani, S.; Dawson, K. A.; Rädler, J. O.; Franzese, G., Understanding the Kinetics of Protein–Nanoparticle Corona Formation. *ACS Nano* **2016,** *10* (12), 10842-10850.

64. Wang, J.; Jensen, U. B.; Jensen, G. V.; Shipovskov, S.; Balakrishnan, V. S.; Otzen, D.; Pedersen, J. S.; Besenbacher, F.; Sutherland, D. S., Soft Interactions at Nanoparticles Alter Protein Function and Conformation in a Size Dependent Manner. *Nano Lett.* **2011,** *11* (11), 4985-4991.

65. Cui, M.; Liu, R.; Deng, Z.; Ge, G.; Liu, Y.; Xie, L., Quantitative study of protein coronas on gold nanoparticles with different surface modifications. *Nano Research* **2014,** *7* (3), 345-352.

66. Schade, M.; Moretto, A.; Donaldson, P. M.; Toniolo, C.; Hamm, P., Vibrational Energy Transport through a Capping Layer of Appropriately Designed Peptide Helices over Gold Nanoparticles. *Nano Lett.* **2010,** *10* (8), 3057-3061.

67. Hondred, J. A.; Breger, J.; Garland, N.; Oh, E.; Susumu, K.; Walper, S.; Medintz, I.; Claussen, J. C., Enhanced enzymatic activity from phosphotriesterase trimer gold nanoparticle bioconjugates for pesticide detection. *Analyst* **2017**.

68. Lata, J. P.; Gao, L.; Mukai, C.; Cohen, R.; Nelson, J. L.; Anguish, L.; Coonrod, S.; Travis, A. J., Effects of Nanoparticle Size on Multilayer Formation and Kinetics of Tethered Enzymes. *Bioconjugate Chem.* **2015**, Ahead of Print.

69. Hassan, S.; Schade, M.; Shaw, C. P.; Lévy, R.; Hamm, P., Response of Villin Headpiece-Capped Gold Nanoparticles to Ultrafast Laser Heating. *The Journal of Physical Chemistry B* **2014,** *118* (28), 7954-7962.

70. Pensa, E.; Cortés, E.; Corthey, G.; Carro, P.; Vericat, C.; Fonticelli, M. H.; Benítez, G.; Rubert, A. A.; Salvarezza, R. C., The Chemistry of the Sulfur–Gold Interface: In Search of a Unified Model. *Acc. Chem. Res.* **2012,** *45* (8), 1183-1192.

71. Colangelo, E.; Comenge, J.; Paramelle, D.; Volk, M.; Chen, Q.; Lévy, R., Characterizing Self-Assembled Monolayers on Gold Nanoparticles. *Bioconjug. Chem.* **2016**.

72. Piella, J.; Bastús, N. G.; Puntes, V., Size-Dependent Protein–Nanoparticle Interactions in Citrate-Stabilized Gold Nanoparticles: The Emergence of the Protein Corona. *Bioconjug. Chem.* **2016**.

73. Kapur, A.; Aldeek, F.; Ji, X.; Safi, M.; Wang, W.; Del Cid, A.; Steinbock, O.; Mattoussi, H., Self-Assembled Gold Nanoparticle–Fluorescent Protein Conjugates as

Platforms for Sensing Thiolate Compounds via Modulation of Energy Transfer Quenching. *Bioconjug. Chem.* **2017,** *28* (2), 678-687.

74. Zong, J.; Cobb, S. L.; Cameron, N. R., Peptide-functionalized gold nanoparticles: versatile biomaterials for diagnostic and therapeutic applications. *Biomater Sci* **2017**.

75. Webb, J. A.; Bardhan, R., Emerging advances in nanomedicine with engineered gold nanostructures. *Nanoscale* **2014,** *6* (5), 2502-2530.

76. Link, S.; Burda, C.; Mohamed, M. B.; Nikoobakht, B.; El-Sayed, M. A., Laser Photothermal Melting and Fragmentation of Gold Nanorods: Energy and Laser Pulse-Width Dependence. *The Journal of Physical Chemistry A* **1999,** *103* (9), 1165-1170.

77. Link, S.; El-Sayed, M. A., Shape and size dependence of radiative, non-radiative and photothermal properties of gold nanocrystals. *IRPC* **2000,** *19* (3), 409-453.

78. Hill, J. R.; Dlott, D. D.; Rella, C. W.; Peterson, K. A.; Decatur, S. M.; Boxer, S. G.; Fayer, M. D., Vibrational Dynamics of Carbon Monoxide at the Active Sites of Mutant Heme Proteins. *J. Phys. Chem.* **1996,** *100* (29), 12100-12107.

79. Fujisaki, H.; Straub, J. E., Vibrational energy relaxation in proteins. *Proc. Natl. Acad. Sci. U.S.A.* **2005,** *102* (19), 6726-6731.

80. Xie, A.; Meer, A. F. G. v. d.; Austin, R. H., Excited-State Lifetimes of Far-Infrared Collective Modes in Proteins. *Phys. Rev. Lett.* **2001,** *88* (1), 018102.

Chapter 2 – Experimental Methodology

Parts of this chapter were adapted with permission from:

Kozlowski, R. B.; Ragupathi, A.; Dyer, R. B. Characterizing the Surface Coverage of Protein-Gold Nanoparticle Bioconjugates. *Bioconjugate Chem.* **2018**, *29*, 2691–2700.

Section 2-1: Introduction

In this study, many different techniques and methods were required to characterize bioconjugates and examine kinetics of enzymes with and without external photoexcitation. To ensure that enzyme-AuNP conjugates were prepared correctly, various methodologies were needed to probe the characteristics of the synthesized AuNPs as well as the bioconjugates themselves. Monitoring the activity of the enzyme free in solution and conjugated to AuNPs requires spectroscopic methods, and light driven kinetics were monitored via developed methodologies. This chapter contains six main sections, describing the methodologies for production of DHFR, materials for protein-AuNP conjugation, conjugating protein and AuNPs, analytical methods for characterization, activity assays, and data analysis. Plasmids for enzyme mutants were cloned by Dr. Oskar Laur in the Emory Integrated Genomics Core, which is subsidized by the Emory University School of Medicine. Protein expression and purification was performed by Dr. Rong Fu and Qun Li in Dr. Brian Dyer's lab for all of the enzymes used in this dissertation. Most

chemicals used in this dissertation were purchased from standard commercial sources, and they were all used as received. Dihydrofolate (DHF), the substrate for DHFR, was synthesized using dithionite reduction method,[1] as described later in this chapter. AuNPs of 15 nm diameter were synthesized using the citrate reduction method, as described later in this chapter.[2] The instrumentation and techniques used in this dissertation are described here in detail.

Section 2-2: Dihydrofolate Reductase Production

Section 2-2.1: Mutants of Dihydrofolate Reductase and Plasmid Design

The studies presented in this dissertation all involve the use of protein-AuNP bioconjugates. The protein needs to be site-specifically attached to the gold nanoparticles, such that each attached protein is conjugated in the same manner as all other conjugated proteins. A strong covalent bond is formed between gold and thiols (energy of 40-50 kcal/mol). There are natural thiols in proteins in the form of cysteine amino acid residues. In wildtype (WT) DHFR, there are two intrinsic cysteine residues, C85 and C152. C85 is buried in the folded state of the protein, which would prevent surface conjugation to a nanoparticle. C152 is surface exposed, but it is adjacent to the GH loop and not near the network of coupled motions, which is not an area of interest on the enzyme for these studies. Therefore, both of these cysteine residues were mutated to serine (C152S) and alanine (C85A) to prevent any possibility of multiple attachment sites.

After mutating the intrinsic cysteine residues to other residues, a cysteine residue in an area of interest on the enzyme can be incorporated by further mutation. As described

in the Introduction, DHFR has a network of coupled motions, so areas of interest in the enzyme revolve around that network. G121 is a residue involved in the network of coupled motions in DHFR, so the first mutant, the FG Loop mutant, was a E120C mutation (glutamic acid to cysteine). The second DHFR mutant was E101C, the Alpha Helix mutant, where E101 is immediately next to Y100 (tyrosine), which is near the cofactor binding site residue of the network. This residue seems to be part of the network of coupled motions in DHFR, largely with the conformational changes to allow the binding and release of the cofactor, NADPH.[3] Although there is some connection of this residue to the network, later studies with MD simulations and mutational studies do not show this residue to be a major component of the network.[4, 5] This mutant could serve as a means to determine its relationship to the network of coupled motions experimentally.

For controls, a mutant to allow bioconjugation away from the network of coupled motions was designed. D87 (aspartic acid), the Distal Mutant, was mutated to a cysteine residue. This attachment site is on the side of the enzyme opposite to the active site, and no known residues involved in the network of coupled motions are located around it. Further, this residue is spatially close to the engineered Histidine tag on the C-terminus of the enzyme. The sequences for the single cysteine mutants are shown in **Figure 2.1**.

The last mutant in this dissertation is the His Tagged mutant, which does not have an engineered or intrinsic cysteine in the enzyme. As described in Section 2-4.1, the Histidine tag has a strong interaction with AuNPs, allowing an electrostatic attachment without the use of a cysteine residue. The His Tagged mutant also serves as a control, due to its attachment site being away from the known residues in DHFR's network of coupled motions.

FG Loop Mutant – E120C, C85A, C152S

178 AA

MISLIXXLAV DRVIGMENAM PWNLPADLAW FKRNTLNKPV IMGRHTWESI GRPLPGRKNI
ILSSQPGTDD RVTWVKSVDE AIAAAGDVPE IMVIGGGRVY EQFLPKAQKL YLTHIDAEVC
GDTHFPDYEP DDWESVFSEF HDADAQNSHS YSFEILERRT GGAENLYFQG HHHHHHGA

Alpha Helix Mutant – E101C, C85A, C152S

178 AA

MISLIAALAV DRVIGMENAM PWNLPADLAW FKRNTLNKPV IMGRHTWESI GRPLPGRKNI
ILSSQPGTDD RVTWVKSVDE AIAAAGDVPE IMVIGGGRVY CQFLPKAQKL YLTHIDAEVE
GDTHFPDYEP DDWESVFSEF HDADAQNSHS YSFEILERRT GGAENLYFQG HHHHHHGA

Distal Mutant – D87C, C85A, C152S

178 AA

MISLIAALAV DRVIGMENAM PWNLPADLAW FKRNTLNKPV IMGRHTWESI GRPLPGRKNI
ILSSQPGTDD RVTWVKSVDE AIAAAGCVPE IMVIGGGRVY EQFLPKAQKL YLTHIDAEVE
GDTHFPDYEP DDWESVFSEF HDADAQNSHS YSFEILERRT GGAENLYFQG HHHHHHGA

Figure 2.1: Sequences of Single Cysteine DHFR Mutants.

Residues of interest are color-coded. **Grey:** Residues that are intrinsically cysteines in WT DHFR that have been mutated to non-thiol containing residues. **Green:** The residue of interest that has been mutated to a cysteine – Will be the binding site to the AuNP. **Yellow:** Six residue TEV cleavage sequence – This sequence is cleaved by TEV protease. **Blue:** The hexa-histidine tag that is used for protein purification but cleaved by TEV protease before binding to AuNPs.

Because the Histidine tag strongly associates with the AuNPs, the His tag in the single cysteine mutants was removed via a TEV cleavage, as described in Section 2-4.1. The TEV site, ENLYFQG, was inserted between the enzyme and the His tag, allowing for the His tag to be completely removed from the enzyme.

Section 2-2.3: DHFR Expression and Purification

C-terminal hexa-histidine tagged *E. coli* DHFR was cloned and expressed in BL21(DE3), which is a strain of *E. coli*.[6] WT DHFR and His Tagged DHFR had only the hexa-histidine tag modification. The FG Loop, Alpha Helix, and Distal Mutant DHFR mutants had a TEV cleavage site (Glu-Asn-Leu-Tyr-Phe-Gln-Gly) inserted between the protein and the hexa-Histidine tag, where Gly was inserted directly on the protein. Luria-Bertani (LB) medium containing 100 µg/mL ampicillin was used. A single colony of ampicillin-resistant bacteria was selected and inoculated in 20 mL LB medium, which was stored at 30°C overnight. This was the starter culture, and 1 mL was inoculated into 1000 mL of LB medium. The bacteria were grown at 37°C until OD_{600} reached ~0.7. The growth of cells was stopped by addition of isopropyl β-D-thiogalactopyranoside (IPTG) to a final concentration of 1 mM. The culture was grown overnight at 30°C on an incubator shaking at 200 rpm. The cells were centrifugated at 5000g at 4°C for 15 minutes to harvest the bacteria, then flash frozen and stored at -80°C.

Bacteria pellets were thawed and resuspended in 50 mM Tris, 150 mM NaCl, 5 mM β-mercaptoethanol (βME) at pH 8.0, 1 tablet protease inhibitor per 50 mL of cell lysis buffer, and 1 mg/mL lysosome. The solution was stirred on ice and then sonicated on ice (Sonic Dissemble model 500, Fisher Scientific, Pittsburgh, PA). The insoluble debris was removed via centrifugation at 13000 rpm at 4°C for 30 minutes. The pellet was discarded, and the supernatant was filtered with a 0.22 µm filter and applied to a nickel HisPrep affinity column on a GE Healthcare AKTA FPLC system (GE Healthcare, Pittsburgh, PA). The column equilibration buffer was 50 mM tris-HCl, 150 mM NaCl, 10 mM imidazole, and 5 mM βME at pH 8.0. The protein was eluted though the column with a gradient to

25% elution buffer of 50 mM tris-HCl, 150 mM NaCl, 500 mM imidazole, and 5 mM βME at pH 8.0 for 40 column volumes. The eluted protein was collected in many vials, which were combined and concentration using an Amicon concentrator with a 10 kDa molecular weight cutoff filter (Millipore, Billerica, MA). This concentrated protein was buffer exchanged into storage buffer, containing 50 mM sodium phosphate, 100 mM NaCl, 5 mM dithiothreitol (DTT), and 5% glycerol at pH 7.0 using a HiPrep Desalting column (GE Healthcare). Sodium Dodecyl-Sulfate-Polyacrylamide Gel Electrophoresis followed by Coomassie Blue staining was used to determine the purity of the protein.

Section 2-2.4: TEV Protease Expression and Purification

A Tobacco Etched Virus (TEV) protease plasmid was received as a gift from Dr. Emily Weinert (former PI at Emory University, current PI at Pennsylvania State University). The cell line used in TEV protease expression was Rosetta (DE3) pLysS with ampicillin and chloramphenicol resistance. LB media was supplemented with 100 µg/mL ampicillin and 30 µg/mL chloramphenicol. For each 1 L of LB media, 5 mL of overnight culture was inoculated. Bacteria was grown at 37°C until OD600 was approximately 0.6. The temperature was then lowered to 30°C for 30 minutes. The sample was induced with 1 mM IPTG and allowed to continuing growing at 30°C for 4 hours. Cells were harvested via centrifugation as described in Section 2-2.3.

Per 1 L of harvested culture, cells were resuspended in 10-15 mL of 50 mM potassium phosphate, 100 mM NaCl, 10% glycerol, and 25 mM imidazole at pH 8.0. The cells were lysed with sonication as described in Section 2-2.3. To this sample, 5%

polyethylenimine at pH 7.9 was added to a final concentration of 0.1%. The lysate was centrifuged at 12000 rpm for 30 minutes. The pellet was discarded, and the supernatant was applied to a Ni-NTA column equilibrated with lysis buffer, as described in Section 2-2.3. The supernatant was washed with 7 volumes of lysis buffer, and TEV protease was eluted with a stepwise gradient to 50 mM potassium phosphate, 100 mM NaCl, 10% glycerol, and 200 mM imidazole at pH 8.0. Fractions were analyzed by SDS-PAGE, and the cleanest fractions were pooled with the addition of 1 mM EDTA, 1 mM DTT. The pooled fractions were run on a Sephadex75 column that was pre-equilibrated in 50 mM Tris, 200 mM NaCl, 2 mM EDTA, 2 mM DTT, and 5% glycerol at pH 8.0. These fractions were analyzed by SDS-PAGE, and the cleanest fractions were pooled, aliquoted, and stored at -80°C.

TEV protease is very unstable during concentration. It was important to never concentrate the protein and to always incubate column resin with elution buffers prior to adding the protein to prevent accidental concentration and maximize the yield eluted in each fraction per elution volume. Additionally, TEV protease was very unstable after multiple freeze-thaw cycles, so single use aliquots were made each preparation prior to storage at -80°C. Each 3 L prep produced approximately 3 Sephadex75 16/60 injections, and each injection yielded 30-40 0.5-1 mg/mL 500 µL aliquots.

Section 2-3: Materials for Protein-Gold Nanoparticle Conjugation

Section 2-3.1: Buffers

All buffers used were sodium phosphate buffers, prepared with monobasic and dibasic sodium phosphate, all analytical grade (VWR). The pH was adjusted using concentrated (6 M) or diluted (0.5 M) HCl and NaOH and a calibrated pH meter. The volume addition of acid and base was less than 1% of the total buffer volume, and the salt addition was less than 5% of the buffer concentration.

Section 2-3.2: Protein Stocks

All freshly purified protein stocks were stored at -80°C in 50 mM sodium phosphate, 100 mM NaCl, 5 mM dithiothreitol (DTT), and 5% glycerol at pH 7.0 All free protein samples used in experiments were in 50 mM sodium phosphate buffer at pH 7.0. All protein samples used in AuNP conjugation were in 10 mM sodium phosphate buffer at pH 7.0.

Section 2-3.3: Gold Nanoparticle Synthesis

Citrate stabilized 15 nm AuNPs were synthesized via citrate reduction method.[2] Briefly, 0.1969 g hydrogen tetrachloroaurate (III) trihydrate was combined with 500 mL DI water in a 1 L two neck round bottom flask. The reaction mixture was stirred, heated, and under reflux. Once vigorously boiling (refluxing at 1 drip per second), 0.5704 g sodium citrate dihydrate in 50 mL water was quickly poured in. The reaction mixture was allowed

to reflux for 15 minutes, and the color changed from yellow to clear to black to purple and finally to red. The heat and water for the condenser were turned off, and the mixture was allowed to cool overnight. The mixture of synthesized AuNPs was filtered with a 0.2 μm filter to get rid of the larger aggregates of particles. AuNPs were stored in a glass bottle covered with aluminum foil at 4°C.

UV/Vis absorption spectra of the synthesized AuNPs were measured on a Perkin Elmer Lambda 35 spectrophotometer (Waltham, MA), and were comparable to spectra of NanoXact citrate stabilized 0.05 mg/mL 15 nm diameter AuNPs from Nanocomposix (San Diego, CA) (**Figure 3.4**). Synthesized AuNPs were also characterized with TEM, which is described in detail in Section 2-5.5.

Section 2-3.4: Fluorescence Assay Components

The fluorescence assay developed in this dissertation involves the dissolution of AuNPs via potassium cyanide, KCN. KCN was purchased from Sigma and used as received. Assays also involved the use of sodium phosphate buffer, Tris 2-carboxyethyl | Phosphine (TCEP; from Oakwood Chemical), Tween 20 (from Fisher Scientific), WT DHFR, and the conjugates of interest (FG Loop-AuNP, Alpha Helix-AuNP, Distal Mutant-AuNP, and His Tagged-AuNP. Each solution measured in the fluorometer contained 32 μL of protein/conjugates, 16 μL saturated KCN, and 52 μL 10 mM sodium phosphate buffer for 100 μL total volume, which was the minimum total volume that could be measured in a micro quartz cuvette in the Horiba Dual-FL fluorometer, which had to be elevated with two standard 3/8” nuts placed side-by-side underneath the cuvette itself.

Section 2-4: Conjugating Proteins to Gold Nanoparticles

Section 2-4.1: TEV Cleavage

All freshly purified protein stocks were stored at -80°C in 50 mM sodium phosphate, 100 mM NaCl, 5 mM dithiothreitol (DTT), and 5% glycerol at pH 7.0. DHFR is purified via a hexa-Histidine tag on a nickel column. The Histidine tag has a strong association to the AuNP (1-5 nM dissociation constant),[7] which would cause two binding sites of the protein on AuNPs, the cysteine and the His tag (**Figure 2.2**). A Tobacco Etched Virus (TEV) protease cleavage site of Glu-Asn-Leu-Tyr-Phe-Gln-Gly is inserted between the protein and the Histidine tag, and TEV protease is then used to cleave the Histidine tag from the rest of the protein after initial purification. Briefly, a minimum of 1:20 molar ratio of TEV:DHFR was allowed to react for at least 24 hours at 4°C. The sample was then purified via a Ni-NTA (nitrilotriacetic acid) column, as the uncleaved His tag containing DHFR and His tag containing TEV protease bind to the nickel while the cleaved DHFR products flows through the column.

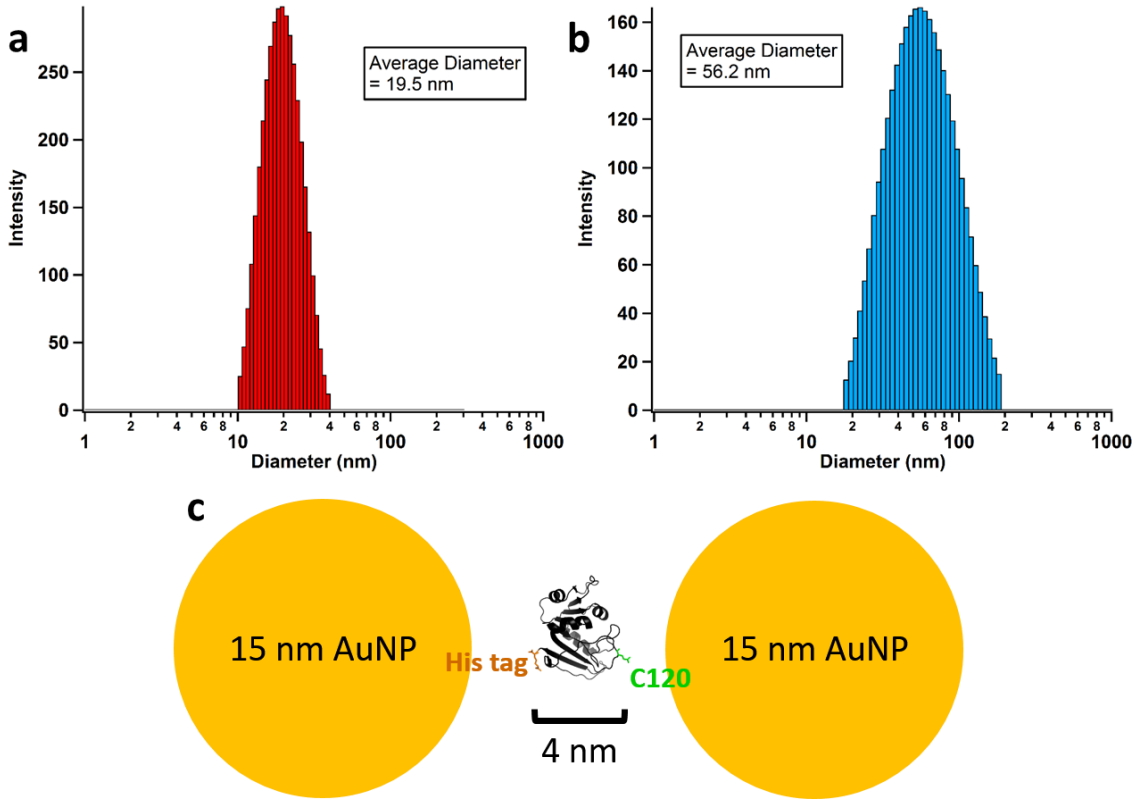

Figure 2.2: DLS of FG Loop-AuNP Before TEV Cleavage.

DLS comparisons of FG Loop mutant of DHFR prior to His tag being cleaved. **a.** Free, unbound 15 nm AuNPs. Diameter obtained is 19.5 nm. **b.** FG Loop mutant with His tag still present. Diameter obtained is 56.2 nm. **c.** Schematic of a potential scenario. One DHFR molecule is 4 nm at its longest, so the expected diameter of the conjugates is free AuNPs plus one full layer of protein, 8 nm maximum, which would be 27.5 nm here. However, 56.2 nm is the observed diameter, meaning there is likely some kind of interaction of the His tag with the AuNPs, potentially a bridging interaction, as depicted here. Reproduced with permission from: Kozlowski, R. B.; Ragupathi, A.; Dyer, R. B. Characterizing the Surface Coverage of Protein-Gold Nanoparticle Bioconjugates. *Bioconjugate Chem.* **2018**, *29*, 2691–2700. Copyright 2018, American Chemical Society.

When binding the protein to AuNPs, the thiols of the cysteine residues need to be available to bind to the gold, so DTT could not be present in the protein added to AuNPs. Further, high salt concentrations will cause AuNPs to crash out in solution, so there could

be minimal sodium phosphate and no presence of NaCl salt. The flow through from the column was therefore buffer exchanged into 10 mM sodium phosphate buffer at pH 7.0 with Millipore Centricon filters for six rounds. With the lack of glycerol, the protein cannot undergo multiple freeze-thaw cycles, and without NaCl, the protein is not extremely stable in solution. Therefore, the protein solution was diluted to 50 μM and aliquoted into approximately 75-125 vials per tube of protein prepped (380 μL for conjugate preparation and 50 μL for free protein activity assays). The aliquots were flash frozen in liquid nitrogen and lyophilized for at least 48 hours. The lyophilized aliquots were labeled and stored at -20°C for up to one year. When rehydrated for use in experiments, samples were rehydrated in 5 mM Tris 2-carboxyethyl phosphine (TCEP) to prevent protein-protein disulfide without the use of sulfur containing reducing agents (such as βME or DTT).

Sodium dodecyl sulfate polyacrylamide gel electrophoresis (SDS-PAGE) was used to further confirm the cleavage (**Figure 2.3**). The denaturing gel shows that cleaved protein travels faster than uncleaved protein, and the mass difference is approximately 2 kDa (cleaved: 21 kDa, uncleaved: 23 kDa), verifying successful cleavage of the His tag.

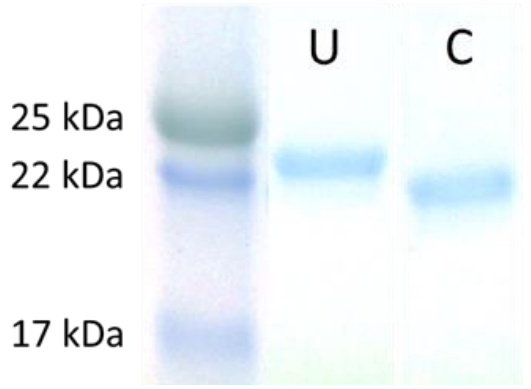

Figure 2.3: SDS-PAGE Before and After TEV Cleavage.

SDS-PAGE gel of the FG Loop mutant before (Lane 2) and after (Lane 3) TEV cleavage. Uncleaved protein (U) runs at 23 kDa. Cleaved (C) protein runs at 21 kDa. The Alpha Helix mutant also shows the same gel profile. Protein ladder is in lane 1. Reproduced with permission from: Kozlowski, R. B.; Ragupathi, A.; Dyer, R. B. Characterizing the Surface Coverage of Protein-Gold Nanoparticle Bioconjugates. *Bioconjugate Chem.* **2018**, *29*, 2691–2700. Copyright 2018, American Chemical Society.

CD spectroscopy was performed on the mutants at 5 μM concentration in 10 mM sodium phosphate buffer on a Jasco J-810 spectropolarimeter (Easton, MD) to confirm the folded state of the mutated enzyme in comparison to WT DHFR (**Figure 2.4**). The FG Loop mutant and Alpha Helix mutant have similar CD spectra to WT DHFR, indicating that the mutants fold properly. The cleavage has approximately a 90% yield when run for either 25 hours with 1:10 TEV:DHFR or 40 hours with 0.5:10 TEV:DHFR.

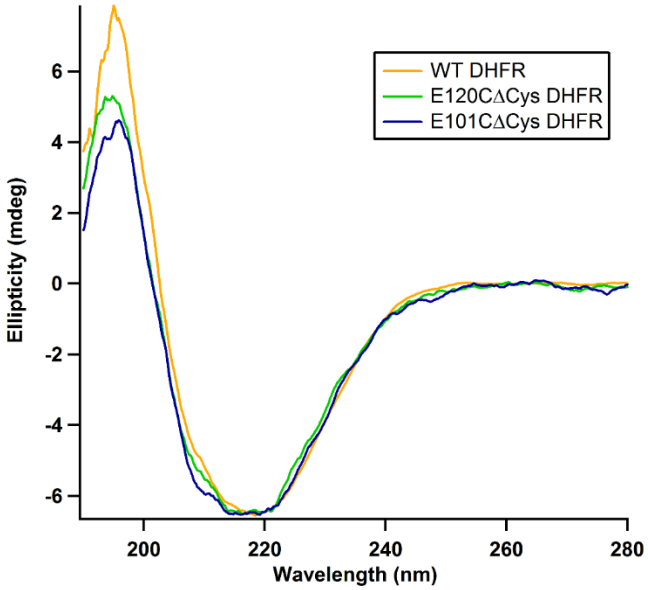

Figure 2.4: CD Spectra of DHFR and Mutants.

CD spectra of free WT, E120CΔCys, and E101CΔCys DHFR in 10 mM sodium phosphate buffer, pH 7. All protein concentrations are 5 μM. There is very little change in the ellipticity of the mutants in comparison to WT DHFR, indicating that the secondary structure of the mutants is similar to that of WT DHFR; the mutants are properly folded. Reproduced with permission from: Kozlowski, R. B.; Ragupathi, A.; Dyer, R. B. Characterizing the Surface Coverage of Protein-Gold Nanoparticle Bioconjugates. *Bioconjugate Chem.* **2018**, *29*, 2691–2700. Copyright 2018, American Chemical Society.

Section 2-4.2: Protein-Gold Nanoparticle Binding Process

DHFR (240 μL of 50 μM) was added to AuNPs at 1,500 times excess (976 μL of 8.5 nM). Multiple tubes of this reaction at these exact volume and concentration levels were set up such that the centrifugation process was consistent. The solution was incubated at 4°C for at least 8 hours to ensure complete binding of protein to AuNPs. After centrifugation, all tubes were simply combined to ensure a consistent sample for later measurements.

Section 2-4.3: Separation of Free Protein from Conjugates

The DHFR-15 nm AuNP conjugates were then centrifuged at 8,000 rpm for 90 minutes on an Eppendorf 5415 D centrifuge (Hauppauge, NY). The supernatant (containing free protein and citrate) was removed, and the pellet (containing the conjugates) was resuspended in 0.005% Tween 20, 10 mM sodium phosphate, pH 7.0 buffer. The resulting solution was centrifuged for 40 minutes and resuspended in Tween 20 buffer twice more to wash away as much free protein as possible from the conjugates. The conjugates were stored in 0.005% Tween 20, 10 mM sodium phosphate pH 7.0 buffer in an 8 times dilution from the combined pellets. For the 5 nm AuNP conjugates, centrifugation cycles are at 13,200 rpm for 90 minutes during all cycles. For the 30 nm AuNP conjugates, centrifugation cycles are at 8,000 rpm for 10 minutes during all cycles. Since the AuNPs from Nanocomposix are more dilute than the synthesized 15 nm AuNPs, the final dilution for these conjugates is 2 times rather than 8 times. The low salt concentration and surfactant help to stabilize the AuNPs, keeping them from sticking to tubes and pipette tips. The stability of the conjugates can be visually seen via colorimetric inspection, as pink represents stable conjugates and purple/blue represents aggregated AuNPs, where the SPR band drastically broadens and redshifts when aggregated.

Section 2-5: Analytical Methods for Characterization

Section 2-5.1: SDS-PAGE

A Biorad Mini-PROTEAN tetra vertical electrophoresis cell (Hercules, CA) was used to run SDS-PAGE gels. The denaturing gels were run with Tris-Glycine-SDS running

buffer. Laemmli sample loading buffer was added such that the final concentration of free protein was 10 μM, and the final dilution of 5 nm conjugates was 4x, 15 nm conjugates was 20x, and 30 nm conjugates was 4x. 10 μL color prestained protein standard, broad range (11-245 kDa) was added to ladder wells, and 15 μL protein or bioconjugate samples were added to each well. The gel was run at 200 V for 35 minutes. A 0.1% Coomassie R-250, 50% methanol, 7% acetic acid solution was used to stain the gel for 30 minutes. A 5% methanol, 7% acetic acid solution was used to destain the gel and was replaced several times for several days before imaging.

Section 2-5.2: UV/Vis Absorption Spectroscopy

UV/Vis absorption spectra of conjugates were taken on a Thermo Scientific Nanodrop 2000 spectrophotometer (Waltham, MA). Appropriate dilutions were used for the conjugate samples, and the spectra were normalized at the peak maximum: 521 nm for 5 nm conjugates, 523 nm for 15 nm conjugates, 524 nm for 30 nm conjugates, 515 nm for free 5 nm AuNPs, 518 nm for free 15 nm AuNPs, and 520 nm for free 30 nm AuNPs.

Section 2-5.3: Dynamic Light Scattering

A Micromeritics Instrument Corporation NanoPlus DLS Nano Particle Size Analyzer instrument (Norcross, GA) was used for DLS measurements. The following settings were used in data collection: Pinhole – 50 μm; Intensity Range – 3,000 to 50,000 counts per second; Scattering Factor – Rayleigh-Gans-Debye (RGD); Analysis method – CONTIN; Noise Threshold: 0.3%; Cell Type – Micro Cell; Correlator Type: Log;

Accumulations – 30, then averaged; Repetitions – 3 then averaged; Laser Wavelength – 665.2 nm; Measurement angle – 173°; Diluent – Water (Refractive index: 1.3300, Viscosity: 0.8900, and Dielectric Constant: 78.3).

Conjugate samples were diluted by 5-10 times, and all samples were filtered with a 0.2 μm filter before running, as dust or larger particles can greatly affect DLS data.

Section 2-5.4: Fluorescence Assay to Determine Protein Concentration

The amount of protein bound to AuNPs was determined through fluorescence assays after dissolving AuNPs with KCN. 16 μL saturated KCN was added to 32 μL washed conjugates. The sample was sonicated in a Fisher Scientific Sonic Dissemble model 500 (Pittsburgh, PA) until the AuNPs were completely dissolved, and 52 μL of 10 mM sodium phosphate buffer was added for the final dilution. The dissolved AuNP samples were stored at room temperature until use. Stock solutions for a calibration were made in 0.005% Tween 20, 10 mM sodium phosphate buffer to keep the amount of Tween 20 consistent among all samples. The stock solutions were WT DHFR at 10 μM, 5 μM, 3 μM, 2 μM, 1 μM, and 0.5 μM. The samples were run on a Horiba Scientific Dual-FL fluorometer (Edison, NJ) using a quartz fluorometer cuvette. The excitation wavelength was 280 nm with a 2 pixel increment. The tryptophan emission peak is highly concentration dependent and is used as the calibration factor for the standards. The integration (peak area) of the emission peak from 300 to 385 nm was plotted versus the concentration of protein in the standard to generate the standard curve. A linear fit to the data was used to determine the concentration of the unknown samples. There is a minor effect of KCN on the emission spectrum, so the WT stock samples were prepared with an equivalent amount of KCN.

Section 2-5.5: Transmission Electron Microscopy

Samples were diluted to a nanoparticle concentration of 1 nM and dispersed and dried on 200 mesh copper TEM grids. When imaging protein-AuNP conjugates, a stain was required, as the protein does not contain enough electrons to be visible in a TEM image. Sodium phosphotungstate is a negative stain. AuNPs themselves contain extremely high amounts of electrons, and proteins do not. The stain also contains many electrons, so in a TEM image, the AuNPs are very dark, the surrounding protein later will not be colored, and the stain itself will be darker than the protein layer, allowing the protein layer itself to be visible. The grids were stained with 2% sodium phosphotungstate at pH 7.8 for 30 seconds before being wicked away. The grid was allowed to dry. TEM images were all taken on a Hitachi H7000 TEM (Hitachi High-Technologies America, Inc., Pleasanton, CA) with an accelerating voltage of 80 kHz.

Section 2-6: Activity Assays

Section 2-6.1: Standard Activity Assays

Activity assays were run by monitoring the decrease in 340 nm absorbance on an Ocean Optics QE65000 spectrometer (Winterpark, FL) with a Xenon lamp source, following the oxidation of NADPH to $NADP^+$. 50 mM sodium phosphate pH 7.0 buffer, NADPH (50 μM), and DHFR (10-30 nM) were added into a cuvette and allowed to equilibrate at 37°C in an Ocean Optics QPOD temperature-controlled cuvette stage (Winterpark, FL) for 5 minutes. DHF (50 μM) was added to initiate the reaction, and the 340 nm absorbance was measured over 5 minutes. All reactions were run in at least

triplicate. Enzyme turnover was calculated by method of initial rates, which was either linear or exponential depending on the sample. For the exponential fits, pre-exponential (A) and τ parameters from an exponential fit were used with the integrated extinction coefficient for NADPH (11,800 $M^{-1}cm^{-1}$) to determine the initial rate of the reaction. The linear fits were used with the integrated extinction coefficient to determine the initial rate. The concentration of protein was used with the initial rate to determine enzyme turnover (in s^{-1}).

Section 2-6.2: Temperature Dependent Kinetics

The temperature-dependent kinetic assays were run as described in the Standard Activity Assay section. The assays were run at six different temperatures: 22°C, 27°C, 32°C, 37°C, 42°C, and 47°C. The raw data were fit to linear or exponential fits (**Figure 5.3**). The natural log of the rates is plotted on the y-axis of the Arrhenius plots, and the respective inverse temperatures are on the x-axis (**Figure 5.4** and **Figure 5.5**). The slope of the line was used to determine the activation energy, E_a, as it represents $-E_a/R$, where R is the gas constant 8.314 J/K·mol. The rates and temperatures were plotted as ln(rate) vs inverse temperature, described by the Arrhenius equation:

$$ln(k) = \frac{1}{T} \cdot \frac{-\Delta E_a}{R} + ln(A)$$

Section 2-6.3: Lasers for Heating Experiments

Light driven activity experiments were performed with two pulsed laser sources, one with nanosecond pulses and one with femtosecond pulses. The ns laser was a

CrystaLaser diode pumped Q-switched 527 nm laser with 20 ns pulses (Reno, NV) set to 5.0 kHz repetition rate. The 80 fs pulses were generated from a Coherent ultrafast laser system described elsewhere to produce 530 nm light in 80 fs pulses with a 1.0 kHz repetition rate (**Figure 2.5**).[8-10] For a control experiment, a non-pulsed laser source, continuous wave light, was used. The CW laser was a Verdi Coherent 531 nm, 5 W CW pump laser (Santa Clara, CA).

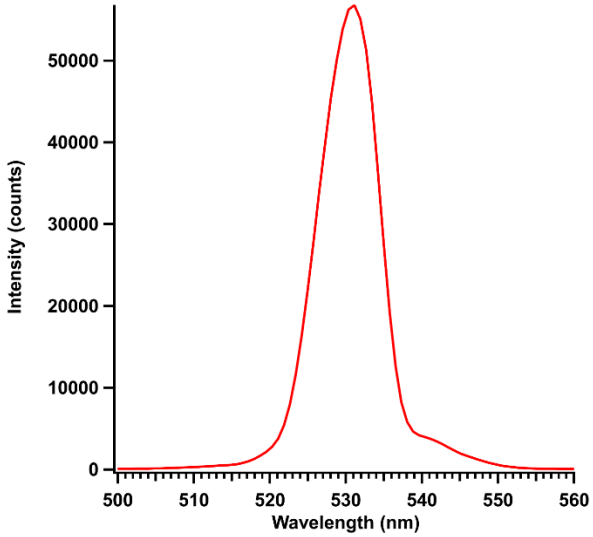

Figure 2.5: Spectrum of 80 fs Laser Pulse.

The Coherent ultrafast laser system described was used to generate 530 nm-80 fs pulses.

Section 2-6.4: Light Driven Activity Assays

The light driven activity assays were performed as described in the Standard Activity Assays section, with the perpendicular addition of either the CW, 20 ns pulsed, or 80 fs pulsed lasers. In all cases, the laser was aligned perpendicularly to the Xenon lamp

source in the cuvette stage (**Figure 4.6**). The green lasers do not interfere with the probing of the sample, as the beams cross the sample perpendicular to the probe beam and are terminated into a beam dump or power meter for laser power determination. The power of the laser was attenuated with a continuous variable neutral density filter and monitored with a power meter after interaction with the sample. The power absorbed by the sample is roughly half of the initial power; for example, for a typical 40 mW power trial, the power measured through the sample was 20 mW. The sample was continuously illuminated with the laser throughout the entire 5-minute duration of the activity measurements. The laser was aligned by inserting a fiber optic cable into the holder on the receiving end of the laser in cuvette stage (in place of the beam dump) and placing two pinholes into the sample holder. This fiber optic cable was attached to the spectrometer. The mirrors directing the laser into the cuvette stage were adjusted to maximize the laser intensity through the pinholes and onto the centered fiber, which maximizes alignment with the fiber optic coupled Xenon lamp source in the perpendicular holders on the cuvette holder.

Before the assay, the sample was allowed to equilibrate at 37°C with the laser blocked. DHF was added to initiate the reaction, and the laser block was immediately removed upon start of data collection. Laser power was attenuated with a variable neutral density filter, from 50 mW to 200 mW for ns experiments, from 5 mW to 40 mW for fs experiments, and from 100 mW to 200 mW for CW experiments. The pump laser diameter was collimated to 2 mm for all excitation sources, fully spanning the open width of the micro volume Starna Cells fluorescence cuvette (Atascadero, CA). This allowed the pump beam to excite the entirety of the sample in the plane of the laser. The probe beam diameter

was half the diameter of the pump beam at 1 mm and passed through the center of the pump laser beam, which allowed only the pumped sample to be probed.

Section 2-7: Data Analysis

Section 2-7.1: Activity Assays

UV/Vis absorption spectra are obtained using a Xenon lamp and Ocean Optics detector. Each time point obtained produced a full range intensity spectrum from 200 nm to 900 nm saved as a txt file. Data points were collected every second, so for a standard five-minute assay, 300 txt intensity spectrum files were produced. The 300 txt files were loaded into IgorPro 7 via a designed loading procedure. As described in Section 2-6.1, the absorption at 340 nm was monitored for activity assays, watching the oxidation of NADPH cofactor to $NADP^+$. A procedure script was written to take the loaded waves and pull out only the 340 nm intensity point in the spectrum. A similar script was written to pull out the 425 nm intensity point. The Xenon lamp used for the light source was fairly noisy, and the changes observed in these experiments were quite small. To correct for the noise in the spectrum, an intensity normalization was employed to correct for lamp intensity fluctuations. The intensity at 425 nm was separated from the kinetics of interest, and over time, the 425 nm absorbance did not change over the course of enzyme turnover (**Figure 2.6**). Thus, any observed changes in intensity (and thus absorbance due to Beer's Law) at 425 nm were deemed to be due to lamp fluctuations.

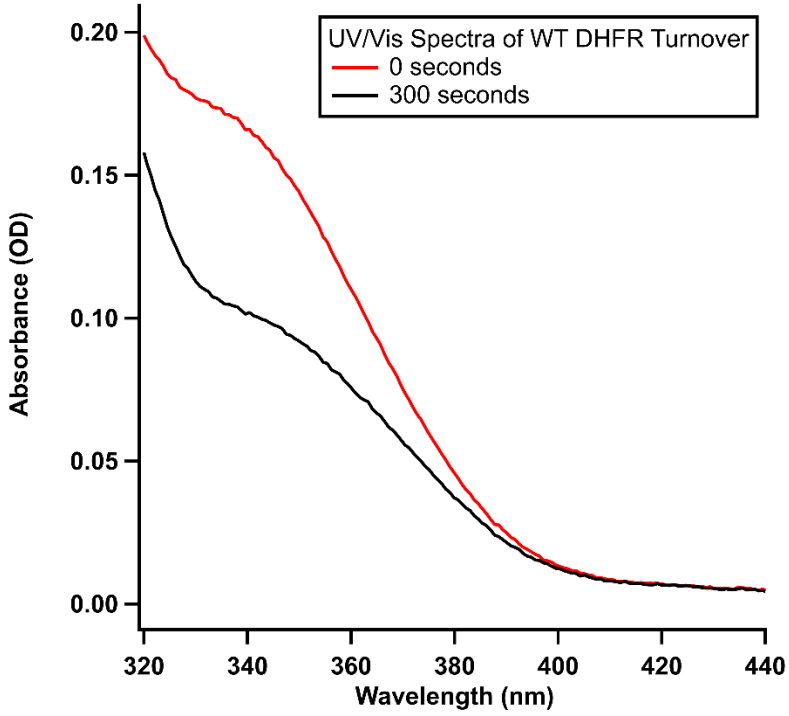

Figure 2.6: WT DHFR UV/Vis Before and After Activity Assay.

UV/Vis absorption spectra of WT DHFR before an activity assay (red) and after a five-minute activity assay (black). There is clearly a change in absorbance from 320-420 nm. Beyond 420 nm, there is no change in absorption over the course of a reaction.

A normalization factor was created based on the average intensity of light at 425 nm in each of the experimental trials (approximately 40,000-45,000 counts depending on the lamp intensity).

$$Normalization\ Factor = \frac{45{,}000\ counts}{425\ nm\ Intensity}$$

This normalization factor served as a correction for each data point, as it gives the amount of deviation from a constant intensity value. Any difference in the normalization factor was a difference not due to kinetics. A normalized 340 nm intensity was obtained by using the normalization factor.

$$Normalized\ 340\ nm\ Intensity = \ Normalization\ Factor \times 340\ nm\ Intensity$$

The normalized 340 nm value is an intensity, so the intensity was converted to an absorbance using Beer's Law. The incident intensity was measured through a "blank", where the light was passed to the detector in the absence of a sample. The light intensity in the absence of a sample varied based on lamp intensity and lamp spectrum conditions (approximately 25,000-30,000 counts).

$$Absorbance\ at\ 340\ nm = \ -\log\left(\frac{Normalized\ 340\ nm\ Intensity}{30{,}000\ counts}\right)$$

Finally, to correct for slight variations in sample conditions, all absorbance data points were vertically shifted to a common starting absorbance of 0.18, the calculated value based on sample concentrations. This simply added or subtracted a common value from every single point in the time course to start the initial data point at OD 0.18. This was the data sent through further analysis as described in Section 2-6.1.

Section 2-7.2: Transmission Electron Microscopy

TEM images were analyzed with the program ImageJ (**Figure 2.7**). The scale bar from each individual image was calibrated to set the scale in ImageJ for each respective image. The threshold in ImageJ was set to where the AuNPs were mostly saturated, but not bleeding into the background or each other, which turns the AuNPs black and the background white (**Figure 2.7** right images). Narrow lines between each AuNP were manually "erased" to keep them as separate particles for analysis. Any sections of aggregated AuNPs were completely erased because individual particles could not be distinguished. Particles were analyzed for area. The diameter was then determined from the area based on the area of a circle, $A = \pi(d/2)^2$. The average AuNP diameter and standard deviation of 75 analyzed particles were determined to be 14.1 ± 1.4 nm.[11]

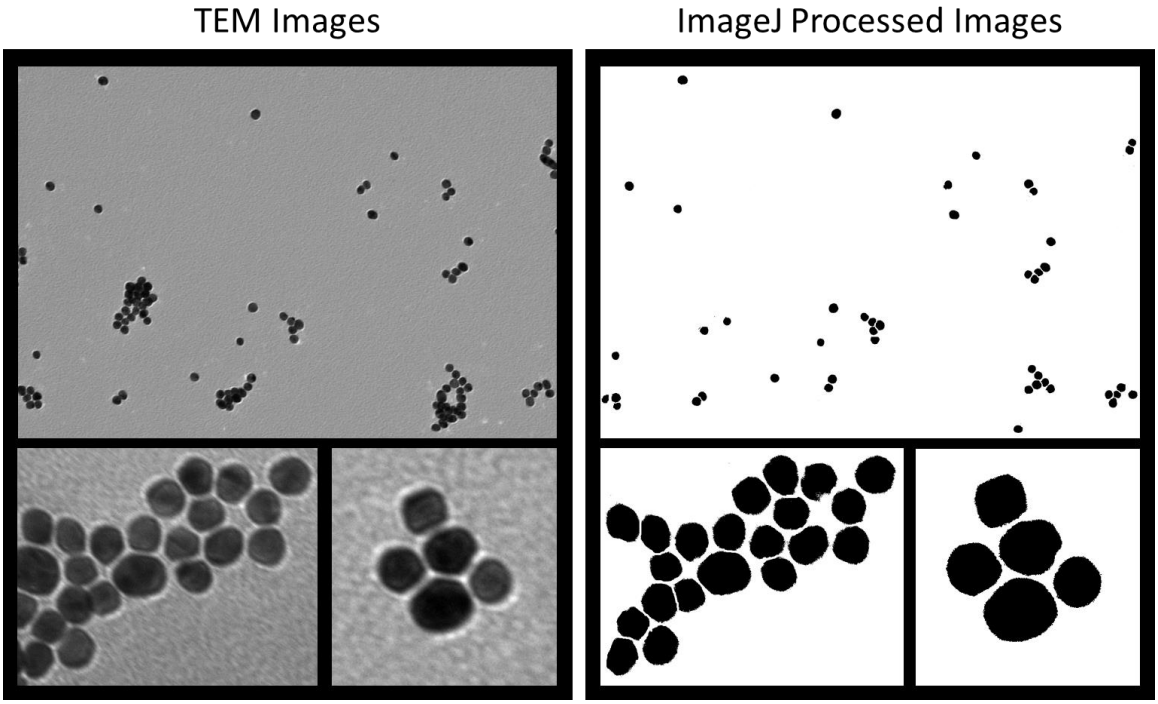

Figure 2.7: TEM of Synthesized AuNPs.

TEM images of synthesized AuNPs versus the same images processed in ImageJ for size analysis, each with different scale bars.[11] Reproduced with permission from: Kozlowski, R. B.; Ragupathi, A.; Dyer, R. B. Characterizing the Surface Coverage of Protein-Gold Nanoparticle Bioconjugates. *Bioconjugate Chem.* **2018**, *29*, 2691–2700. Copyright 2018, American Chemical Society.

Section 2-7.3: COMSOL Simulations

COMSOL simulations were performed with the Heat Transfer module to determine the theoretical amount of heat transferred from the AuNP after laser excitation. The laser power absorbed by each AuNP is calculated using the following equation:

Equation 2.1

$$p_{AuNP} = \frac{p_{Laser} \times (1-\zeta)^2 \times \left(1 - 10^{-\varepsilon_{AuNP} lc}\right)}{c\sigma l N_A}$$

$\mathbf{P_{AuNP}}$: The laser power absorbed by each AuNP.

Assuming that AuNP photo-thermal conversion efficiency is 100%, then all photon energy is converted to thermal energy. Thus, $\mathbf{P_{AuNP}}$ is equivalent to the heating power of AuNP. Therefore, we use $\mathbf{P_{AuNP}}$ as the power of heating source to calculate the heat dissipation and temperature gradient in the surrounding environment in the simulations.

20 ns Pulsed Experiment:

Variables in **Equation 2.1**:

$\mathbf{P_{Laser}}$: The laser power of the Q-switched laser during the 20 ns pulse.

The average power of 527 nm Nd:YAG Q-switched laser (CrystaLaser®) at the sample is determined to be **100 mW** or **200 mW**.

The 527 nm Nd:YAG Q-switched laser is operating at 5,000 Hz and each with a 20 ns pulse duration. Therefore, $\mathbf{P_{Laser}}$ = 100 mW / 5000 Hz / 20 ns = $\mathbf{1 \times 10^3\ W}$ during the 20 ns laser pulse.

ξ : Scattering coefficient of cuvette, **0.04**.

ε_{AuNP} : The molar absorption coefficient of AuNP. $\varepsilon_{AuP,\,527nm} = \mathbf{3.67 \times 10^8\ M^{-1}\ cm^{-1}}$.

l : The pathlength of cuvette, **1 cm**.

c : Molar concentration of AuNP in the sample, **1.10 nM**.

Therefore, the absorbance of the AuNP sample in the cuvette is $A = \varepsilon lc = 0.404$.

$\boldsymbol{\sigma}$: The laser spot size of pulse laser beam. Since the diameter of the laser spot is **2 mm**, thus the spot size is $\mathbf{3.14 \times 10^{-6}\ m^2}$.

$\boldsymbol{N_A}$: Avogadro Number, $\mathbf{6.02 \times 10^{23}}$.

Given all the parameters listed above, we can calculate that

$\mathbf{P_{AuNP}}$ **= 2.68 * 10^{-8} W for 100 mW laser power**

and $\mathbf{P_{AuNP}}$ **= 5.37 * 10^{-8} W for 200 mW laser power.**

80 fs Pulsed Experiment:

Variables in **Equation 2.1**:

$\mathbf{P_{Laser}}$: The laser power of the Q-switched laser during the 20 ns pulse.

The average power of a 530 nm, 80 fs, 1 kHz laser at the sample is determined to be **5 mW**, **20 mW** and **40 mW**.

The 530 nm, 80 fs laser is operating at 1000 Hz and each with a 80 fs pulse duration. Therefore, $\mathbf{P_{Laser}}$ = 40 mW /1000 Hz/ 80 fs = $\mathbf{5 \times 10^{8}\ W}$ during the 80 fs laser pulse.

ξ : Scattering coefficient of cuvette, **0.04**.

$\boldsymbol{\varepsilon_{AuNP}}$: The molar absorption coefficient of AuNP. $\boldsymbol{\varepsilon_{AuP,\,527nm}}$ = $\mathbf{3.67\times 10^{8}\ M^{-1}\ cm^{-1}}$.

l : The pathlength of cuvette, **1 cm**.

c : Molar concentration of AuNP in the sample, **1.00 nM**.

Therefore, the absorbance of the AuNP sample in the cuvette is A = εlc = 0.367.

$\boldsymbol{\sigma}$: The laser spot size of pulse laser beam. Since the diameter of the laser spot is **2 mm**, thus the spot size is **3.14×10^{-6} m^2**.

$\boldsymbol{N_A}$: Avogadro Number, **6.02×10^{23}**.

Given all the parameters listed above, we can calculate that

P_{AuNP} = 1.34 * 10^{-2} W for 40 mW laser power

P_{AuNP} = 6.7 * 10^{-3} W for 20 mW laser power

and **P_{AuNP} = 1.675 * 10^{-3} W for 5 mW laser power.**

For all heat flow experiments, the heat transfer of the AuNP to the surrounding environment is described by the following two sets of 3-dimensional heat transfer equations, in which variable ***s*** represents the 3D coordinate (x, y, z) in the model.

The first set of equations describe the heat transfer in the AuNP and H_2O surrounding environment respectively:

Equation 2.2:

$$\begin{cases} \rho_{(Au)} C_{p(Au)} \partial_t T(s,t) = \kappa_{(Au)} \nabla^2 T(s,t) + p_{AuNP}(s,t) & s \in \text{AuNP region} \\ \rho_{(w)} C_{p(w)} \partial_t T(s,t) = \kappa_{(w)} \nabla^2 T(s,t) & s \in \mathrm{H_2O} \text{ region} \end{cases}$$

$\boldsymbol{\rho}$: density

$\boldsymbol{C_p}$: specific heat capacity

$\boldsymbol{T}$: temperature

$\boldsymbol{\kappa}$: thermal conductivity

The second set of equations describe the boundary conditions that defines the heat transfer and surface temperature condition at the AuNP/H_2O interface:

Equation 2.3:

$$\begin{cases} \kappa_{(Au)}\partial_r T(S^-,t) = \kappa_w \partial_r T(S^+,t) & S^- \in \text{Inner surface } of \text{ AuNP region} \\ T(S^-,t) = T(S^+,t) & S^+ \in \text{Outer surface of AuNP that in } H_2O \text{ region} \end{cases}$$

$\boldsymbol{T}$: temperature

$\boldsymbol{C_p}$: specific heat capacity

$\boldsymbol{\kappa}$: thermal conductivity

Section 2-8: Chapter 2 References

1. Blakley, R. L., Crystalline dihydropteroylglutamic acid. *Nature* **1960,** *188*, 231-232.

2. Hill, H. D.; Mirkin, C. A., The bio-barcode assay for the detection of protein and nucleic acid targets using DTT-induced ligand exchange. *Nature Protoc.* **2006,** *1* (1), 324-336.

3. Agarwal, P. K.; Billeter, S. R.; Rajagopalan, P. T. R.; Benkovic, S. J.; Hammes-Schiffer, S., Network of Coupled Promoting Motions in Enzyme Catalysis. *Proc. Natl. Acad. Sci. U.S.A.* **2002,** *99*, 2794-2799.

4. Singh, P.; Francis, K.; Kohen, A., Network of Remote and Local Protein Dynamics in Dihydrofolate Reductase Catalysis. *ACS Catal.* **2015,** *5* (5), 3067-3073.

5. Singh, P.; Sen, A.; Francis, K.; Kohen, A., Extension and Limits of the Network of Coupled Motions Correlated to Hydride Transfer in Dihydrofolate Reductase. *JACS* **2014,** *136* (6), 2575-2582.

6. Reddish, M. J.; Vaughn, M. B.; Fu, R.; Dyer, R. B., Ligand-Dependent Conformational Dynamics of Dihydrofolate Reductase. *Biochemistry* **2016,** *55* (10), 1485-1493.

7. Aldeek, F.; Safi, M.; Zhan, N.; Palui, G.; Mattoussi, H., Understanding the Self-Assembly of Proteins onto Gold Nanoparticles and Quantum Dots Driven by Metal-Histidine Coordination. *ACS Nano* **2013,** *7* (11), 10197-10210.

8. Li, G.; Magana, D.; Dyer, R. B., Photoinduced Electron Transfer in Folic Acid Investigated by Ultrafast Infrared Spectroscopy. *J. Phys. Chem. B* **2012,** *116* (10), 3467-3475.

9. Li, G.; Magana, D.; Dyer, R. B., Direct Observation and Control of Ultrafast Photoinduced Twisted Intramolecular Charge Transfer (TICT) in Triphenyl-Methane Dyes. *J. Phys. Chem. B* **2012,** *116* (41), 12590-12596.

10. Li, G.; Magana, D.; Dyer, R. B., Anisotropic energy flow and allosteric ligand binding in albumin. *Nat. Commun.* **2014,** *5*, 4100/1-4100/7.

11. Kozlowski, R.; Ragupathi, A.; Dyer, R. B., Characterizing the Surface Coverage of Protein–Gold Nanoparticle Bioconjugates. *Bioconjug. Chem.* **2018,** *29* (8), 2691-2700.

Chapter 3 – Synthesizing and Characterizing Enzyme-Gold Nanoparticle Conjugates

Adapted with permission from:

Kozlowski, R. B.; Ragupathi, A.; Dyer, R. B. Characterizing the Surface Coverage of Protein-Gold Nanoparticle Bioconjugates. *Bioconjugate Chem.* **2018**, *29*, 2691–2700.

Section 3-1: Introduction

The conjugation of proteins to nanoparticles has attracted broad interest due to potential biomedical and nanotechnological applications.[1-4] More specifically, gold nanoparticle (AuNP) bioconjugates have many potential biological applications, including biosensing,[5, 6] enzyme immobilization,[7] drug delivery,[8-10] and bioimaging.[11, 12] For example, AuNPs have been used as colorimetric biosensors in ligand-receptor chemistry to isolate viable cells from a population of cells, which has implications in diagnostic applications and cancer biology assays.[13] Extending the fundamental research into clinical trials, a first-in-man trial has been completed, where silica coated AuNPs have been bioengineered into a transplantation patch that was implanted onto a cardiac artery in patients with atherosclerosis (ClinicalTrials.gov Identifier: NCT01270139).[14] AuNPs are of particular interest due to their biocompatibility and their ability to be surface functionalized and used as a delivery vehicle. Further, AuNPs have useful optical

properties due to their surface plasmon resonance (SPR), which is the collective oscillation of electrons on the nanoparticle surface.[15, 16] The SPR absorption of AuNPs depends on the size of the particle and the dielectric constant of the capping molecules on the AuNP surface. In 100 nm spherical AuNPs or smaller, the SPR absorption band is centered in the green region of the visible spectrum.

Proteins have been attached to AuNPs mainly using two methods: adsorption by electrostatic interactions or covalent binding via functional groups.[17-20] With electrostatic attachment, the binding is via noncovalent interactions specific to the charge of the capping ligand on the AuNP and the charge on the protein surface. Other noncovalent forces may help stabilize protein attachment, such as hydrogen bonding, Van der Waals, or hydrophobic interactions.[21-23] This type of conjugation is non-specific because the protein can associate to the AuNP surface in many different orientations, depending on protein structure and surface charge. In contrast, attachment of the protein through covalent binding occurs with a specific functional group that binds to either the gold itself or a capping ligand.[19, 20, 24, 25] A surface exposed cysteine has been used as an attachment site on proteins, as the thiol will covalently bind to the gold. This covalent method of conjugation is beneficial because the attachment point on the protein is site-specific. The cysteine can be selectively placed such that the protein binds to a specific area of interest on the protein.[26-28] This ability to control the location of the nanoparticle in relation to the protein and to create a tighter bond between the protein and nanoparticle are key motivations for covalent bioconjugation.

There have been significant efforts to characterize protein-nanoparticle bioconjugates, and surface coverage is an important parameter in bioconjugate stability and

protein functionality. The activity of an enzyme-AuNP bioconjugate is directly related to the number of proteins bound to the nanoparticle surface; higher surface coverage gives a greater number of catalytic sites per AuNP and usually increases the bioconjugate activity.[29] At high surface coverage levels, however, protein crowding may become an issue.[30] Protein crowding might restrict access of the substrate and cofactor to their respective binding sites on the enzyme, or it might hinder the dynamics necessary for the protein to function, such as loop motions. In addition, the protein structure itself might be stabilized or destabilized due to electrostatics and sterics of protein-protein interactions.[31, 32] These effects of crowding negatively influence the activity of the enzyme. In contrast, for enzyme cascades, having multiple enzymes in close proximity can enhance the overall efficiency by substrate channeling or by speeding up the diffusion process.[33] Therefore, the design of functional bioconjugates should consider the balance between the number of available catalytic sites and the effects of protein crowding on the nanoparticle surface. Further, surface coverage can be affected by the method of attachment (covalent or noncovalent) and the size and surface curvature of the AuNP (larger AuNP means smaller curvature). All of these factors should be considered when designing bioconjugates for optimum function. There have been reports of methods to determine surface coverage of biomolecules on nanoparticle surfaces, but these methods either require a significant amount of biomolecule-NP conjugates or are complicated in nature.[34-36] We present a simple, sample conservative fluorescence based assay in conjunction with UV/Vis absorption spectroscopy method to accurately determine the surface coverage of protein on gold nanoparticles.

The most common methods for bioconjugate characterization employ UV/Vis spectrophotometry and transmission electron microscopy (TEM).[17-19] However, these methods alone do not account for unbound protein or the molar ratio of bound protein to nanoparticle. A method has been reported for measuring the concentration of protein bound to AuNPs using circular dichroism (CD) spectroscopy.[37] The lack of sensitivity of CD and large scattering background from nanoparticles limit this approach to high total protein concentrations, and the method assumes the protein bound to the nanoparticle surface is folded in the same manner (and thus has the same spectrum) as free in solution. Further, there are no reported methods for accurate protein concentration determination for low protein concentration samples (ie. a monolayer of protein on AuNPs), as AuNPs scatter significantly in the near UV and UV region of the absorption spectrum. Clearly, a new approach is required to determine the ratio of bound protein to nanoparticles to characterize the surface coverage of bioconjugates.

In this study, *E. coli* dihydrofolate reductase (ecDHFR) is used as a model enzyme for bioconjugate characterization studies. DHFR catalyzes the reduction of dihydrofolate (DHF) to tetrahydrofolate (THF) via the oxidation of the cofactor nicotinamide adenine dinucleotide phosphate (NADPH) to $NADP^+$.[38] The enzyme is covalently linked to the AuNPs via a site-specific cysteine engineered into the enzyme surface. An integrated suite of physical methods is used to isolate and characterize the bioconjugates, including a method to separate free protein from bioconjugates and account for the free protein that might still be present. A novel method to determine the protein concentration of bioconjugates directly and accurately is reported, which is used in conjunction with UV/Vis absorption spectra of the AuNPs to accurately determine surface coverage of protein on the

AuNPs. This novel approach for measuring the protein/AuNP ratio is combined with dynamic light scattering (DLS) to demonstrate that the surface coverage is monolayer or sub-monolayer. The effect of AuNP surface coverage on protein binding and surface coverage are assessed by varying the AuNP sizes over a range of diameters from 5 nm to 30 nm. The surface coverage of protein is found to be related to the curvature of the AuNP surface, with higher surface coverage on AuNPs of greater curvature. The combination of these characterization methods is important for understanding the functionality of protein-AuNP bioconjugates, particularly enzyme activity.

Section 3-2: Results and Discussion

Section 3-2.1: Conjugate Design and Preparation

The design of DHFR-AuNP conjugates for this study incorporates a site-specific, surface exposed cysteine that is capable of forming a covalent bond with the gold atoms of the AuNP. These conjugates were purified from free, unbound enzyme (**Figure 3.1**), and then characterized with an integrated suite of biophysical methods. The concentrations of AuNPs was determined by UV/Vis spectroscopy and protein was determined by fluorescence after dissolution of AuNPs by KCN, and these concentrations were used to calculate surface coverage of proteins on the AuNPs.

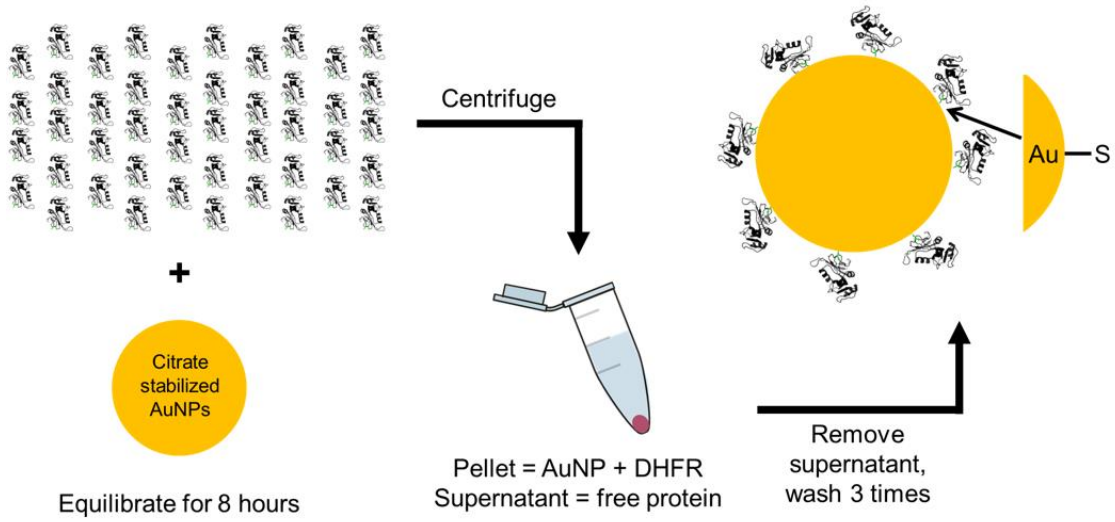

Figure 3.1: Schematic of Protein-AuNP Conjugation Process.

A large excess of DHFR is added to citrate stabilized AuNPs and allowed to equilibrate for no less than 8 hours. The samples were centrifuged to pellet the conjugates and the supernatant of free protein and citrate was removed by pipetting. Buffer was added to resuspend the pellet, and this process was repeated at least 3 times to remove all free protein from the conjugate solution.[39] Reproduced with permission from: Kozlowski, R. B.; Ragupathi, A.; Dyer, R. B. Characterizing the Surface Coverage of Protein-Gold Nanoparticle Bioconjugates. *Bioconjugate Chem.* **2018**, *29*, 2691–2700. Copyright 2018, American Chemical Society.

Conjugate Design. Citrate, a weak capping ligand, was used to cap the AuNPs so that the protein thiolate S^- would easily displace the citrate molecules from the AuNP surface. Wildtype (WT) DHFR contains two intrinsic cysteines at positions 85 and 152. When WT DHFR is folded, C85 is buried and not exposed to the surrounding solution, while C152 is surface exposed, located just off the GH loop of the protein. Because these cysteines might compete with the intended sites of attachment, both of them were replaced by site-specific mutation (ΔCys), C85 to an alanine (C85A) and C152 to a serine (C152S). Because the hexa-histidine tag added to the C-terminus of the protein for purification strongly associates to AuNPs,[40] it was cleaved prior to formation of the bioconjugate to

leave only the surface cysteine as the single binding point to the AuNPs. Two additional variants of DHFR were made to introduce non-native cysteines in surface exposed positions as specific points of attachment, designated as the FG Loop mutant and Alpha Helix mutant (**Figure 3.2a-b**). The FG Loop mutant (E120CΔCys, **Figure 3.2a**) has E120 on the FG loop mutated to a cysteine (E120C). The Alpha Helix mutant has E101 on a rigid alpha helix mutated to a cysteine (E101CΔCys, **Figure 3.2b**). These mutants are used to test the effect of the location of the point of attachment to the protein on the bioconjugate properties. The FG Loop mutant is expected to sterically hinder the substrate and cofactor from entering the active site, but the orientation on the AuNP should not completely prohibit the substrate and cofactor binding. The Alpha Helix mutant might sterically prevent the cofactor from having free access, but just as with the FG Loop mutant, it should not completely prevent binding. The focus of the present study is on the characterization of the bioconjugates formed with these enzyme constructs; the full evaluation of the reactivity of these bioconjugates will be published elsewhere.

Mutant Activity. The enzyme activities of the free mutants were assayed in comparison to WT DHFR to ensure that the mutations did not greatly affect enzyme function. The steady state kinetics of cofactor oxidation (NADPH absorbance at 340 nm) for the FG Loop mutant, Alpha Helix mutant, and WT DHFR in the presence of a large excess of substrate and cofactor are compared in **Figure 3.2c**. Since these kinetics measurements were obtained under identical conditions, they can be compared to assess the relative enzyme activity of each enzyme variant. The kinetics and thus the activity of each mutant is nearly identical to WT DHFR, so these mutations do not affect the ability of DHFR to catalyze the reduction of DHF.

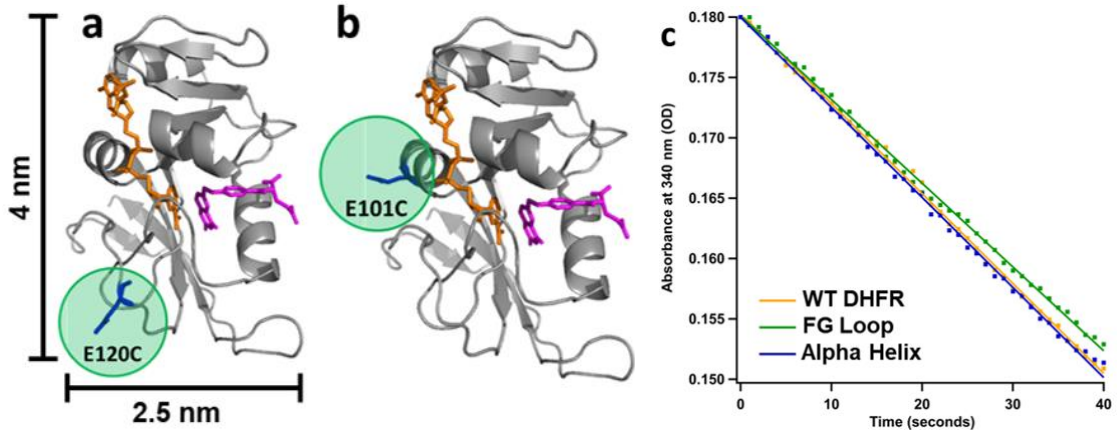

Figure 3.2: DHFR Mutants.

Location of cysteine mutation (highlighted in green) for (a) FG Loop mutant and (b) Alpha Helix mutant DHFR. Crystal structure from PDB 1RX2 with backbone shown in cartoon view (grey), substrate dihydrofolate in stick view (pink), and cofactor NADPH in stick view (orange). (c) Initial rate data for free protein when [DHFR] = 10 nM, [DHF] = 50 μM, and [NADPH] = 50 μM at 37°C. Yellow = WT DHFR. Green = FG Loop mutant. Blue = Alpha Helix mutant.[39] Reproduced with permission from: Kozlowski, R. B.; Ragupathi, A.; Dyer, R. B. Characterizing the Surface Coverage of Protein-Gold Nanoparticle Bioconjugates. *Bioconjugate Chem.* **2018**, *29*, 2691–2700. Copyright 2018, American Chemical Society.

AuNP Synthesis. Citrate stabilized AuNPs with a diameter of 15 nm were synthesized via the citrate reduction method.[41] TEM was used to characterize the synthesized AuNPs, and the size of the AuNPs was analyzed with ImageJ (**Figure 2.6** and **Figure 3.3**), giving an average particle size distribution of 14.1 ± 1.4 nm. Citrate stabilized 5 nm and 30 nm AuNPs were purchased from Nanocomposix (San Diego, CA) and used without modification.

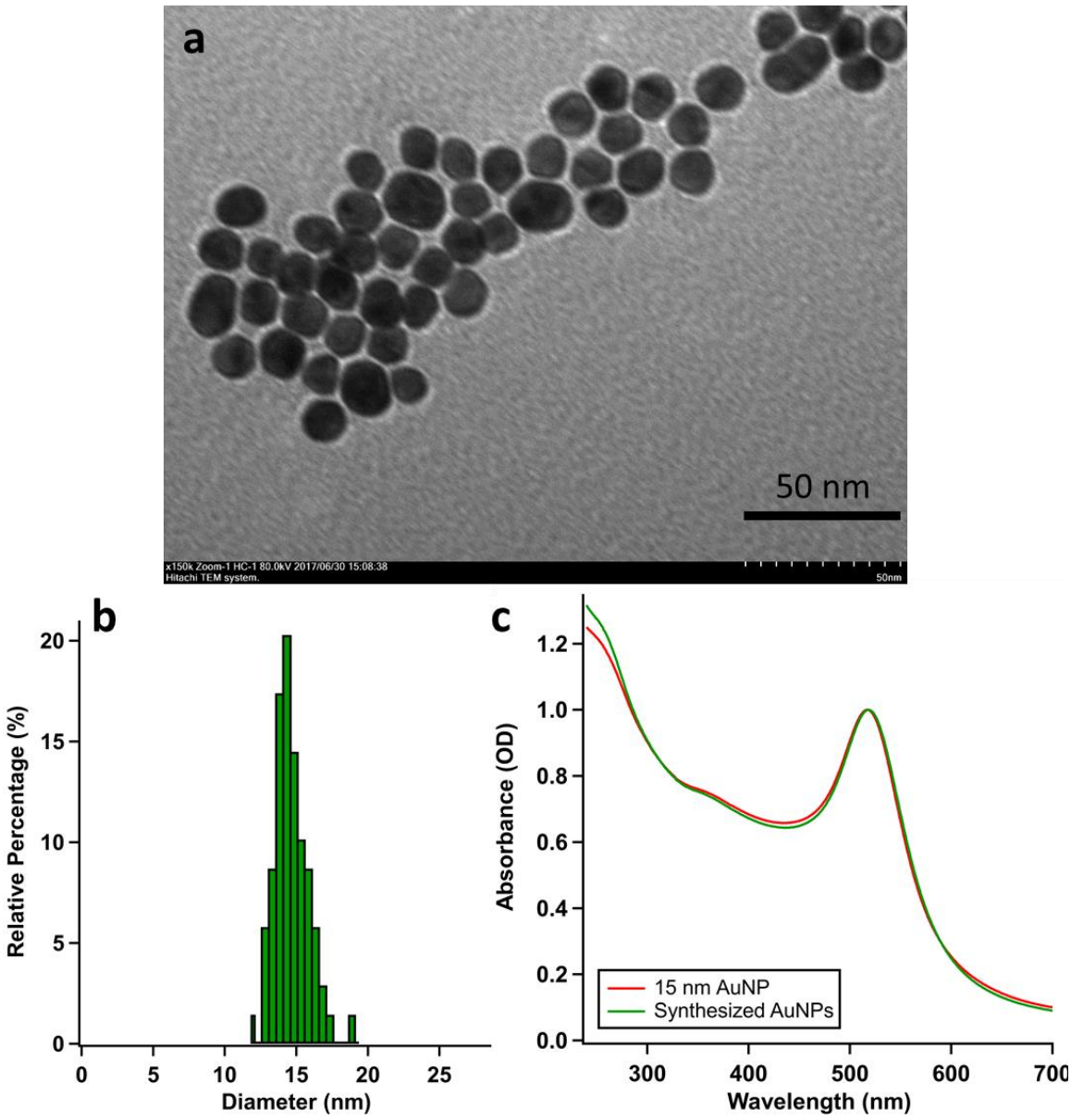

Figure 3.3: Characterization of 15 nm AuNPs.

Characterization includes TEM, DLS, and UV/Vis absorption spectroscopy. (a) TEM image of synthesized AuNPs. The scale bar is 50 nm. (b) Particle size distribution. The TEM images were analyzed with ImageJ. Sizes of 75 AuNPs were measured, and the size distribution was plotted in 0.5 nm increments. The average diameter of the AuNPs is 14.1 ± 1.4 nm. **(c)** UV/Vis absorption spectra of synthesized AuNPs (green) and 15 nm AuNPs bought from Nanocomposix (red). Reproduced with permission from: Kozlowski, R. B.; Ragupathi, A.; Dyer, R. B. Characterizing the Surface Coverage of Protein-Gold Nanoparticle Bioconjugates. *Bioconjugate Chem.* **2018**, *29*, 2691–2700. Copyright 2018, American Chemical Society.

Protein-AuNP Conjugation and Isolation. DHFR was conjugated to AuNPs through covalent binding with the surface cysteine as shown in **Figure 3.1**. A large excess of protein was added to AuNPs in the binding step, which means most of the protein was not bound to the AuNPs. The free protein was separated from the conjugates via centrifugation, which pellets the conjugates and leaves the remaining unbound protein and displaced citrate in the supernatant. Multiple rounds of centrifugation and washing with 0.005% Tween 20, 10 mM sodium phosphate, pH 7.0 buffer removed the free protein. The conjugates were then stored in the same buffer at 4°C until characterized.

Section 3-2.2: Covalent Attachment of Protein to Gold Nanoparticles

There are three lines of evidence that support covalent attachment rather than nonspecific chemisorption of DHFR to AuNPs. First, we have introduced surface Cys into the DHFR structure in positions that are highly exposed. Furthermore, we have tested whether these Cys are chemically active by labeling these positions with a thiol reactive dye, Badan (6-Bromoacetyl-2-dimethylaminonapthalene). Attachment efficiency of the Badan dye to the E120CCys and E101CCys mutants is >90%, which indicates that the surface Cys is highly reactive in both cases. Second, reactive thiols (thiolates) invariably form strong covalent bonds with a gold surface. Covalent attachment of proteins to Au surfaces through reactive Cys has been established for many proteins, including cytochrome c, glucose oxidase, and Protein G.[26-28] Therefore, it is highly likely that since our DHFR constructs have reactive surface Cys they will form covalent attachments with a gold surface.

Finally, we conducted a series of control experiments to verify covalent attachment (**Figure 3.4**). Protein that is covalently bound on a gold surface cannot be removed by denaturing the protein or by the introduction of high salt concentration, whereas such treatment often removes chemisorbed protein. Furthermore, introduction of high salt concentration to AuNPs that are not stabilized by bound protein causes AuNPs to aggregate and crash out of solution, a process that is easily detected by a color change from pink to blue. Capping the AuNP binding sites and exposed thiols on the protein with an excess of 2-mercaptoethanol (βME) blocks covalent attachment of the protein. These properties of the protein-AuNP conjugates can be used to test the mode of attachment. When covalent attachment of DHFR is blocked with βME, addition of a high concentration of salt causes the nanoparticles to immediately aggregate, with an associated color change (**Figure 3.4a**). Without βME, addition of the same large excess of salt does not crash out the AuNPs because the covalently bound DHFR stabilizes them in this case. This same effect is observed when the protein is denatured in preparation for an SDS-PAGE gel. The βME containing conjugate samples aggregate upon denaturation of DHFR, whereas this is not the case for the samples without βME, due to covalent attachment of the protein (**Figure 3.4b**). SDS-PAGE of these samples shows that only the DHFR-AuNP conjugates and DHFR-AuNP + NaCl samples are stable (**Figure 3.4c**). After staining the gel, free protein can be seen in the lanes containing DHFR-AuNP + βME and DHFR-AuNP + βME + NaCl lanes, indicating that the protein is not bound to the AuNPs in the presence of βME (**Figure 3.4d**). These results demonstrate that the DHFR-AuNP conjugates contain protein that is covalently bound to the AuNPs.

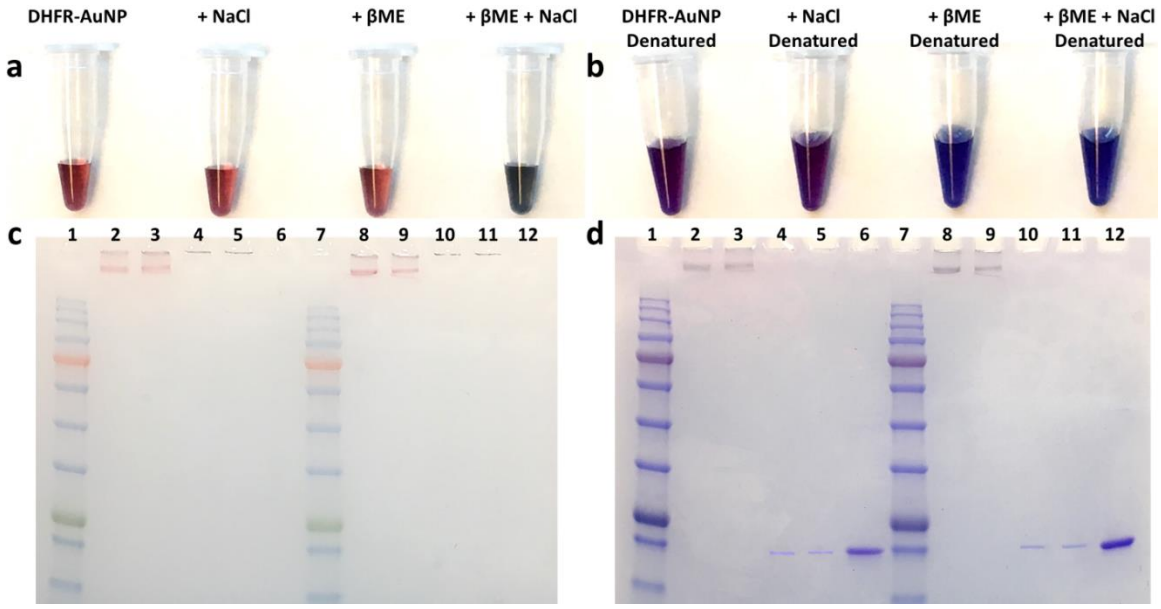

Figure 3.4: Evidence for Covalent Binding of Protein to AuNPs.

a. Pictures of samples 1 hour after preparation. The first tube contains the standard DHFR-AuNP conjugates. Tube 2 is standard conjugates with 1 M NaCl added. Tube 3 is standard conjugates in 10 mM βME, which caps the gold binding sites on the AuNPs as well as the thiols on the protein. Tube 4 is standard conjugates with 10 mM βME and 1 M NaCl. Tubes 1-3 have the identical pink color of conjugates, which shows that the addition of βME does not prevent the electrostatic binding of the protein to AuNPs. In tube 4, clear aggregation can be seen, where the AuNPs turn purple, demonstrating that the electrostatically bound protein (like in tube 3) is not sufficient to stabilize the AuNPs from the high salt concentration. The addition of salt to covalently bound protein to AuNPs does not aggregate the AuNPs. **b.** A similar effect of the addition of salt to βME containing conjugates can be obtained when denaturing the protein. Laemmli sample buffer is added to all conjugate samples to denature the protein before running the SDS-PAGE gels. After boiling these samples for 5 minutes (followed by icing for 5 minutes), tubes 1 and 2 have a similar color appearance, with a purple tint. Tubes 3 and 4 are blue in color, rather than purple, indicating that the denaturing of electrostatically bound protein on AuNPs causes AuNP aggregation due to non-covalent protein stabilization. **c.** Unstained gel of samples. Lanes 1 and 7 are protein ladder. Lanes 2-5 are for FG Loop-15 nm AuNP conjugates, and lanes 8-11 are for Alpha Helix-15 nm AuNP conjugates. Lane 6 is free FG Loop DHFR, and lane 12 is free Alpha Helix DHFR. Lanes 2 and 8 are standard DHFR-AuNP conjugates, lanes 3 and 9 are DHFR-AuNP conjugates + NaCl, lanes 4 and 10 are DHFR-AuNP conjugates + βME, and lanes 5 and 11 are DHFR-AuNP conjugates + βME + NaCl. It is clear that stable conjugates are present in lanes 2-3 and 8-9, while the AuNPs have aggregated in lanes 4-5 and 8-9.

d. Stained gel of the samples. Lane assignments are described in **c.** Here, it is evident that there is protein bound to AuNPs in lanes 2-3 and 8-9, by the color of the conjugates turning from pink in **c** to purple. Further, there is clearly free, unbound protein present in lanes 4-5 and 10-11, indicating that the βME/denaturing process causes the protein to leave the surface of the AuNPs, where the AuNPs then aggregate.[39] Reproduced with permission from: Kozlowski, R. B.; Ragupathi, A.; Dyer, R. B. Characterizing the Surface Coverage of Protein-Gold Nanoparticle Bioconjugates. *Bioconjugate Chem.* **2018**, *29*, 2691–2700. Copyright 2018, American Chemical Society.

Section 3-2.3: Characterization of Protein-Gold Nanoparticle Conjugates

SDS-PAGE of Conjugates. SDS-PAGE of the conjugates was used to determine if the AuNPs are indeed bound to protein, as well as to determine the efficiency of removal of the free protein from conjugates. The unstained gel (**Figure 3.5**) shows that DHFR-AuNP conjugates run on the gel (lanes 2-7) and are pink in color, while unbound AuNPs aggregate in the well (lanes 8-10) and are black in color. The free AuNPs actually aggregate immediate upon addition to loading buffer, as they are weakly capped with citrate and salt easily destabilizes them. The absence of aggregation in the case of the conjugates indicates that they are stabilized relative to citrate capped AuNPs, confirming that the protein is covalently attached to AuNPs and not just electrostatically bound. The 5 nm AuNP-DHFR conjugates run the fastest and 30 nm AuNP-DHFR conjugates run the slowest, as expected based on size. Coomassie Blue stain was used to detect the presence of protein. In the stained gel (**Figure 3.6**), the pink conjugates turn purple, which indicates the presence of protein directly on the AuNPs. The free protein bands run at approximately 21 kDa in lanes 11-12, and these free protein bands are not present in any of the conjugate lanes, indicating that there is no (within the detection limit) free protein in the conjugate samples after

separation and washing. The detection limit of a stained protein band on the gel is approximately 3% of the AuNP bound protein concentration.

Figure 3.5: Unstained SDS-PAGE Gel.

Lane 1 is protein marker. Lanes 2-3 are DHFR-5 nm AuNP conjugates. Lanes 4-5 are DHFR-15 nm AuNP conjugates. Lanes 6-7 are DHFR-30 nm AuNP conjugates. Lanes 8-10 are free AuNPs: 5 nm, 15 nm, and 30 nm. Lanes 11-12 are free protein. The DHFR-AuNP conjugates are pink in color, indicating their stability. The smaller AuNP conjugates run faster on the gel than the larger AuNP conjugates. The free citrate stabilized AuNPs are deep purple and did not leave the wells during the run cycle of the gel. These AuNPs aggregated immediately upon addition to the well, indicating that the AuNPs in lanes 2-7 are indeed bound to protein. The gel is unstained, so no sample is visible in the free protein lanes. FG = FG Loop mutant. AH = Alpha Helix mutant. In the samples run on the gel, the concentration of protein on the AuNPs is on average 900 ng, and the detection limit of the Coomassie Blue stain is known to be 30 ng. Thus, the detection limit is approximately 3% of the AuNP bound protein concentration.[39] Reproduced with permission from: Kozlowski, R. B.; Ragupathi, A.; Dyer, R. B. Characterizing the Surface Coverage of Protein-Gold Nanoparticle Bioconjugates. *Bioconjugate Chem.* **2018**, *29*, 2691–2700. Copyright 2018, American Chemical Society.

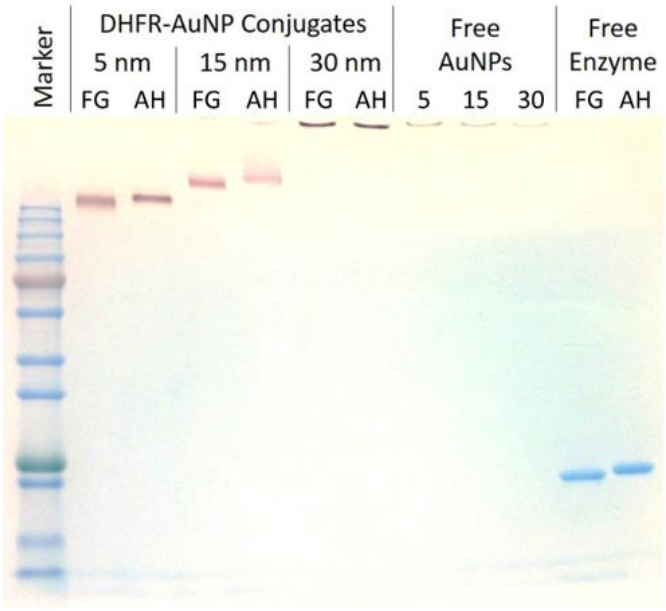

Figure 3.6: Stained SDS-PAGE Gel.

SDS-PAGE gel of DHFR-AuNP conjugates and free DHFR. Lane 1 is protein marker. Lanes 2-3 are 5 nm AuNP-DHFR conjugates. Lanes 4-5 are 15 nm AuNP-DHFR conjugates. Lanes 6-7 are 30 nm AuNP-DHFR conjugates. Lanes 8-10 are free AuNPs: 5 nm, 15 nm, and 30 nm. Lanes 11-12 are free protein. FG = FG Loop mutant. AH = Alpha Helix mutant.[39] Reproduced with permission from: Kozlowski, R. B.; Ragupathi, A.; Dyer, R. B. Characterizing the Surface Coverage of Protein-Gold Nanoparticle Bioconjugates. *Bioconjugate Chem.* **2018**, *29*, 2691–2700. Copyright 2018, American Chemical Society.

UV/Vis Absorption Spectra of Conjugates. UV/Vis spectrophotometry was used to verify the replacement of the citrate capping ligands with protein on the AuNP surface. For free citrate stabilized 5 nm AuNPs, the SPR absorbance maximum is at 515 nm. When protein has replaced citrate, the SPR band redshifts due to the change in dielectric constant of the molecules on the surface of the AuNP. This redshift is approximately 6 nm, to 521 nm (**Figure 3.7a**). The SPR shift for the 15 nm AuNP conjugates is from 518 nm to 523 nm (**Figure 3.7b**), and for 30 nm AuNP conjugates, the shift is from 520 nm to 524 nm (**Figure 3.7c**). These SPR redshifts from free AuNPs to DHFR-AuNP conjugates are

consistent for both the FG Loop mutant and Alpha Helix mutant conjugates, which indicates that the protein is indeed bound to the AuNP surfaces.

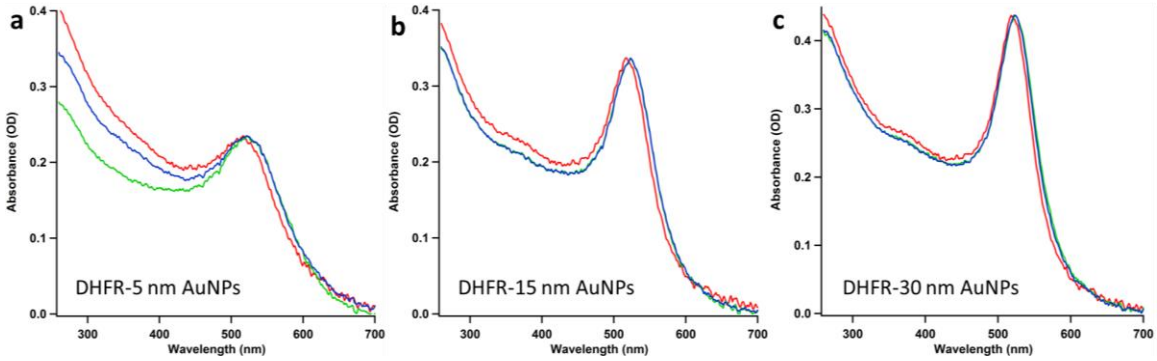

Figure 3.7: UV/Vis Absorption Spectra of DHFR-AuNP Conjugates.

a. 5 nm AuNP conjugates. SPR shift from 515 nm to 521 nm upon protein conjugation. b. 15 nm AuNP conjugates. SPR shift from 518 nm to 523 nm. **c.** 30 nm AuNP conjugates. SPR shift from 520 nm to 524 nm. Red = Free AuNPs. Green = FG Loop mutant conjugates. Blue = Alpha Helix mutant conjugates.[39] Reproduced with permission from: Kozlowski, R. B.; Ragupathi, A.; Dyer, R. B. Characterizing the Surface Coverage of Protein-Gold Nanoparticle Bioconjugates. *Bioconjugate Chem.* **2018**, *29*, 2691–2700. Copyright 2018, American Chemical Society.

Dynamic Light Scattering. Dynamic Light Scattering (DLS) was used to determine the hydrodynamic diameter of the AuNPs and conjugates. DLS measures the rate of diffusion of particles through a confocal observation volume that is defined by imaging the scattered light through a pinhole. This diffusion rate is then used to calculate the hydrodynamic diameter of the particles. It is difficult to measure the smallest particle size (5 nm) with conventional DLS instruments that employ a red light-source, so we applied this technique to characterize all samples except free 5 nm AuNPs. The time decay of the autocorrelation function (ACF) of the scattering signal is plotted for free AuNPs and conjugates in **Figure 3.8a-c**. The ACF decay is slower for the conjugates than for free

AuNPs, as expected for larger, slower diffusing particles. The plot of the intensity distributions (inset of **Figure 3.8a-c**) shows narrow size distributions for free AuNPs, centered at 18 nm and 35 nm for the 15 nm and 30 nm AuNPs, respectively. The DLS measurement determines hydrodynamic diameters from diffusion rates, which are slightly higher than the physical diameter determined by TEM. The intensity distributions of 5 nm AuNP-FG Loop and Alpha Helix conjugates (**Figure 3.8a**) are centered at 16.5 nm and 19.4 nm, respectively, where the slight difference could be due to the higher concentration of conjugates required to obtain DLS data with the smaller particles. Both 15 nm AuNP-DHFR conjugates have intensity distributions centered at 27 nm and are slightly broader than the free AuNP distribution. A similar increase in size to 48 nm is observed for 30 nm AuNP-FG Loop conjugates and to 46 nm for 30 nm AuNP-Alpha Helix conjugates. The roughly 9-12 nm increase in hydrodynamic diameter for the DHFR-AuNP conjugates is consistent with the known structural properties of DHFR. The physical diameter of DHFR is at maximum 3.5 nm,[7] and the hydrodynamic diameter is somewhat larger (4.5 nm), therefore the measured hydrodynamic diameters of the conjugates indicate a monolayer or slightly sub-monolayer of protein bound to the AuNP.

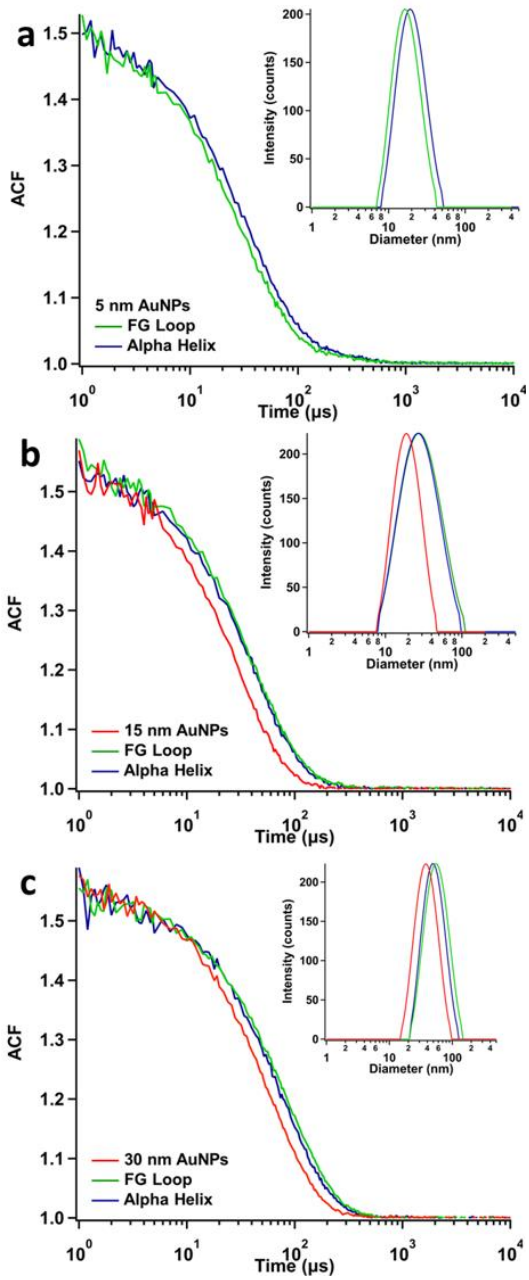

Figure 3.8: DLS of DHFR-AuNP conjugates.

(a) 5 nm AuNP conjugates: (Green) FG loop conjugates (16.5 nm), (Blue) Alpha Helix conjugates (19.4 nm). Free AuNPs are too small to obtain accurate DLS measurements. **(b)** 15 nm AuNP conjugates: (Red) free 15 nm AuNPs (18 nm), both AuNP-DHFR conjugates (27 nm). **(c)** 30 nm AuNP conjugates: free 30 nm AuNPs (35 nm), FG loop conjugates (48 nm), Alpha Helix conjugates (46 nm).[39] Reproduced with permission from: Kozlowski, R. B.; Ragupathi, A.; Dyer, R. B. Characterizing the Surface Coverage of Protein-Gold Nanoparticle Bioconjugates. *Bioconjugate Chem.* **2018**, *29*, 2691–2700. Copyright 2018, American Chemical Society.

Section 3-2.4: Protein Concentration Determination of Conjugates

Currently, there is very little information in the literature regarding the determination of protein concentration on AuNPs at low surface coverage; however, this information is crucial to understanding bioconjugate function and stability. The most common methods for quantifying protein concentration are spectrophotometric, using the intrinsic UV absorption of the protein at 280 nm or the visible absorption at 595 nm in a Bradford assay. The strong absorption and scattering background of AuNPs introduce large errors into these methods, however, making them unsuitable for application to protein-AuNP conjugates. The method we have developed for protein concentration determination in protein-AuNP conjugates is a fluorescence assay (**Figure 3.9**), following the dissolution of AuNPs with potassium cyanide (KCN) (**Figure 3.9a**).[42] When KCN is added to a sample of conjugates, KCN and Au atoms form a complex, dissolving the AuNPs and leaving the protein free in solution. The dissolution of the AuNPs removes the absorption and scattering spectral contributions due to the particles.[42] The protein in this state (for this sample) is too dilute to measure via standard UV/Vis absorption, so the much more sensitive fluorescence detection is used. WT DHFR has five intrinsic tryptophan residues, so there is a strong native fluorescence signal that can be used to quantify the amount of protein. Additionally, fluorescence spectroscopy intrinsically has zero background, so it is much more sensitive than absorption spectroscopy.

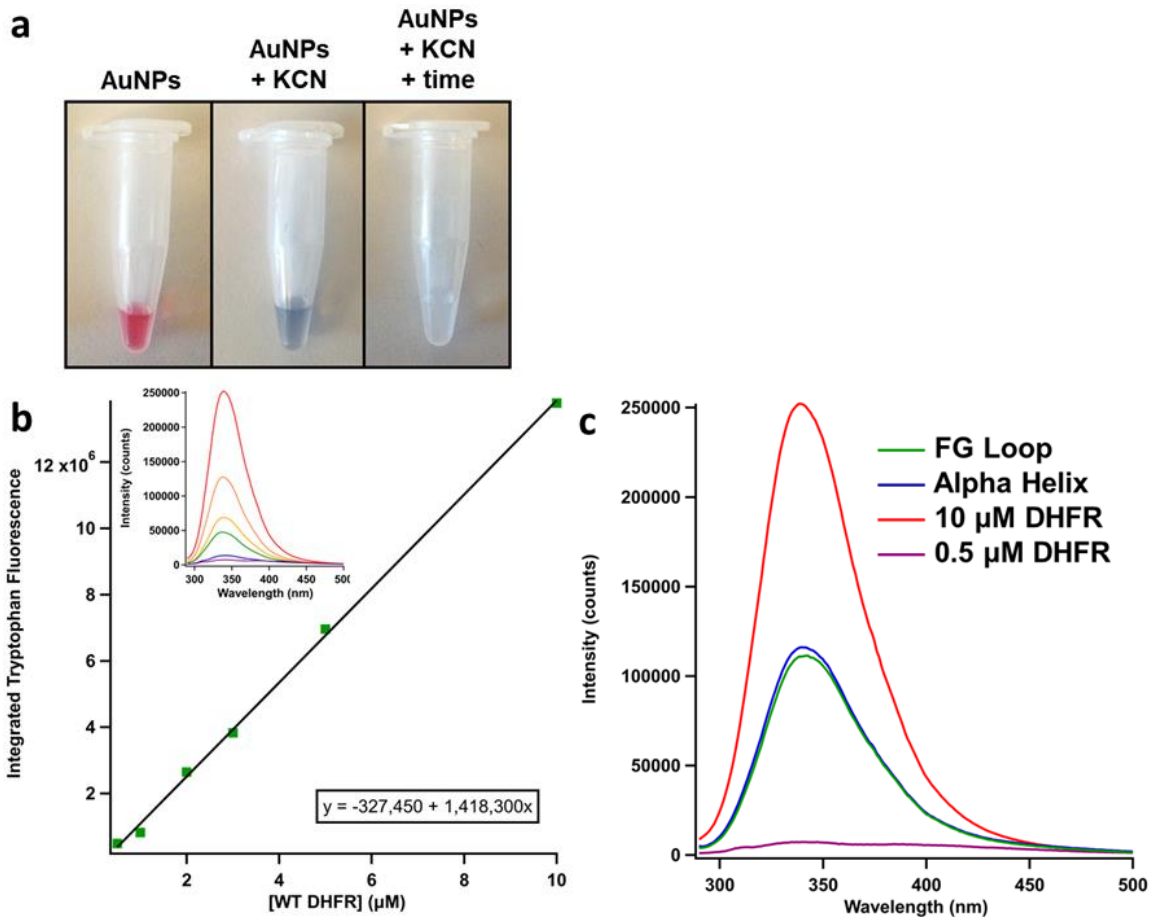

Figure 3.9: Fluorescence Assay.

Assay for protein concentration determination on the AuNPs. a. Left: DHFR-AuNP conjugates are stable, as indicated by their pink color. Middle: Immediately after the addition of KCN, the AuNPs start to aggregate, indicated by the deep purple/blue color. Right: After reacting for 1 hour, the AuNPs are dissolved and are now Au-KCN complexes, showing no visible color. **b.** Standard curve for WT DHFR protein samples under identical conditions as the unknown conjugate samples (same KCN and Tween 20 concentrations). The inset shows the fluorescence spectra obtained with 280 nm excitation. The area under each curve integrated from 300 to 385 nm is plotted versus the respective concentration to form the standard curve. **c.** The tryptophan fluorescence spectra for the conjugate samples bounded by the upper and lower ends of the calibration curve [WT DHFR]. The area under each conjugate spectrum is used in conjunction with the standard curve equation to determine the concentration of protein in the AuNP samples. Green = FG Loop conjugates. Blue = Alpha Helix conjugates.[39] Reproduced with permission from: Kozlowski, R. B.; Ragupathi, A.; Dyer, R. B. Characterizing the Surface Coverage of Protein-Gold Nanoparticle Bioconjugates. *Bioconjugate Chem.* **2018**, *29*, 2691–2700. Copyright 2018, American Chemical Society.

Known concentrations of WT DHFR samples were used to create a calibration curve, prepared in the same manner as the conjugate samples, including identical additions of TCEP, Tween 20, and KCN (**Figure 3.9b**). The fluorescence spectra are taken with 280 nm excitation to excite the tryptophan residues, and the tryptophan emission peak is centered at approximately 340 nm. The area under the emission curve is plotted versus the respective protein concentration. The linear fit of this calibration curve is used to determine the protein concentration in the conjugate samples, which were also excited at 280 nm and analyzed in the same manner as the WT DHFR standards (**Figure 3.9c**).

The pelleting and washing of the protein-AuNPs is necessary to remove free protein from the bioconjugates. However, some conjugates are lost in the process of removing the supernatant, as it is performed by pipetting the supernatant away from the pellet, so there is a balance between efficient removal of free protein and loss of conjugates. To limit loss of conjugates, narrow pipette tips can be used during supernatant removal when the level is close to the pellet. Three centrifugation steps are sufficient for washing the conjugates without losing much sample, as the free protein is below the detection limit in the SDS-PAGE gel (**Figure 3.9**). Consistent protein concentrations, typically in the range of 3-5 μM, are obtained with this method for many repetitions of the conjugate preparation.

Section 3-2.5: Surface Coverage of Conjugates

The first step in characterizing the surface coverage of the protein-AuNP conjugates is to determine the molar ratio of bound protein to AuNP. The number of moles of protein is determined from the concentration assay described above. The UV/Vis absorption spectrum of the conjugates provides the AuNP concentration, and therefore moles of

AuNPs ($\varepsilon_{521\ nm}$ = 1.10 x 10^7 $M^{-1}cm^{-1}$ for 5 nm AuNPs, $\varepsilon_{523\ nm}$ = 3.67 x 10^8 $M^{-1}cm^{-1}$ for 15 nm AuNPs, $\varepsilon_{524\ nm}$ = 3.36 x 10^9 $M^{-1}cm^{-1}$ for 30 nm AuNPs). The molar ratio of protein to AuNPs is summarized for each of the conjugates in **Table 3.1**. This method has been tested on many different conjugate preparations, and the ratio of DHFR to AuNPs is reproducible, with standard deviations equal to or less than 10% of the protein:AuNP ratio.

Table 3-1: Surface Coverage of DHFR-AuNP Conjugates.

The number of proteins per AuNP is shown with respective standard deviations, as well as the surface coverage for each type of conjugates.[39] Reproduced with permission from: Kozlowski, R. B.; Ragupathi, A.; Dyer, R. B. Characterizing the Surface Coverage of Protein-Gold Nanoparticle Bioconjugates. *Bioconjugate Chem.* **2018**, *29*, 2691–2700. Copyright 2018, American Chemical Society.

	Proteins Per AuNP* **Surface Coverage Percentage**		
Mutant	**5 nm AuNPs**	**15 nm AuNPs**	**30 nm AuNPs**
FG Loop Conjugates	7 ± 1 89%	35 ± 4 50%	180 ± 10 63%
Alpha Helix Conjugates	7 ± 1 89%	34 ± 4 48%	183 ± 11 65%

*The uncertainty is determined from the standard deviation of at least 3 separate conjugate preparations.

Surface area calculations are an important test of whether the experimentally determined ratio of protein to AuNP is physically reasonable. Further, the surface coverage

is different for difference sizes of AuNPs. In this dissertation, AuNPs with diameters of 5 nm, 15 nm, and 30 nm were used to characterize surface coverages (**Figure 3.10**).

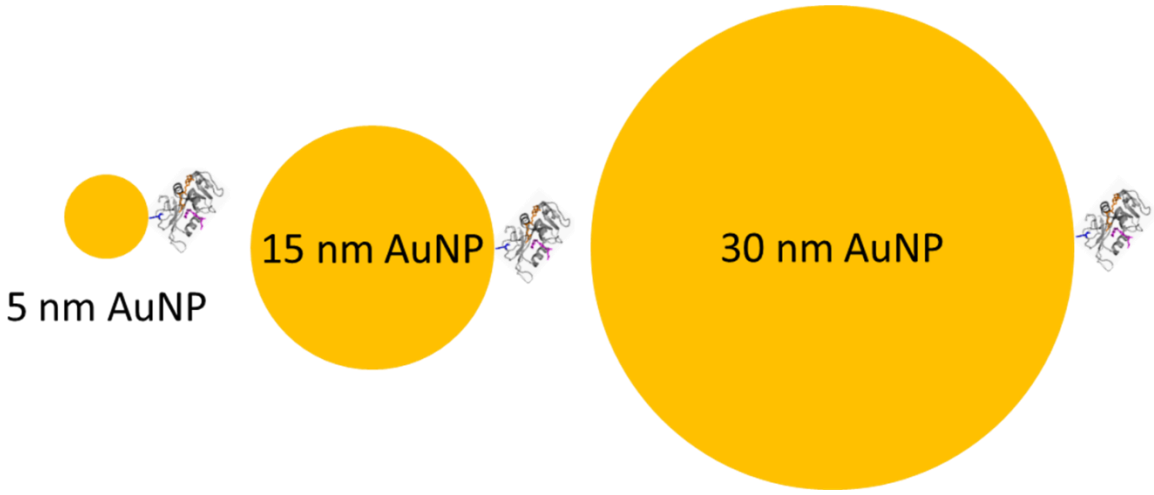

Figure 3.10: Protein Size on Different AuNP Sizes.

Schematic of DHFR and different AuNP diameters (5 nm, 15 nm, and 30 nm), to scale. The length of DHFR is roughly the same as the diameter of 5 nm AuNPs. Larger AuNPs can fit more proteins on the surface.

The surface area of the protein is taken to be a rectangle of 2.5 nm by 4 nm based on the binding geometry (**Figure 3.11**), which is 10 nm^2. The surface area of the AuNPs is calculated to be 78 nm^2 for 5 nm AuNPs, 707 nm^2 for 15 nm AuNPs, and 2,827 nm^2 for 30 nm AuNPs. The maximum number of proteins that can fit on the AuNPs is calculated by dividing the surface area of the AuNP by the surface area of the protein. With this simplifying assumption, the maximum possible number of bound DHFR molecules is 8 for the 5 nm AuNPs, 70 for the 15 nm AuNPs, and 282 for the 30 nm AuNPs. These numbers represent an upper bound because the calculation assumes no empty space in the packing of the protein molecules on the surface, which is of course not possible. In addition, the actual contact area of the protein with AuNP surface is probably less than the rectangular

cross section used in the calculation. All of the experimentally determined ratios of protein to AuNPs are less than the upper bound determined from this simplified model, consistent with a monolayer or sub-monolayer of protein on the surface, in agreement with the DLS results.

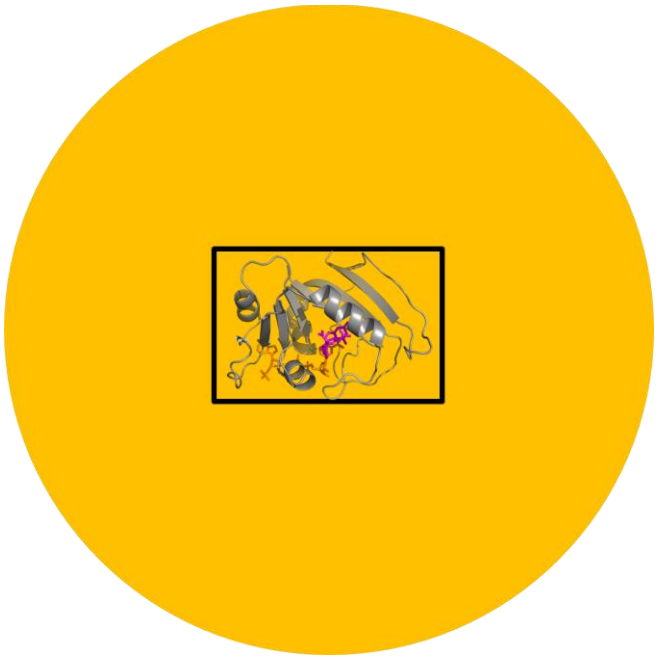

Figure 3.11: 2-D Representation of DHFR on a 15 nm AuNP.

DHFR is approximately the size of a 2.5x4 nm rectangle. Here, a visual of the size of DHFR on the surface of a 15 nm AuNP.

The surface coverage of the protein on the AuNPs (**Table 3.1**) is determined by dividing the experimentally determined number of proteins per AuNP by the maximum number of proteins that can bind based on the surface area. The average surface coverage is 89% for DHFR-5 nm AuNP conjugates, 49% for DHFR-15 nm AuNP conjugates, and 64% for DHFR-30 nm AuNP conjugates. The DLS results indicate that there is at most a

monolayer of protein on each AuNP, consistent with these calculated surface coverages. Furthermore, the protein surface coverage appears to be related to the size of the AuNP. We postulate that the surface coverage is correlated to the curvature of the surface (which depends on the size of the nanoparticle) due to protein-protein steric effects. The greater the surface curvature, the more volume is available to pack proteins on the nanoparticle surface. Thus, we attribute the nearly 100% surface coverage for 5 nm AuNP conjugates to its high curvature (relative to the size of the protein) that minimizes steric clash of bound proteins. When the radius of curvature decreases with the increasing AuNP size, there is more steric interaction of bound proteins, restricting the number that can bind, which is demonstrated by the 50-60% surface coverage in 15 nm and 30 nm AuNP conjugates. As the nanoparticle becomes large compared to the size of the protein, this effect is expected to saturate, which could explain the minimal difference between surface coverage in the larger conjugates. A similar protein crowding effect is observed for proteins bound on membrane vesicle surfaces; at high protein surface coverage, the steric pressure is sufficient to drive nanotubule formation, which relieves the steric pressure by creating a much greater surface curvature of the membrane.[43, 44] Thus, it is important to consider how curvature impacts surface coverage in bioconjugate systems, and the methods presented herein allow for the accurate quantification of parameters to determine surface coverage of protein-AuNP conjugates.

Section 3-3: Chapter 3 Conclusions

In this chapter, we present a thorough protein-AuNP bioconjugate characterization methodology using SDS-PAGE, UV/Vis absorption, DLS and most importantly, an accurate method for surface coverage determination. The characterization scheme was applied to DHFR-AuNP conjugates of three different AuNP sizes: 5, 15, and 30 nm, as a means of varying the surface curvature and surface coverage. We show that the protein-AuNP conjugates were successfully synthesized, only a monolayer of protein is bound to the nanoparticles, and free protein was removed in the washing steps. We also present a novel methodology for accurately determining the protein concentration on AuNPs using KCN dissolution and a fluorescence assay. The conjugate synthesis is reproducible, with a consistent average surface coverage per AuNP. Further, the surface coverage of proteins on the AuNPs seems to be related to the curvature of the AuNP. There is higher surface coverage with smaller AuNPs, which have greater curvature and allow for higher loading density due to sterics. For larger AuNPs, (smaller surface curvature) steric crowding of the attached proteins increases, causing a decrease in surface coverage on the AuNP.

In summary, a thorough characterization of the surface coverage in protein-nanoparticle conjugates is key to understanding their functionality, particularly enzyme activity. The integrated characterization methodology developed in this work to determine surface coverage can be applied to many other types of protein-nanoparticle conjugates. The methods of detection are UV/Vis absorption and fluorescence for these AuNPs, which can be used for not only protein detection, but also for DNA detection. Further, the developed protocols could be broadly applied to other systems, such as silver nanoparticles

and quantum dots, where just the KCN step for concentration determination would need to be modified.

Section 3-4: Chapter 3 References

1. Ghosh, P.; Han, G.; De, M.; Kim, C. K.; Rotello, V. M., Gold nanoparticles in delivery applications. *Adv. Drug Del. Rev.* **2008,** *60* (11), 1307-1315.

2. Medintz, I. L.; Uyeda, H. T.; Goldman, E. R.; Mattoussi, H., Quantum dot bioconjugates for imaging, labelling and sensing. *Nature Mater.* **2005,** *4*, 435-446.

3. Grzelczak, M. P.; Danks, S. P.; Klipp, R. C.; Belic, D.; Zaulet, A.; Kunstmann-Olsen, C.; Bradley, D. F.; Tsukuda, T.; Viñas, C.; Teixidor, F.; Abramson, J. J.; Brust, M., Ion Transport across Biological Membranes by Carborane-Capped Gold Nanoparticles. *ACS Nano* **2017,** *11* (12), 12492-12499.

4. Jain, P. K.; Lee, K. S.; El-Sayed, I. H.; El-Sayed, M. A., Calculated Absorption and Scattering Properties of Gold Nanoparticles of Different Size, Shape, and Composition: Applications in Biological Imaging and Biomedicine. *J. Phys. Chem. B* **2006,** *110* (14), 7238-7248.

5. Hutter, E.; Maysinger, D., Gold-nanoparticle-based biosensors for detection of enzyme activity. *Trends Pharmacol. Sci.* **2013,** *34* (9), 497-507.

6. Zong, J.; Cobb, S. L.; Cameron, N. R., Peptide-functionalized gold nanoparticles: versatile biomaterials for diagnostic and therapeutic applications. *Biomater. Sci.* **2017,** *5*, 872-886.

7. Ditzler, L. R.; Sen, A.; Gannon, M. J.; Kohen, A.; Tivanski, A. V., Self-Assembled Enzymatic Monolayer Directly Bound to a Gold Surface: Activity and Molecular Recognition Force Spectroscopy Studies. *J. Am. Chem. Soc.* **2011,** *133* (34), 13284-13287.

8. Dreaden, E. C.; Austin, L. A.; Mackey, M. A.; El-Sayed, M. A., Size matters: gold nanoparticles in targeted cancer drug delivery. *Ther. Deliv.* **2012,** *3* (4), 457-478.

9. Zhou, J.; Patel, T. R.; Sirianni, R. W.; Strohbehn, G.; Zheng, M.-Q.; Duong, N.; Schafbauer, T.; Huttner, A. J.; Huang, Y.; Carson, R. E.; Zhang, Y.; Sullivan, D. J., Jr.; Piepmeier, J. M.; Saltzman, W. M., Highly penetrative, drug-loaded nanocarriers improve treatment of glioblastoma. *Proc. Natl. Acad. Sci. U.S.A.* **2013,** *110* (29), 11751-11756.

10. Alkilany, A. M.; Thompson, L. B.; Boulos, S. P.; Sisco, P. N.; Murphy, C. J., Gold nanorods: Their potential for photothermal therapeutics and drug delivery, tempered by the complexity of their biological interactions. *Adv. Drug Del. Rev.* **2012,** *64* (2), 190-199.

11. Sharma, P.; Brown, S.; Walter, G.; Santra, S.; Moudgil, B., Nanoparticles for bioimaging. *Adv. Colloid Interface Sci.* **2006,** *123-126*, 471-485.

12. Dreaden, E. C.; Alkilany, A. M.; Huang, X.; Murphy, C. J.; El-Sayed, M. A., The golden age: gold nanoparticles for biomedicine. *Chem. Soc. Rev.* **2012,** *41* (7), 2740-2779.

13. Rauta, P. R.; Hallur, P. M.; Chaubey, A., Gold nanoparticle-based rapid detection and isolation of cells using ligand-receptor chemistry. *Sci. Rep.* **2018,** *8* (1), 2893.

14. Kharlamov, A. N.; Feinstein, J. A.; Cramer, J. A.; Boothroyd, J. A.; Shishkina, E. V.; Shur, V., Plasmonic photothermal therapy of atherosclerosis with nanoparticles: long-term outcomes and safety in NANOM-FIM trial. *Future Cardiol.* **2017,** *13* (4), 345-363.

15. Sapsford, K. E.; Algar, W. R.; Berti, L.; Gemmill, K. B.; Casey, B. J.; Oh, E.; Stewart, M. H.; Medintz, I. L., Functionalizing Nanoparticles with Biological Molecules:

Developing Chemistries that Facilitate Nanotechnology. *Chem. Rev.* **2013,** *113* (3), 1904-2074.

16. Govorov, A. O.; Richardson, H. H., Generating heat with metal nanoparticles. *Nano Today* **2007,** *2* (1), 30-38.

17. Piella, J.; Bastús, N. G.; Puntes, V., Size-Dependent Protein–Nanoparticle Interactions in Citrate-Stabilized Gold Nanoparticles: The Emergence of the Protein Corona. *Bioconjugate Chem.* **2016,** *1*, 88-97.

18. Colangelo, E.; Comenge, J.; Paramelle, D.; Volk, M.; Chen, Q.; Lévy, R., Characterizing Self-Assembled Monolayers on Gold Nanoparticles. *Bioconjugate Chem.* **2016,** *1*, 11-22.

19. Lata, J. P.; Gao, L.; Mukai, C.; Cohen, R.; Nelson, J. L.; Anguish, L.; Coonrod, S.; Travis, A. J., Effects of Nanoparticle Size on Multilayer Formation and Kinetics of Tethered Enzymes. *Bioconjugate Chem.* **2015,** *26* (9), 1931-1938.

20. Hondred, J. A.; Breger, J.; Garland, N.; Oh, E.; Susumu, K.; Walper, S.; Medintz, I.; Claussen, J. C., Enhanced enzymatic activity from phosphotriesterase trimer gold nanoparticle bioconjugates for pesticide detection. *Analyst* **2017,** *142*, 3261-3271.

21. Vilanova, O.; Mittag, J. J.; Kelly, P. M.; Milani, S.; Dawson, K. A.; Rädler, J. O.; Franzese, G., Understanding the Kinetics of Protein–Nanoparticle Corona Formation. *ACS Nano* **2016,** *10* (12), 10842-10850.

22. Wang, J.; Jensen, U. B.; Jensen, G. V.; Shipovskov, S.; Balakrishnan, V. S.; Otzen, D.; Pedersen, J. S.; Besenbacher, F.; Sutherland, D. S., Soft Interactions at Nanoparticles Alter Protein Function and Conformation in a Size Dependent Manner. *Nano Lett.* **2011,** *11* (11), 4985-4991.

23. Cui, M.; Liu, R.; Deng, Z.; Ge, G.; Liu, Y.; Xie, L., Quantitative study of protein coronas on gold nanoparticles with different surface modifications. *Nano Research* **2014,** *7* (3), 345-352.

24. Schade, M.; Moretto, A.; Donaldson, P. M.; Toniolo, C.; Hamm, P., Vibrational Energy Transport through a Capping Layer of Appropriately Designed Peptide Helices over Gold Nanoparticles. *Nano Lett.* **2010,** *10* (8), 3057-3061.

25. Hassan, S.; Schade, M.; Shaw, C. P.; Lévy, R.; Hamm, P., Response of Villin Headpiece-Capped Gold Nanoparticles to Ultrafast Laser Heating. *J. Phys. Chem. B* **2014,** *118* (28), 7954-7962.

26. Aubin-Tam, M.-E.; Hwang, W.; Hamad-Schifferli, K., Site-Directed Nanoparticle Labeling of Cytochrome C. *Proc. Natl. Acad. Sci. U.S.A.* **2009,** *106* (11), 4095-4100.

27. Rodriguez-Quijada, C.; Sánchez-Purrà, M.; de Puig, H.; Hamad-Schifferli, K., Physical Properties of Biomolecules at the Nanomaterial Interface. *J. Phys. Chem. B* **2018,** *122* (11), 2827-2840.

28. Lee, J. M.; Park, H. K.; Jung, Y.; Kim, J. K.; Jung, S. O.; Chung, B. H., Direct Immobilization of Protein G Variants with Various Numbers of Cysteine Residues on a Gold Surface. *Anal. Chem.* **2007,** *79* (7), 2680-2687.

29. Liu, F.; Wang, L.; Wang, H.; Yuan, L.; Li, J.; Brash, J. L.; Chen, H., Modulating the Activity of Protein Conjugated to Gold Nanoparticles by Site-Directed Orientation and Surface Density of Bound Protein. *ACS Applied Materials & Interfaces* **2015,** *7* (6), 3717-3724.

30. Kuznetsova, I. M.; Turoverov, K. K.; Uversky, V. N., What Macromolecular Crowding Can Do to a Protein. *Int. J. Mol. Sci.* **2014,** *15* (12), 23090-23140.

31. Wieczorek, G.; Zielenkiewicz, P., Influence of Macromolecular Crowding on Protein-Protein Association Rates—a Brownian Dynamics Study. *Biophys. J.* **2008,** *95* (11), 5030-5036.

32. Phillip, Y.; Sherman, E.; Haran, G.; Schreiber, G., Common Crowding Agents Have Only a Small Effect on Protein-Protein Interactions. *Biophys. J.* **2009,** *97* (3), 875-885.

33. Keighron, J. D.; Keating, C. D., Enzyme:Nanoparticle Bioconjugates with Two Sequential Enzymes: Stoichiometry and Activity of Malate Dehydrogenase and Citrate Synthase on Au Nanoparticles. *Langmuir* **2010,** *26* (24), 18992-19000.

34. Liu, S.; Horak, J.; Höldrich, M.; Lämmerhofer, M., Accurate and reliable quantification of the protein surface coverage on protein-functionalized nanoparticles. *Anal. Chim. Acta* **2017,** *989*, 29-37.

35. Schneck, N. A.; Phinney, K. W.; Lee, S. B.; Lowenthal, M. S., Quantification of antibody coupled to magnetic particles by targeted mass spectrometry. *Anal. Bioanal. Chem.* **2016,** *408* (29), 8325-8332.

36. Grell, T. A. J.; Paredes, E.; Das, S. R.; Aslan, K., Quantitative Comparison of Protein Surface Coverage on Glass Slides and Silver Island Films in Metal-Enhanced Fluorescence-based Biosensing Applications. *Nano Biomed. Eng.* **2010,** *2* (3), 165-170.

37. Li, S.; Peng, Z.; Leblanc, R. M., Method To Determine Protein Concentration in the Protein–Nanoparticle Conjugates Aqueous Solution Using Circular Dichroism Spectroscopy. *Anal. Chem.* **2015,** *87* (13), 6455-6459.

38. Fierke, C. A.; Johnson, K. A.; Benkovic, S. J., Construction and evaluation of the kinetic scheme associated with dihydrofolate reductase from Escherichia coli. *Biochemistry* **1987,** *26* (13), 4085-92.

39. Kozlowski, R.; Ragupathi, A.; Dyer, R. B., Characterizing the Surface Coverage of Protein–Gold Nanoparticle Bioconjugates. *Bioconjug. Chem.* **2018,** *29* (8), 2691-2700.

40. Aldeek, F.; Safi, M.; Zhan, N.; Palui, G.; Mattoussi, H., Understanding the Self-Assembly of Proteins onto Gold Nanoparticles and Quantum Dots Driven by Metal-Histidine Coordination. *ACS Nano* **2013,** *7* (11), 10197-10210.

41. Hill, H. D.; Mirkin, C. A., The bio-barcode assay for the detection of protein and nucleic acid targets using DTT-induced ligand exchange. *Nature Protoc.* **2006,** *1* (1), 324-336.

42. Yehl, K.; Joshi, J. P.; Greene, B. L.; Dyer, R. B.; Nahta, R.; Salaita, K., Catalytic Deoxyribozyme-Modified Nanoparticles for RNAi-Independent Gene Regulation. *ACS Nano* **2012,** *6* (10), 9150-9157.

43. Stachowiak, J. C.; Hayden, C. C.; Sasaki, D. Y., Steric confinement of proteins on lipid membranes can drive curvature and tubulation. *Proc. Natl. Acad. Sci. U.S.A.* **2010,** *107* (17), 7781-7786.

44. Stachowiak, J. C.; Schmid, E. M.; Ryan, C. J.; Ann, H. S.; Sasaki, D. Y.; Sherman, M. B.; Geissler, P. L.; Fletcher, D. A.; Hayden, C. C., Membrane bending by protein–protein crowding. *Nat. Cell Biol.* **2012,** *14*, 944-949.

Chapter 4 – Driving Enzyme Dynamics with Light in Dihydrofolate Reductase-Gold Nanoparticle Conjugates

Section 4-1: Introduction

The role of protein dynamics in the mechanism of chemical catalysis by enzymes is a crucial but unresolved question,[1-4] in part due to the complexity of the protein energy landscape. Proteins are highly dynamic molecules,[5-7] but determining which protein motions might be coupled to catalysis has been very difficult because it has not been possible to excite such motions directly while observing the effect on catalysis. Protein motions that might affect catalysis range from local fluctuations of side chains to larger scale conformational changes (domain rotations or loop closures) and also span a wide range of timescales.[8-10] These motions can be divided into two general classes: ones directly coupled to crossing the transition state and ones that facilitate the search for reactive conformations. An example of the first type would be motions that modulate the donor to acceptor distance for hydride transfer on the timescale of crossing the transition state (10^{-13} – 10^{-12} s).[6, 8, 9] Such motions may be coherently coupled to catalysis. In contrast, motions involved in the search for the reactive conformation are slower, on the nanosecond to microsecond timescale, and they modulate the population of Michaelis state conformations rather than couple directly to catalysis.[11-13] Here we explore whether it is possible to directly excite this second class of motions in a model enzyme, DHFR, using laser induced heating of DHFR conjugated to a gold nanoparticle (AuNP).

AuNPs have been used previously as heat sources with thermophilic enzymes and peptides.[14-17] A laser is used to photoexcite the surface plasmon resonance (SPR) absorbance of the AuNP.[18-20] Electron-electron scattering leads to a relaxation of electrons, which results in a rapid temperature jump of the AuNP itself. Nonradiative cooling via electron-phonon coupling starts cooling the plasmon, and phonon-phonon coupling causes heat to dissipate into the surroundings.[21] Thermophilic enzyme-gold nanorod conjugates encapsulated in calcium alginate were excited with light, and due to the heat from the nanorod and encapsulation from the alginate, the activity of the thermophilic enzyme increased.[14] The mechanism of heat transfer through small peptides attached to AuNPs was studied using heat responsive labels on the peptide.[15] Heat transfer from the AuNP to the peptide was observed to occur through the single point of attachment of the peptide, producing a time-dependent heat distribution through the peptide. The initial anisotropic heat distribution evolved to an isotropic one as the heat transferred linearly through the backbone of the peptide. While these studies demonstrate that AuNPs can be used as heat sources for attached proteins, none have attempted to connect energy transfer from AuNPs to catalytically relevant enzyme dynamics.

Light excitation of bioconjugated enzyme to AuNPs allows for the study of heat transfer in the enzyme. Initially, the heat transfer from the AuNP is anisotropic, and we hypothesize that there will only be an effect from the heating if the heat is directly coupled to a catalytically active part of the protein. Additionally, the timescale of this initial anisotropic distribution must be faster than the thermal equilibration time across the entire enzyme. Our model enzyme is *E. coli* dihydrofolate reductase (ecDHFR), which has known motions, but the exact role dynamics play in catalysis is contentious.[22-24] DHFR is a

ubiquitous enzyme that catalyzes the reduction of the substrate 7,8-dihydrofolate (DHF) to 5,6,7,8-tetrahydrofolate (THF) through the oxidation of the cofactor nicotinamide adenine dinucleotide phosphate (NADPH) to $NADP^+$. The mechanism of substrate reduction involves a hydride transfer from NADPH to DHF, as well as a concomitant proton transfer.[25]

Molecular Dynamics (MD) simulations and mutational studies have indirectly shown that there are motions across the enzyme that are coupled to each other.[26] In DHFR, there is a network of coupled motions that are coupled to catalysis involving active site residue I14 and distal residues M42, G121, and F125.[26-29] Mutations directly on any of these residues changes the motions such that they become catalytically unfavorable, thus halting the activity of the enzyme. Adding energy into proteins excites vibrations, such as local bond vibrations or collective motions of loops. Because these motions are directly coupled to catalysis, it is possible that inputting energy, in the form of heat, close to this network will cause an acceleration in enzyme activity by allowing the protein to access more conformations and thus more reactive ones.

In the present work, we study the effects on enzyme activity due to dynamical protein motions with both continuous wave (CW) and pulsed (nanosecond and femtosecond) laser excitation of DHFR-15 nm AuNP conjugates (**Figure 4.1**). AuNPs were attached to DHFR near the network of coupled motions and distal to the network. Previous studies with different enzymes show that site-directed orientation of the protein, its surface density, and size of the AuNP affect the activity of the enzyme.[30-33] However, there have been no prior studies connecting attachment site of AuNPs with dynamical motions in enzymes, nor investigating the effect of heat transfer from AuNPs when protein

is site-specifically labeled on AuNPs. Here, we are interested in how heat transfer to the enzyme via site-specific locations might affect enzyme motions, as well as the timescale of these motions.

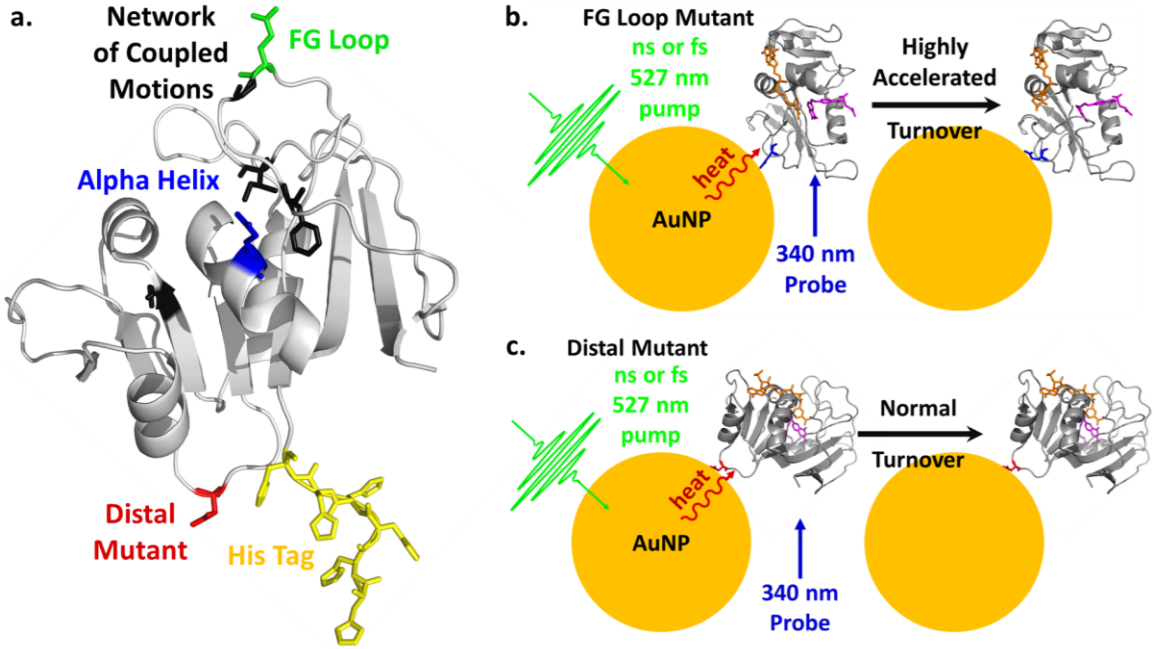

Figure 4.1: Laser Heating Experimental Scheme.

Schematic of the overall experimental design. **a.** DHFR labeled with mutated residues (PDB: 1RX2). Green = FG Loop, blue = Alpha Helix, red = Distal Mutant, and yellow = His Tagged. The residues in the network of coupled motions are black. **b.** FG Loop mutant location. E120, on the FG loop, is mutated to a cysteine for the site of AuNP attachment. This conjugate is expected to have an accelerated turnover because DHFR is attached to the AuNP next to the G121 residue involved in the network of coupled motions in DHFR. **c.** Distal Mutant location. D87 is mutated to a cysteine. There is no expected change in enzyme turnover for this conjugate because the attachment site is not near the network of coupled motions in DHFR. These representations are not to scale. While one enzyme per AuNP is shown here, the experimental evidence shows that there is a monolayer of protein covering each AuNP.[34]

Section 4-2: Results and Discussion

Section 4-2.1: Experimental Design of Dihydrofolate Reductase Mutants

To test the hypothesis that the input of heat energy into the network of coupled motions of DHFR accelerates enzyme turnover, we locally heated the enzyme during turnover through a covalently bound AuNP, either next to the network and active site or remote from it. The AuNP was attached to DHFR by forming a gold-thiol covalent bond with a cysteine (Cys)[35] introduced site-specifically to the surface of the protein as shown in **Figure 4.1a**. The intrinsic Cys, C85 and C152, were mutated to C85A and C152S (ΔCys) to remove them as possible competitive binding sites. The His-tag was also removed from the surface Cys mutants to avoid coordination of AuNPs to both the Cys and His-tag sites. Three positions on the protein were targeted; two that are close to the network of coupled motions and a third that is distal to it, as a control. The FG Loop mutant (E120CΔCys) uses E120C as the AuNP attachment site on the FG loop, immediately adjacent to G121, which is known to be part of the network of coupled motions.[26, 28] Since motions of the FG loop and the nearby network are known to be important for catalysis, attaching the AuNP here should allow for input of heat directly into this flexible region of the enzyme. The second mutant, the Alpha Helix mutant (E101CΔCys), introduces the attachment point on an alpha helix adjacent to the active site, a rigid part of the protein thought to not be involved in the motions of catalysis. Although there is little flexibility or motion of the helix during catalysis, attachment of the AuNP to this location still allows heat transfer close to the active site. There is also a minor network residue nearby, Y100,[26] so some coupling of heat energy into the network may still be possible at this location. The third mutant, the Distal Network mutant (D87CΔCys), has the attachment point on the back side of the protein

opposite the active site and close to the His-tag. E120, E101, and D87 are all equidistant from the active site, but D87 is far away from the network of coupled motions. The final mutant, the His-tag mutant (ΔCys), has no cysteines present in the enzyme, but the presence of the C terminal hexa-histidine tag allows for strong association with the AuNP. This attachment site is on the same side of the protein as D87, also far away from the network, so an input of heat at this attachment site should not affect the activity of the enzyme.

In summary, our hypothesis is that the FG Loop mutant (E120CΔCys) conjugated to AuNPs will have a greater acceleration in turnover in comparison to the Alpha Helix mutant (E101CΔCys)-AuNP conjugates because the AuNP heating the FG loop should have a greater effect on the enzyme motions in catalysis, while no change in activity is expected for either the Distal Network (D87CΔCys) or His Tagged (ΔCys) conjugates (**Figure 4.1**).

Section 4-2.2: Characterization of Enzyme-Gold Nanoparticle Conjugates

We have described the complete characterization of DHFR-AuNP bioconjugates previously.[35] Here, the characterization for the His tagged mutant is compared with the cysteine attached mutants previously described. Briefly, SDS-PAGE and UV/Vis absorbance spectroscopy are used to confirm conjugation of the AuNP to DHFR, and Dynamic Light Scattering (DLS) is used to quantify the surface coverage (protein monolayer versus multilayers). Unstained SDS-PAGE shows that DHFR-AuNP conjugates (15 nm AuNPs) run on the gel and are stable, unlike free AuNPs that aggregate in the wells (**Figure 4.2**).

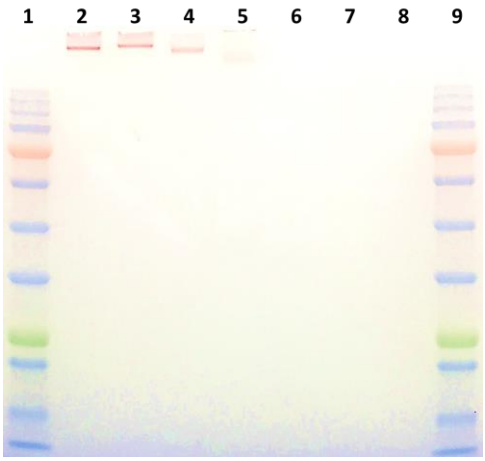

Figure 4.2: Unstained SDS-PAGE Gel of Conjugates.

Lanes 1 and 9 are protein marker. Lanes 2-4 contain DHFR-AuNP conjugates. Lane 5 contains free AuNPs. Lanes 6-8 contain free protein. The DHFR-AuNP conjugates are pink in color, indicating their stability. The gel is unstained, so no sample is visible in the free protein lanes.[34]

Coomassie Blue stained SDS-PAGE shows that protein is bound to the AuNPs, as the pink conjugates are stained blue, and that there is no detectable free protein in the conjugate wells (**Figure 4.3a**). UV/Vis absorbance spectroscopy verified that protein is conjugated on the AuNP surface by showing a redshift in the SPR band from 518 nm to 523 nm (**Figure 4.3b**). This 5 nm redshift is indicative of protein binding to the AuNPs and is consistent among all three of the DHFR-AuNP conjugates. DLS was used to determine the size of the AuNPs and conjugates (**Figure 4.3c**). Unbound AuNPs have a hydrodynamic diameter of 18 nm, compared to 27 nm for the cysteine bound conjugates and 31 nm for the His Tagged conjugates. Subtracting the AuNP hydrodynamic radius from the cysteine bound one gives a thickness of the DHFR layer of 4.5 nm, comparable to the 4 nm diameter of DHFR determined from the crystal structure. Therefore, the DLS measurements are consistent with a monolayer of protein bound to the AuNPs.

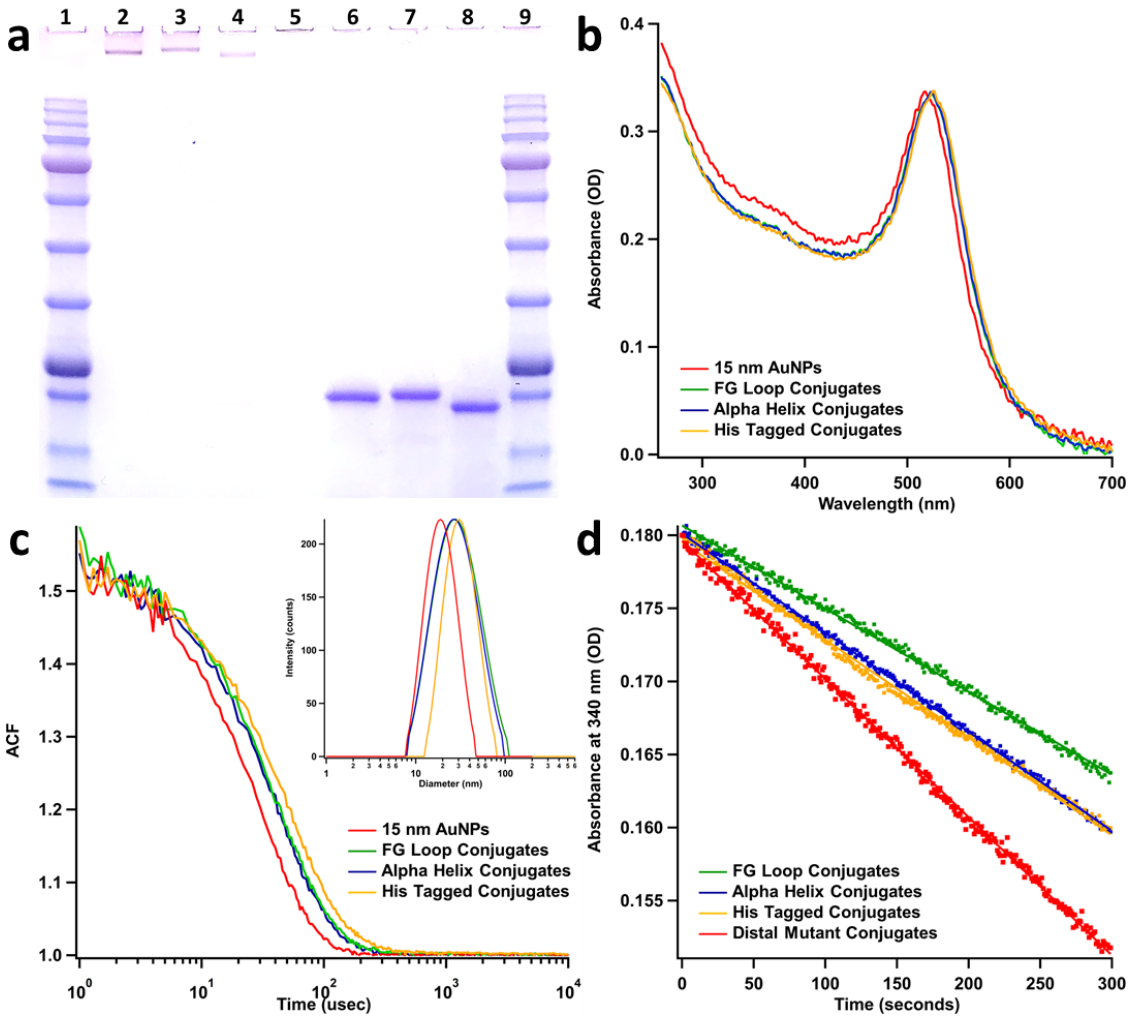

Figure 4.3: Characterization of Conjugates for Laser Heating.

a. Coomassie Blue stained SDS-PAGE gel (Distal Network mutant not shown but runs the same as the cysteine bound conjugates). Lanes 1 and 9 are protein ladders. Lanes 2-4 are conjugates (FG Loop, Alpha Helix, His Tagged). Lane 5 is free 15 nm AuNPs. Lanes 6-9 are free protein, same order as conjugates. The conjugates are purple, indicating blue protein stain on pink conjugates. Free AuNPs aggregate and do not run. There is no free enzyme in the conjugates. **b.** UV/Vis spectra free AuNPs and all conjugates. **c.** DLS of free AuNPs and conjugates. The ACF shows the diffusion rate over time, and the inset shows the intensity distribution. **d.** Concentration corrected activity plots of FG Loop, Alpha Helix, Distal Mutant, and His Tagged conjugates over time.

Free, unbound AuNPs = red, FG Loop mutant conjugates = green, Alpha Helix mutant conjugates = blue, and His Tagged conjugates = yellow. Distal Network mutant not shown for SDS-PAGE, UV/Vis absorption, and DLS, but it runs the same as the cysteine bound conjugates.[34]

The concentration of protein in the DHFR-AuNP conjugates is required to determine the enzyme activity. AuNPs have strong absorbance and scattering in the UV and visible spectral regions, so we used potassium cyanide (KCN) to dissolve the AuNPs and a protein fluorescence assay to determine protein concentration as described in detail previously (**Figure 4.4**).[35] The concentration of protein in the conjugates is consistently in the range of 3-5 μM.

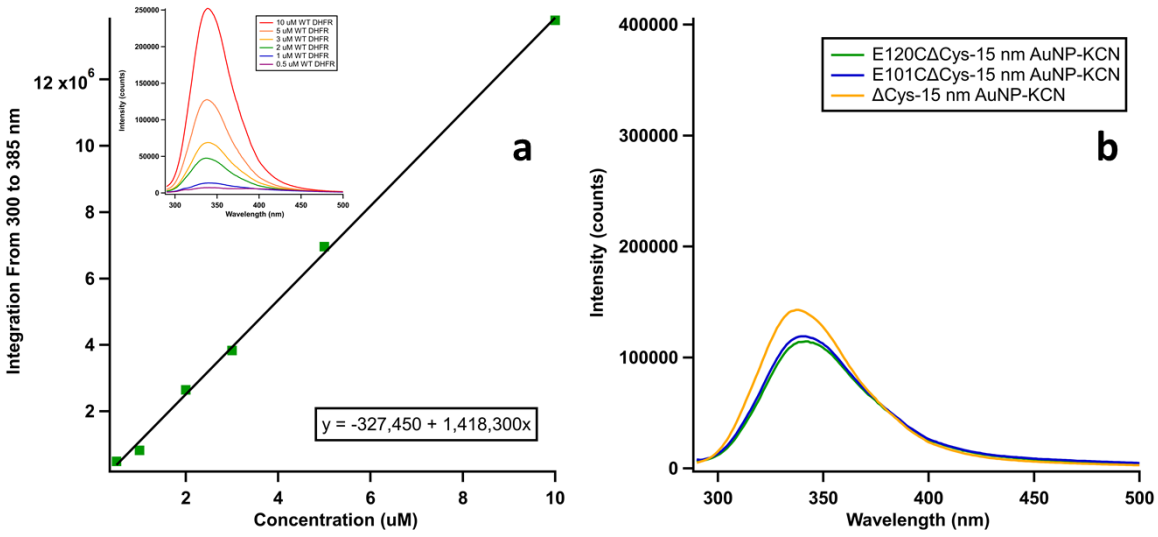

Figure 4.4: Determining Protein Concentration for Laser Heating.

Fluorescence assay for protein concentration determination on the AuNPs. **a.** Standard curve for WT DHFR protein samples treated in the same manner as the unknown conjugate samples (same KCN and Tween 20 concentrations). The inset shows the raw data after 280 nm excitation. The area under each curve from 300 to 385 nm were taken and plotted versus their respective concentrations to form the standard curve. **b.** The raw data for the conjugate samples. The area under the conjugate curves were used in conjunction with the standard curve equation to determine the concentration of protein in the AuNP samples.[34]

To test whether the concentration determined by this assay makes physical sense, we calculated the number of proteins per AuNP and compared this to what would be

expected for a close packed monolayer of protein on the AuNP surface. The concentration of AuNPs was determined from the absorbance spectrum using Beer's Law and $\varepsilon_{523\ nm}$ = 3.67 x 10^8 $M^{-1}cm^{-1}$ for 15 nm AuNPs, from which we calculated the molar ratio of DHFR:AuNP. The average number of proteins per AuNP in the single cysteine conjugates is 35 ± 4, while that ratio is 60 ± 6 for the His-Tag mutant conjugates, indicating consistent with monolayer surface coverage. [35] This difference in DHFR:AuNP ratio for the covalently attached protein versus His-Tag linkage is consistent with the DLS results in **Figure 4.3c**. The cysteine bound conjugates have protein directly bound to the AuNP surface through a gold-thiol covalent bond. In contrast, for the His-tag conjugates, the protein is strongly associated via a hexa His-tag, connected to the C-terminus of the protein through a flexible TEV cleavage sequence (ENLYFQG). This flexible linker likely allows for a higher packing density of DHFR on the AuNP surface and thus a higher surface coverage, consistent with the determined higher protein:AuNP ratio.

Section 4-2.3: Monitoring Activity of DHFR-AuNP Conjugates

The V_{max} of DHFR on the DHFR-AuNP conjugates was measured at saturating substrate concentrations using the 340 nm NADPH absorbance to follow the kinetics. The K_m of DHFR is 4.8 μM[25] and 50 μM of substrate is used in our assays, so V_{max} is certainly being measured in our kinetics experiments. When corrected for concentration, k_{cat} was found, and the Distal Mutant conjugates retain more activity than the other conjugates (**Figure 4.3d and Table 4.1**), which is not surprising, as the cofactor and substrate binding sites of DHFR are more solvent exposed. In the FG Loop and Alpha Helix mutant conjugates, the cofactor binding site may be partially blocked due to the enzyme orientation

on the AuNP, which could explain the lowered activity. The His Tagged conjugates have higher surface coverage based on the fluorescence assay and DLS, which could create protein crowding on the AuNP surface. This could be the cause of the lower activity measurements, as the substrate and cofactor access might be restricted.

Table 4-1: k_{cat} of Free Protein and DHFR-AuNP Conjugates.

Activity measured through steady state turnover, with and without laser illumination.[34]

	k_{cat} (s^{-1})				
Sample Type	**Free Protein**	**-AuNP,[a] No Laser**	**-AuNP,[a] CW**	**-AuNP,[a] ns**	**-AuNP,[a] fs**
FG Loop	27.2 ± 0.3[b]	0.645 ± 0.048	**100 mW:** 0.592 ± 0.028	**50 mW:** 0.568 ± 0.030	**5 mW:** 0.694 ± 0.031
			250 mW: 0.653 ± 0.053	**100 mW:** 1.143 ± 0.032	**20 mW:** 0.690 ± 0.035
				200 mW: 1.105 ± 0.048	**40 mW:** 1.270 ± 0.032
Alpha Helix	30.0 ± 0.3	0.769 ± 0.047	**100 mW:** 0.781 ± 0.023	**50 mW:** 0.750 ± 0.045	**5 mW:** 0.722 ± 0.055
			250 mW: 0.837 ± 0.088	**100 mW:** 1.200 ± 0.048	**20 mW:** 0.745 ± 0.102
				200 mW: 1.221 ± 0.045	**40 mW:** 1.302 ± 0.088
His Tagged	29.6 ± 0.4	0.759 ± 0.035	**100 mW:** 0.742 ± 0.071	**50 mW:** 0.781 ± 0.070	**5 mW:** 0.758 ± 0.038
			250 mW: 0.756 ± 0.041	**100 mW:** 0.792 ± 0.062	**20 mW:** 0.769 ± 0.028
				200 mW: 0.836 ± 0.026	**40 mW:** 0.798 ± 0.037
Distal Mutant	30.1 ± 0.4	1.073 ± 0.083	**100 mW:** 1.004 ± 0.062	**50 mW:** 1.176 ± 0.088	**5 mW:** 1.117 ± 0.057
			250 mW: 1.079 ± 0.053	**100 mW:** 0.981 ± 0.079	**20 mW:** 1.175 ± 0.020
				200 mW: 1.032 ± 0.059	**40 mW:** 1.199 ± 0.010

[a]Conjugates with 15 nm AuNPs. [b]Uncertainties represent standard deviations of at least 3 trials.

Section 4-2.4: Laser Heating of the DHFR-AuNP Conjugates

Our hypothesis is that the input of heat energy into DHFR's network of coupled motions accelerates enzyme turnover, but we also hypothesize that there is a dependence on the timescale of light excitation. The initial energy input is localized at a specific site on the protein surface, but the energy will be redistributed throughout the protein structure on some unknown timescale. Since the net change in temperature is small once the energy is distributed throughout the structure (*vide infra*, COMSOL simulations and Arrhenius kinetics), the effect on rate of continuous heating should be minimal. Therefore, our hypothesis is that for local excitation of the enzyme to affect catalysis, the energy must be input on a timescale that is faster than the redistribution time and can therefore preferentially excite the motions of the protein that are coupled to catalysis. To test this, enzyme-AuNP conjugates were excited with three different types of lasers, all varying in timescale of excitation: 531 nm continuous wave (CW), 527 nm nanosecond (ns) pulsed, and 530 nm femtosecond (fs) pulsed. Each of these lasers is centered around 530 nm, which is used to excite the SPR band of 15 nm AuNPs (**Figure 4.5**).

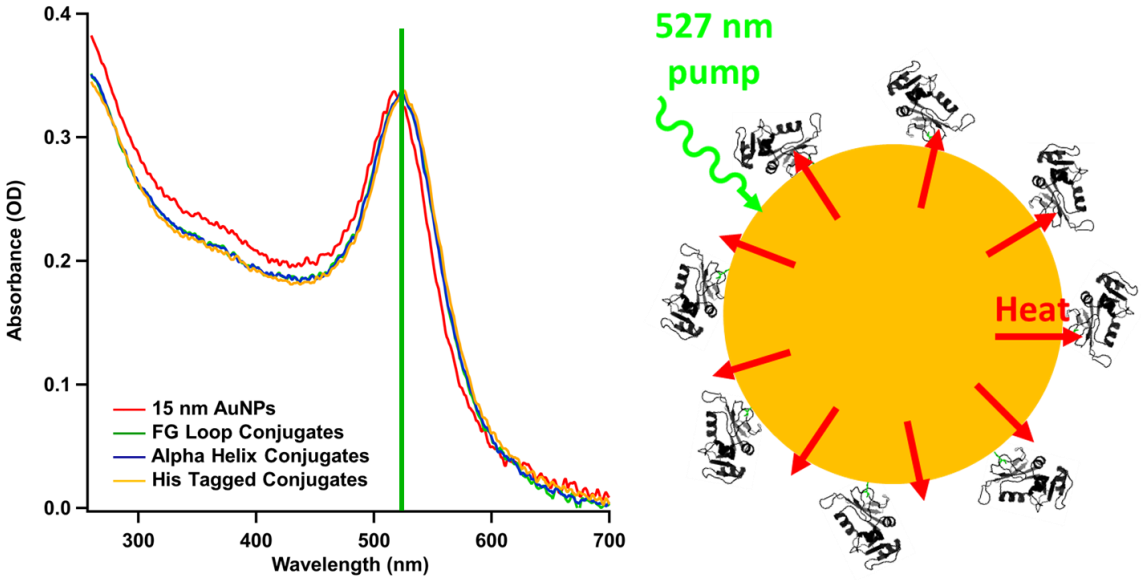

Figure 4.5: Schematic of AuNP Heating.

Each of the three lasers have a wavelength centered at approximately 530 nm, which is at the SPR peak for 15 nm AuNPs conjugated to DHFR. Once the AuNP is excited, the optical energy will be converted to thermal energy that will be dissipated into the surroundings, including into DHFR via the site-specific point of attachment.[34]

Both CW and pulsed lasers deliver the same average power (for example, 50 mW, 100 mW, or 200 mW). The average power is small enough that there is no significant net heating of the protein (much less than 1°C). However, with a pulsed laser, the instantaneous power is much higher than the average power. This high instantaneous power makes it possible to transiently heat the protein, at least locally, before the heat dissipates to yield the same net, small, change in temperature as with the CW laser. We hypothesize that this transient local heating will accelerate the catalysis by activating the coupled network and speeding up the search for reactive conformations. With each of these pump-probe experiments, the pump laser was aligned where the pump and probe beams were

overlapped in the sample such that the probe was only probing the activity of the enzyme that was being excited (locally heated) by the pump beam (**Figure 4.6**).

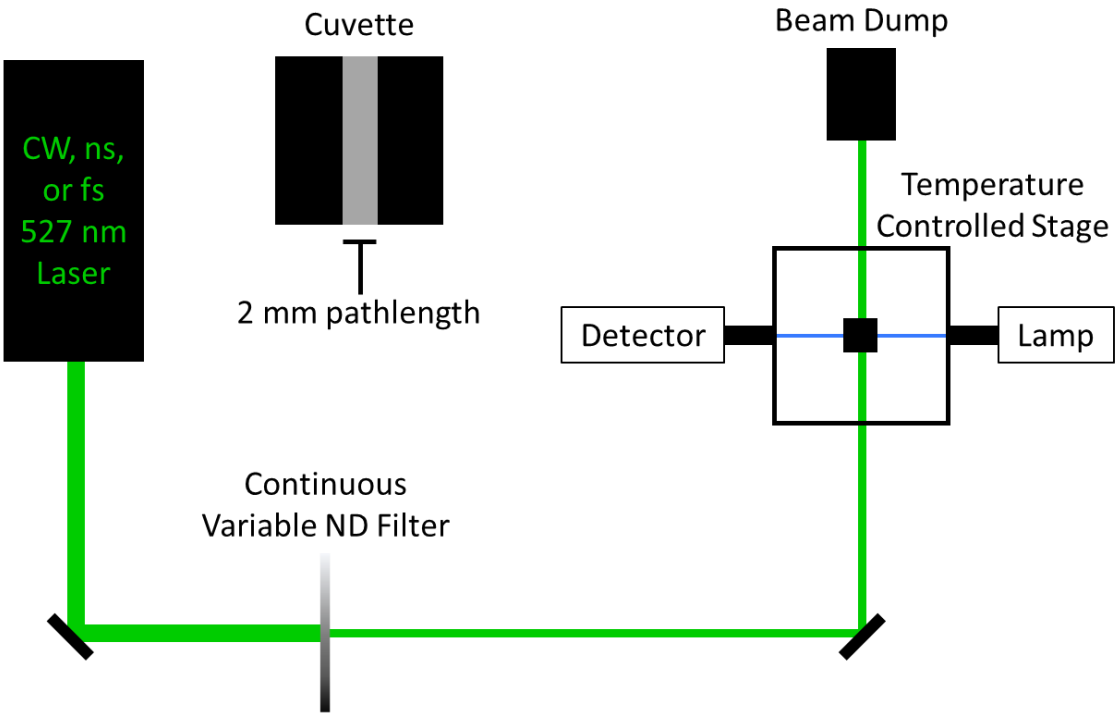

Figure 4.6: Laser Heating Experimental Setup.

Schematic of the system used for the laser heating experiments. The sample in a cuvette is placed in the Peltier temperature-controlled stage. A Xenon lamp probe goes through the 2 mm pathlength orientation of the cuvette. The green CW, 20 ns, or 80 fs laser is sent through a continuous variable neutral density filter to attenuate the power before being sent through the center of the 1 cm pathlength orientation of the cuvette. The laser is terminated with a beam dump or a power meter if measuring the power of the laser.[34]

Section 4-2.5: Pulsed Laser Heating

To examine the effect of pulsed laser excitation on enzyme activity, both 20 ns and 80 fs pulsed lasers were used for excitation sources. The 20 ns excitation source should be similar to the timescale of heat equilibration through the enzyme, and the 80 fs excitation should be shorter than motions or heat equilibration. For the 20 ns laser excitation, pump laser power dependence was performed with 50, 100, and 200 mW average powers. (**Figure 4.7**).

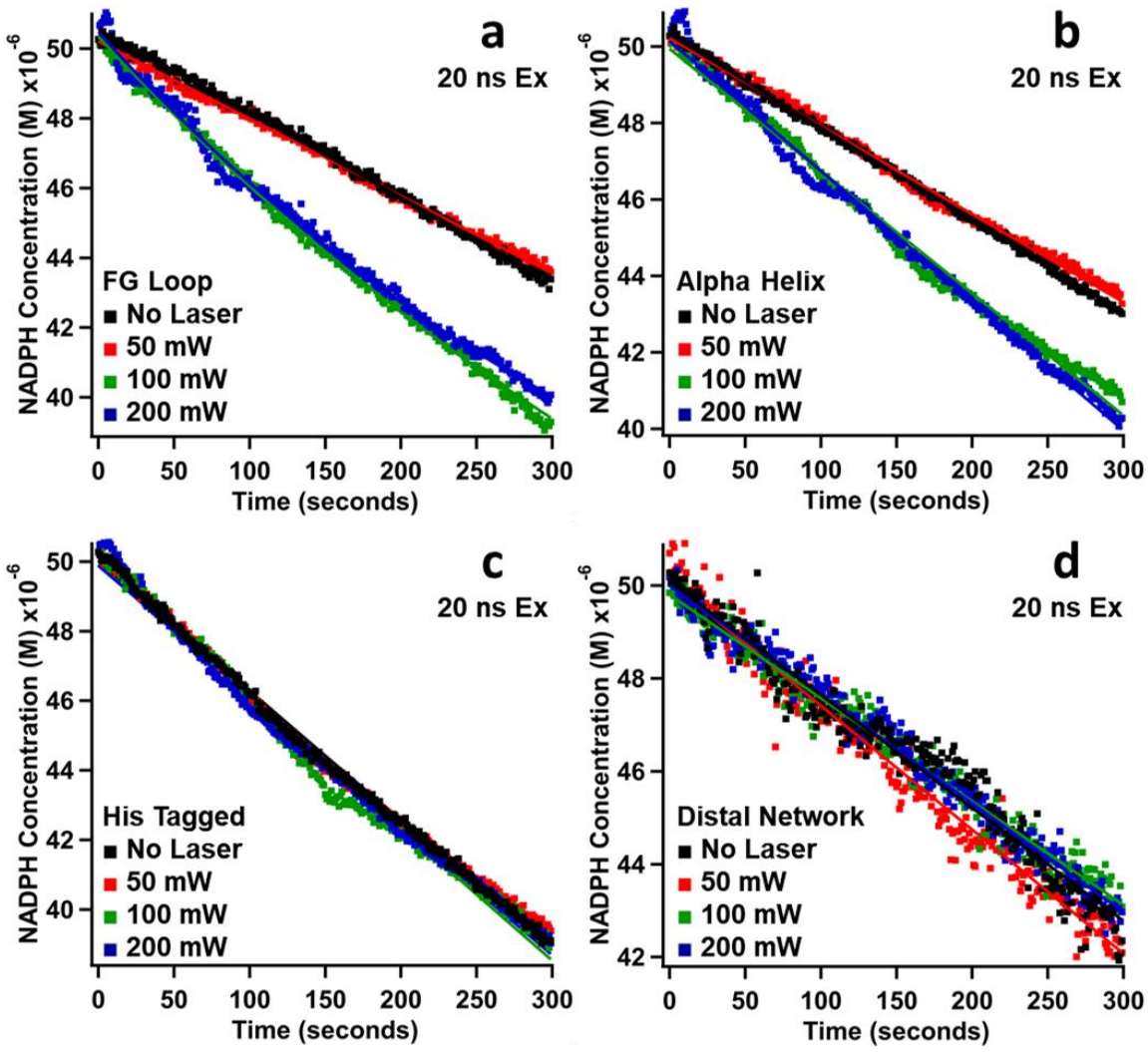

Figure 4.7: Laser Heating with ns Pulsed Excitation.

Rate dependence on nanosecond pulsed laser excitation. **a.** FG Loop-15 nm AuNP conjugates. At least 100 mW ns laser power shows a 75% increase in activity. **b.** Alpha Helix-15 nm AuNP conjugates. At least 100 mW ns laser power shows a 56% increase in activity. **c.** His Tagged-15 nm AuNP conjugates. No increase in activity with any amount of ns laser excitation. **d.** Distal Mutant-15 nm AuNP conjugates. No increase in activity with any amount of ns laser excitation. Reaction conditions for all assays: 10-30 nM enzyme, 50 μM substrate, 50 μM cofactor at 37°C for 5 minutes.[34]

The activity of the FG Loop and Alpha Helix conjugates increased when the AuNP's SPR band was excited with sufficient power, but when they were excited with low

power (50 mW), there was no effect. (**Figure 4.7a-b**). When the power was increased to 100 mW, there was an increase in enzyme activity. The FG Loop conjugate showed a 75% increase in activity, while the Alpha Helix conjugate showed a 56% increase in activity. Increasing the power to 200 mW did not increase this effect, demonstrating that there is a threshold effect of laser power. When the average power was increased above 200 mW, the noise drastically increased, likely due to cavitation caused by the high peak power of individual pulses.[36] Consequently, we kept the average power below 200 mW to avoid this noise problem.

The Distal Mutant and His Tagged conjugates show a different result altogether. When either of these two conjugates are excited with the ns pulsed light, there is no increase in activity with any amount of laser power (**Figure 4.7c-d**). These mutants are both attached to the AuNP away from the networks of motions in DHFR, so the addition of heat is not likely to directly excite any dynamics in the enzyme, which could result in the lack of heating effect.

With the three Cys mutant-AuNP conjugates, the net heat transfer into the protein is the same regardless of the attachment point, as the heat is being transferred from the AuNP to the protein via a Cys residue. Therefore, the efficiency of heat transfer into the protein should be the same between all of the Cys mutant-AuNP conjugates. The unknown questions are: Where does the heat end up after the transfer to the enzyme, and how fast does the heat dissipate throughout the entire enzyme? The results observed here indicate that a maximum effect on the catalysis is achieved when the heat is input more directly into the network of coupled motions in DHFR.

Pump laser power dependence was performed with 5, 20, and 40 mW of 80 fs laser power (**Figure 4.8**). The trend seen with the fs excitation is exactly the same as the trend seen with the ns excitation. For the FG Loop and Alpha Helix conjugates, there is an increase in activity with a sufficient power of the 80 fs pulsed laser (**Figure 4.8)**. When excited with 5 mW and 20 mW of fs pulsed light, there is no change in activity. With 40 mW pump power, the FG Loop conjugates show a 95% increase in activity, and the Alpha Helix conjugates show a 75% increase in activity. The effects of pulsed heating are greater with fs excitation than for ns excitation, indicating that inputting heat on a faster timescale excites more vibrations and could indicate that the important catalytic motions are on the timescale of 20 ns to 80 fs.

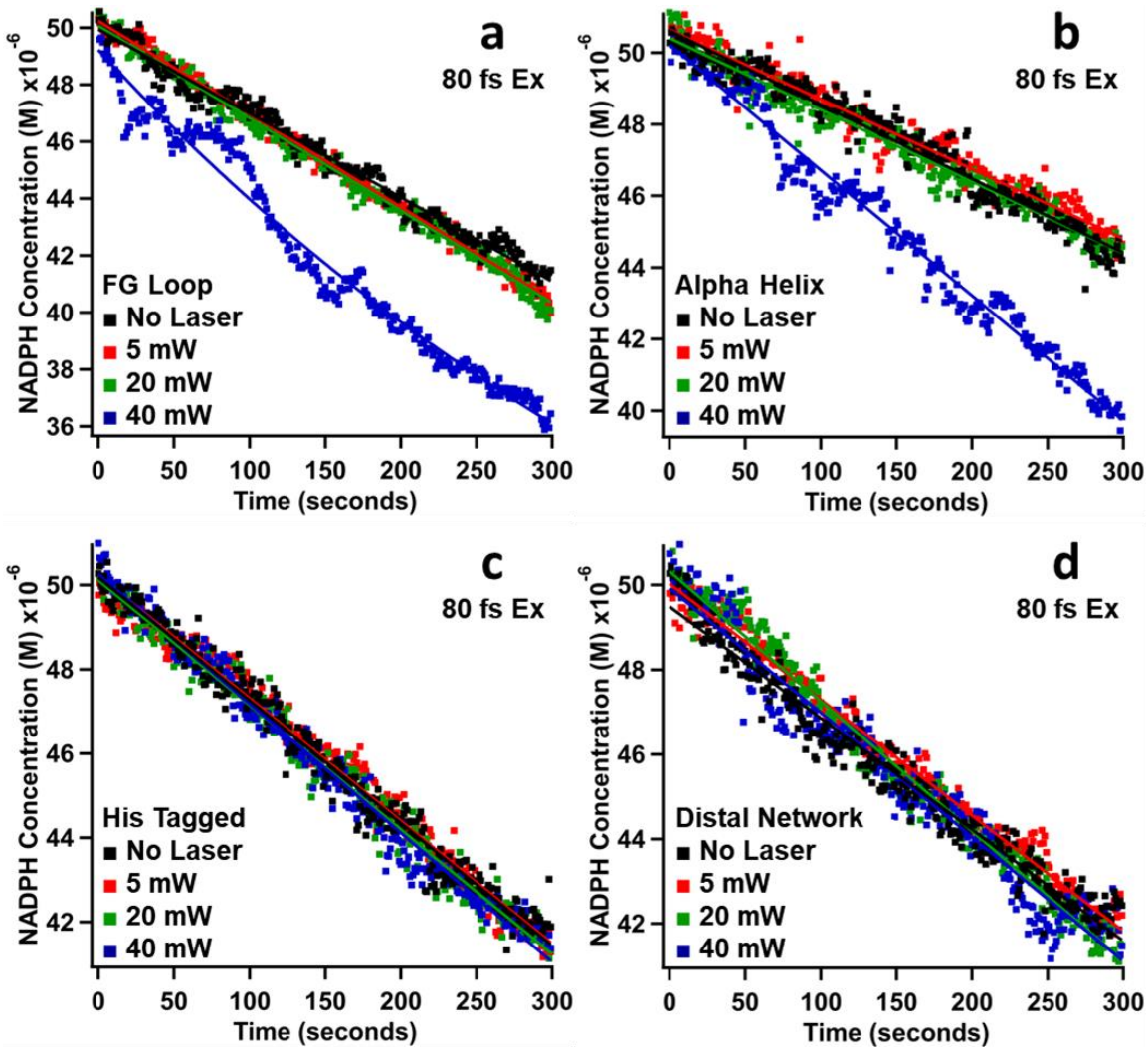

Figure 4.8: Laser Heating with fs Pulsed Excitation.

Rate dependence on femtosecond pulsed laser excitation. **a.** FG Loop-15 nm AuNP conjugates. At least 40 mW fs laser power shows a 95% increase in activity. **b.** Alpha Helix-15 nm AuNP conjugates. At least 40 mW fs laser power shows a 75% increase in activity. **c.** His Tagged-15 nm AuNP conjugates. No increase in activity with any amount of fs laser excitation. **d.** Distal Mutant-15 nm AuNP conjugates. No increase in activity with any amount of fs laser excitation. Reaction conditions for all assays: 10-30 nM enzyme, 50 μM substrate, 50 μM cofactor at 37°C for 5 minutes.[34]

As with the ns pulsed excitation, the Distal Mutant and His Tagged conjugates do not show a turnover increase with any amount of laser excitation (**Figure 4.8c-d**). This is

further evidence that addition of heat on the network of coupled motions in DHFR is imperative to see the rate acceleration, while addition of heat away from the network does not affect the enzyme's turnover.

The Distal Mutant and His Tagged mutant are also experimental controls for questions regarding the bulk heating of solution. If substantial bulk heating were occurring, these two sets of conjugates would also increase in activity with laser excitation. Therefore, the laser excitation in this experiment is directly heating the enzyme from its attachment point to the AuNP, not from bulk heating of the surrounding solution. This idea will be further discussed with temperature-dependent kinetics and calculations later in Chapter 5.

Section 4-2.6: Continuous Wave Laser Heating

As a control, a CW laser was used as a pump excitation source, which provides a continuous excitation of light, not pulsed. Pump power dependence was performed with 100 mW and 250 mW -531 nm CW light. Powers greater than 250 mW were avoided due to the increase in noise. There was no difference in heating the DHFR-AuNP conjugates with any amount of CW excitation (**Figure 4.9**). All of the turnover rates are expressed quantitatively in **Table 4.1**. None of the mutants showed a change in activity with the addition of the CW laser during activity assays. Therefore, continuously heating the DHFR-AuNP conjugates does not affect the enzyme motions related to catalysis. Additionally, the temperature change when continuously heating the conjugates with CW light is negligible, as there was no activity change with the continuous excitation.

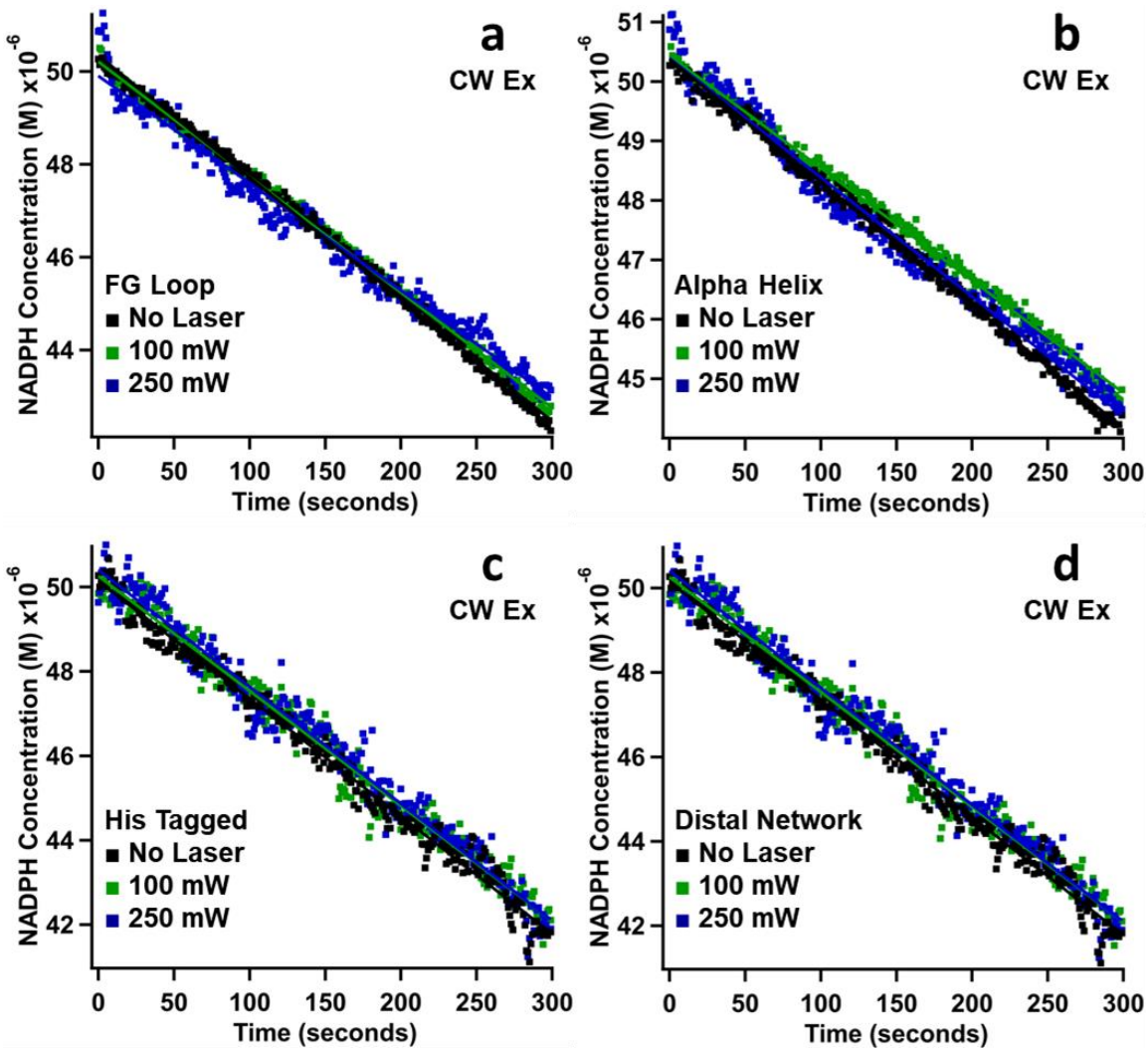

Figure 4.9: Laser Heating with CW Excitation.

Rate dependence on CW laser excitation. **a.** FG Loop-15 nm AuNP conjugates. **b.** Alpha Helix-15 nm AuNP conjugates. **c.** His Tagged-15 nm AuNP conjugates. **d.** Distal Mutant-15 nm AuNP conjugates. None of the conjugates show any increase in activity with any power of a CW laser. Reaction conditions for all assays: 10-30 nM enzyme, 50 μM substrate, 50 μM cofactor at 37°C for 5 minutes.[34]

Section 4-2.7: Comparing Activity with and without Laser

To ensure that the laser excitation was the source of the rate acceleration, a comparison of activity with and without laser excitation was performed on the same

sample. A normal activity assay was run on FG Loop-AuNP conjugates, where there was no laser excitation at the start of the assay. Standard assays are five minutes in length, so at 2.5 minutes, the shutter was opened, and the laser was allowed to interact with the sample (**Figure 4.10**). For the first 2.5 minutes, there is a linear decrease in absorbance. After 2.5 minutes, upon allowing the laser excitation into the sample, there is a drastic increase in slope until the end of the five-minute assay. This demonstrates that the acceleration in rate only occurs when the laser excitation is actively heating the sample.

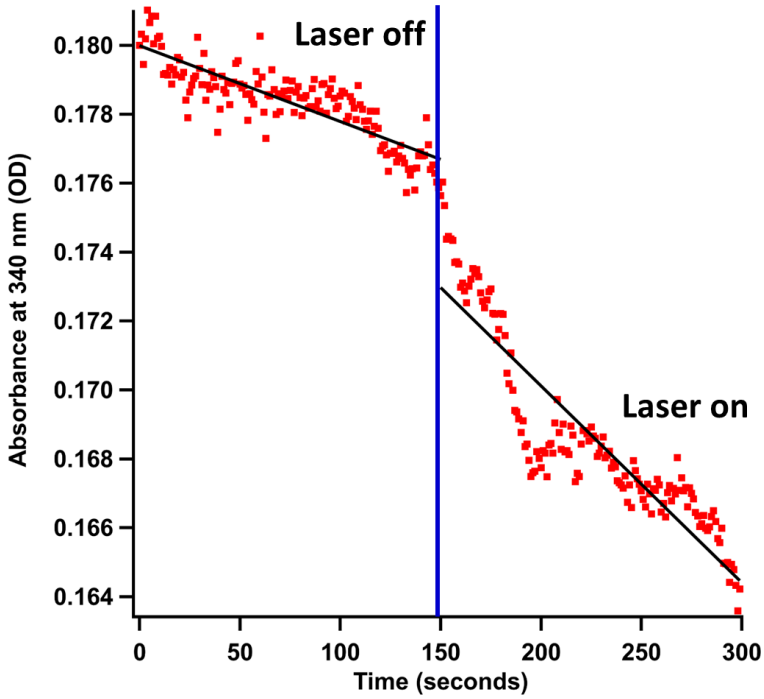

Figure 4.10: DHFR-AuNP Activity: Laser Off vs. Laser On.

Activity of FG Loop-15 nm AuNP conjugates with addition of laser halfway through measurement. The turnover was measured with no laser for 150 seconds, then the laser was opened to excite the same sample for the last 150 seconds. There is a clear difference in the "laser off" slope versus the "laser on" slope, with a drastic increase in slope once the laser hits the sample.[34]

Section 4-3: Chapter 4 Conclusions

In summary, we explored the role of dynamical motions in DHFR catalysis through site-directed heating via attached AuNPs. AuNPs are biologically compatible heaters that allow a large amount of energy to be put into the protein site-specifically. The energy of a single 527 nm photon is 227 kJ/mol, and the activation barrier of DHFR is approximately 75 kJ/mol based on our Arrhenius analysis, so there is a lot of energy being put into the protein from the AuNP. While a lot of the energy from the AuNP gets dissipated, it appears that the enzyme has a way of coupling some of that energy to the active site, specifically through the network of coupled motions. The key is that the energy needs to be input into the network and on the appropriate timescale, such that the coupling outcompetes the energy dissipation. When we excited with 20 ns and 80 fs laser pulses, there was a high rate of acceleration for the FG Loop-AuNP conjugates, where the AuNP was attached directly on the network of coupled motions. We observed no turnover change with either the Distal Mutant-AuNP and His Tagged-AuNP conjugates, which were away from the network. Further, we also observed no change in turnover with any of the DHFR-AuNP conjugates when excited with a CW laser. There was a higher extent of acceleration with the 80 fs pulses than with the 20 ns pulses, which agrees with the previous literature regarding energy dissipation in both proteins and AuNPs.[37-42] This signifies that the important motions in catalysis of DHFR occur on a timescale faster than 20 ns but slower than 80 fs.

Section 4-4: Chapter 4 References

1. Hammes-Schiffer, S.; Benkovic, S. J., Relating protein motion to catalysis. *Annu. Rev. Biochem.* **2006,** *75*, 519-541.

2. Olsson, M. H. M.; Parson, W. W.; Warshel, A., Dynamical contributions to enzyme catalysis: Critical tests of a popular hypothesis. *Chem. Rev.* **2006,** *106* (5), 1737-1756.

3. Glowacki, D. R.; Harvey, J. N.; Mulholland, A. J., Taking Ockham's razor to enzyme dynamics and catalysis. *Nat. Chem.* **2012,** *4* (3), 169-176.

4. Callender, R.; Dyer, R. B., The Dynamical Nature of Enzymatic Catalysis. *Acc. Chem. Res.* **2015,** *48* (2), 407-413.

5. Luk, L. Y. P.; Loveridge, E. J.; Allemann, R. K., Protein motions and dynamic effects in enzyme catalysis. *Phys. Chem. Chem. Phys.* **2015,** *17*, 30817-30827.

6. Singh, P.; Abeysinghe, T.; Kohen, A., Linking Protein Motion to Enzyme Catalysis. *Molecules* **2015,** *20* (1), 1192-1209.

7. Richard, J. P., Protein Flexibility and Stiffness Enable Efficient Enzymatic Catalysis. *J. Am. Chem. Soc.* **2019,** *141* (8), 3320-3331.

8. Klinman, J. P.; Kohen, A., Hydrogen tunneling links protein dynamics to enzyme catalysis. *Annu. Rev. Biochem.* **2013,** *82*, 471-496.

9. Benkovic, S. J.; Hammes, G. G.; Hammes-Schiffer, S., Free-energy landscape of enzyme catalysis. *Biochemistry* **2008,** *47* (11), 3317-3321.

10. Allemann, R. K.; Evans, R. M.; Loveridge, E. J., Probing coupled motions in enzymatic hydrogen tunnelling reactions. *Biochem. Soc. Trans.* **2009,** *37*, 349-353.

11. Radkiewicz, J. L.; Brooks III, C. L., Protein Dynamics in Enzymatic Catalysis: Exploration of Dihydrofolate Reductase. *J. Am. Chem. Soc.* **2000,** *122*, 225-231.

12. Nagel, Z. D.; Klinman, J. P., Tunneling and dynamics in enzymatic hydride transfer. *Chem. Rev.* **2006,** *106* (8), 3095-3118.

13. Wang, L.; Goodey, N. M.; Benkovic, S. J.; Kohen, A., The role of enzyme dynamics and tunnelling in catalysing hydride transfer: studies of distal mutants of dihydrofolate reductase. *Philos T Roy Soc B* **2006,** *361* (1472), 1307-1315.

14. Blankschien, M. D.; Pretzer, L. A.; Huschka, R.; Halas, N. J.; Gonzalez, R.; Wong, M. S., Light-Triggered Biocatalysis Using Thermophilic Enzyme-Gold Nanoparticle Complexes. *ACS Nano* **2013,** *7* (1), 654-663.

15. Schade, M.; Moretto, A.; Donaldson, P. M.; Toniolo, C.; Hamm, P., Vibrational Energy Transport through a Capping Layer of Appropriately Designed Peptide Helices over Gold Nanoparticles. *Nano Lett.* **2010,** *10* (8), 3057-3061.

16. Hassan, S.; Schade, M.; Shaw, C. P.; Lévy, R.; Hamm, P., Response of Villin Headpiece-Capped Gold Nanoparticles to Ultrafast Laser Heating. *J. Phys. Chem. B* **2014,** *118* (28), 7954-7962.

17. Adleman, J. R.; Boyd, D. A.; Goodwin, D. G.; Psaltis, D., Heterogeneous Catalysis Mediated by Plasmon Heating. *Nano Lett.* **2009,** *9* (12), 4417-4423.

18. Govorov, A. O.; Richardson, H. H., Generating heat with metal nanoparticles. *Nano Today* **2007,** *2* (1), 30-38.

19. Sapsford, K. E.; Algar, W. R.; Berti, L.; Gemmill, K. B.; Casey, B. J.; Oh, E.; Stewart, M. H.; Medintz, I. L., Functionalizing Nanoparticles with Biological Molecules: Developing Chemistries that Facilitate Nanotechnology. *Chem. Rev.* **2013,** *113* (3), 1904-2074.

20. Maity, S.; Downen, L. N.; Bochinski, J. R.; Clarke, L. I., Embedded metal nanoparticles as localized heat sources: An alternative processing approach for complex polymeric materials. *Poly* **2011,** *52* (7), 1674-1685.

21. Webb, J. A.; Bardhan, R., Emerging advances in nanomedicine with engineered gold nanostructures. *Nanoscale* **2014,** *6* (5), 2502-2530.

22. Bhabha, G.; Lee, J.; Ekiert, D. C.; Gam, J.; Wilson, I. A.; Dyson, H. J.; Benkovic, S. J.; Wright, P. E., A dynamic knockout reveals that conformational fluctuations influence the chemical step of enzyme catalysis. *Science* **2011,** *332* (6026), 234-238.

23. Loveridge, E. J.; Behiry, E. M.; Guo, J.; Allemann, R. K., Evidence that a dynamic knockout' in Escherichia coli dihydrofolate reductase does not affect the chemical step of catalysis. *Nat. Chem.* **2012,** *4* (4), 292-297.

24. Adamczyk, A. J.; Cao, J.; Kamerlin, S. C. L.; Warshel, A., Catalysis by dihydrofolate reductase and other enzymes arises from electrostatic preorganization, not conformational motions. *Proc. Natl. Acad. Sci. U.S.A.* **2011,** *108* (34), 14115-14120, S14115/1-S14115/8.

25. Fierke, C. A.; Johnson, K. A.; Benkovic, S. J., Construction and evaluation of the kinetic scheme associated with dihydrofolate reductase from Escherichia coli. *Biochemistry* **1987,** *26* (13), 4085-92.

26. Agarwal, P. K.; Billeter, S. R.; Rajagopalan, P. T. R.; Benkovic, S. J.; Hammes-Schiffer, S., Network of Coupled Promoting Motions in Enzyme Catalysis. *Proc. Natl. Acad. Sci. U.S.A.* **2002,** *99*, 2794-2799.

27. Singh, P.; Francis, K.; Kohen, A., Network of Remote and Local Protein Dynamics in Dihydrofolate Reductase Catalysis. *ACS Catal.* **2015,** *5* (5), 3067-3073.

28. Singh, P.; Sen, A.; Francis, K.; Kohen, A., Extension and Limits of the Network of Coupled Motions Correlated to Hydride Transfer in Dihydrofolate Reductase. *JACS* **2014,** *136* (6), 2575-2582.

29. Agarwal, P. K., Role of Protein Dynamics in Reaction Rate Enhancement by Enzymes. *J. Am. Chem. Soc.* **2005,** *127* (43), 15248-15256.

30. Liu, F.; Wang, L.; Wang, H.; Yuan, L.; Li, J.; Brash, J. L.; Chen, H., Modulating the Activity of Protein Conjugated to Gold Nanoparticles by Site-Directed Orientation and Surface Density of Bound Protein. *ACS Applied Materials & Interfaces* **2015,** *7* (6), 3717-3724.

31. Shen, L.; Schroeder, M.; Ogorzalek, T. L.; Yang, P.; Wu, F.-G.; Marsh, E. N. G.; Chen, Z., Surface Orientation Control of Site-Specifically Immobilized Nitro-reductase (NfsB). *Langmuir* **2014,** *30* (20), 5930-5938.

32. Lata, J. P.; Gao, L.; Mukai, C.; Cohen, R.; Nelson, J. L.; Anguish, L.; Coonrod, S.; Travis, A. J., Effects of Nanoparticle Size on Multilayer Formation and Kinetics of Tethered Enzymes. *Bioconjugate Chem.* **2015,** *26* (9), 1931-1938.

33. Vilanova, O.; Mittag, J. J.; Kelly, P. M.; Milani, S.; Dawson, K. A.; Rädler, J. O.; Franzese, G., Understanding the Kinetics of Protein–Nanoparticle Corona Formation. *ACS Nano* **2016,** *10* (12), 10842-10850.

34. Kozlowski, R., Driving Enzyme Dynamics with Light in Dihydrofolate Reductase-Gold Nanoparticle Conjugates. *Nat. Chem.* **to be submitted in 2020**.

35. Kozlowski, R.; Ragupathi, A.; Dyer, R. B., Characterizing the Surface Coverage of Protein–Gold Nanoparticle Bioconjugates. *Bioconjug. Chem.* **2018,** *29* (8), 2691-2700.

36. Wray, W. O.; Aida, T.; Dyer, R. B., Photoacoustic cavitation and heat transfer effects in the laser-induced temperature jump in water. *Appl. Phys. B* **2002,** *74* (1), 57-66.

37. Hill, J. R.; Dlott, D. D.; Rella, C. W.; Peterson, K. A.; Decatur, S. M.; Boxer, S. G.; Fayer, M. D., Vibrational Dynamics of Carbon Monoxide at the Active Sites of Mutant Heme Proteins. *J. Phys. Chem.* **1996,** *100* (29), 12100-12107.

38. Fujisaki, H.; Straub, J. E., Vibrational energy relaxation in proteins. *Proc. Natl. Acad. Sci. U.S.A.* **2005,** *102* (19), 6726-6731.

39. Leitner, D. M., Energy flow in proteins. *Annu. Rev. Phys. Chem.* **2008,** *59*, 233-59.

40. Xie, A.; Meer, A. F. G. v. d.; Austin, R. H., Excited-State Lifetimes of Far-Infrared Collective Modes in Proteins. *Phys. Rev. Lett.* **2001,** *88* (1), 018102.

41. Hu, M.; Hartland, G. V., Heat Dissipation for Au Particles in Aqueous Solution: Relaxation Time versus Size. *J. Phys. Chem. B* **2002,** *106* (28), 7029-7033.

42. Zhang, H.; Sun, Q.; Li, Z.; Nanbu, S.; Smith, S. S., First principle study of proton transfer in the green fluorescent protein (GFP): Ab initio PES in a cluster model. *Comput Theor Chem* **2012,** *990* (Supplement C), 185-193.

Chapter 5 – Exploration of Heating Effect

Section 5-1: Introduction

The results of Chapter 4 show that there is a clear increase in enzymatic turnover with excitation using pulsed lasers. When exciting with 20 ns laser pulses, there was a 75% rate acceleration for the FG Loop-AuNP conjugates, where the AuNP was attached directly on the network of coupled motions. There was a smaller acceleration rate of 56% with the Alpha Helix-AuNP conjugates, where the enzyme was attached near the network residue by the cofactor. There was no change in activity observed with either the Distal Mutant-AuNP and His Tagged-AuNP conjugates. A similar but more pronounced trend was observed with the 80 fs laser excitation, where the FG Loop-AuNP and Alpha Helix-AuNP conjugates both showed an increased turnover acceleration (95% and 75%, respectively), while there was still no change in activity with the Distal Network-AuNP and His Tagged-AuNP conjugates. This demonstrates that the length of the pulse matters, as there was a higher extent of acceleration with the 80 fs pulses than with the 20 ns pulses, which agrees with the previous literature regarding energy dissipation in both proteins and AuNPs.[1-6] This signifies that the important motions in catalysis of DHFR occur on a timescale faster than 20 ns but slower than 80 fs.

The first control performed was to use an excitation source that was not pulsed – A continuous wave (CW) laser source. There was no change in activity observed with any of the DHFR-AuNP conjugates when excited with a CW laser, indicating that our hypothesis that the light must be pulsed was correct. However, more controls are necessary to prove

that the rate acceleration is completely due to dynamics in the enzyme. First, a big question remains: Could the rate acceleration be due to bulk heating of the solution? It is well known that enzymes are generally temperature-dependent, and DHFR activity specifically is dependent on temperature.[7-11] It is also well known that on a very short timescale, AuNPs heat up to extreme temperatures after pulsed laser excitation.[12-14] Here, we can combine experimental and computational techniques to determine the temperature change of the AuNP surface and surrounding solution on the timescale of enzyme turnover. Further, there is a possibility that the pulsed laser excitation has such a high peak pulse power that the enzyme might be dissociating from the surface or the AuNPs might be getting destroyed, causing enzyme dissociation. Transmission electron microscopy (TEM) is used to image electron-rich samples, ie. AuNPs, which can be used to determine the shape and size of AuNPs before and after pulsed laser excitation. Stains can be applied to samples to visualize the presence or absence of protein on electron-rich particles, so TEM can be used to determine if protein is on the AuNP surface or dissociated.

Taken together, these types of controls can ensure that the rate acceleration observed in Chapter 4 is due to enzyme dynamics and not some external factor.

Section 5-2: Results and Discussion

Section 5-2.1: COMSOL Simulations

COMSOL simulations were performed to determine how much of a temperature increase could be expected for the DHFR-AuNP conjugates in the 20 ns and 80 fs pulsed laser heating experiments (**Figure 5.1**).

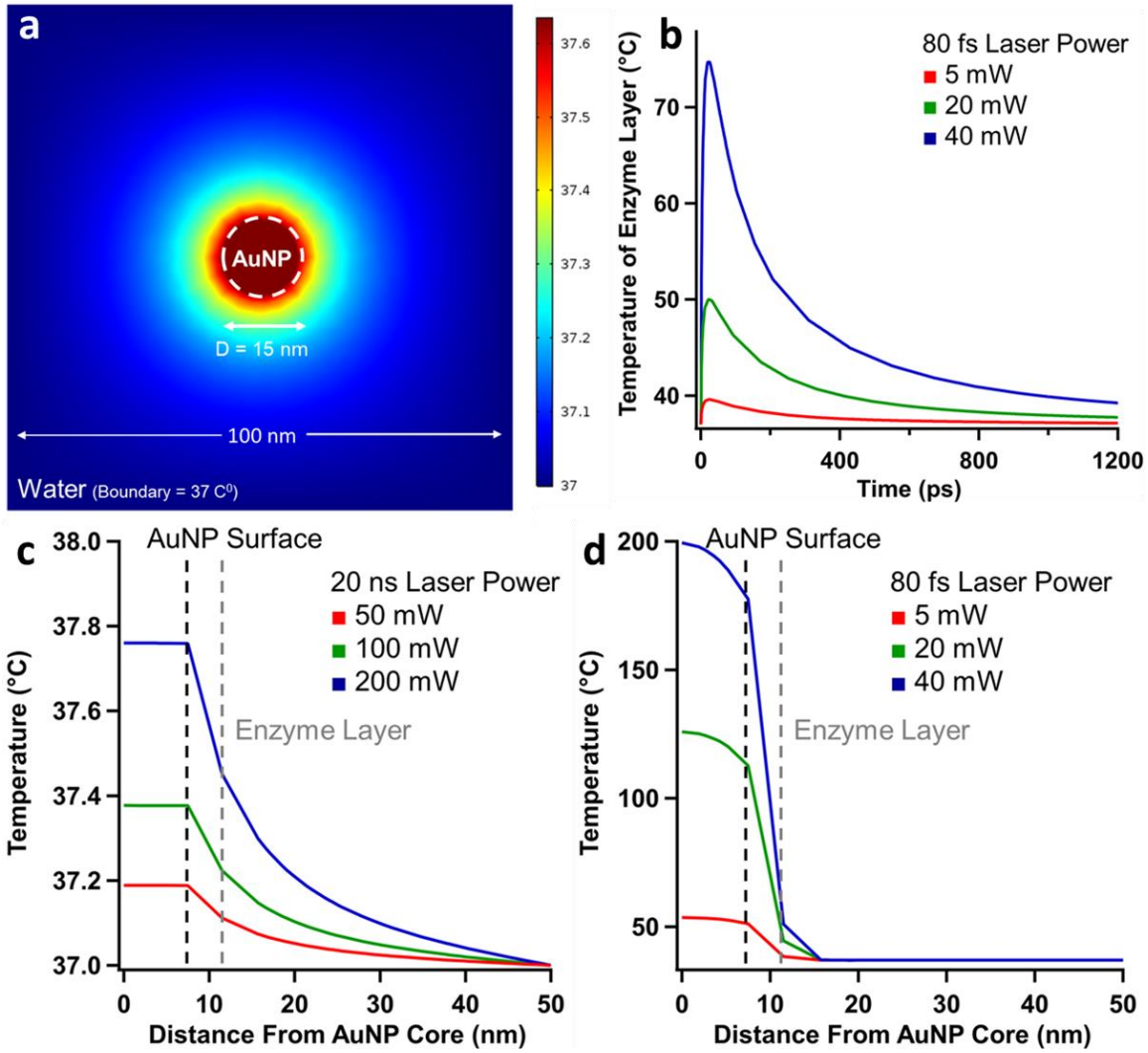

Figure 5.1: COMSOL Simulations of AuNP Heating.

COMSOL finite element analysis. **a.** The heating profile of the 15 nm AuNP and surrounding solution after excitation of a 20 ns laser pulse. Red is warmer temperatures, while blue is cooler temperatures. **b.** Time dependence of the temperature increase at the AuNP surface after 80 fs laser excitation; the large initial increase is dissipated by about 1 ns. **c.** The temperature change in **a** plotted versus the distance from the center of the AuNP for 50 mW, 100 mW, and 200 mW laser powers. For all three powers, the temperature profile is uniform throughout the AuNP itself, then once the on the AuNP surface, there is a nonlinear decrease in temperature until equilibrated with the bulk solution temperature of 37°C, roughly 42.5 nm from the AuNP surface. Same as **c**, but for the fs laser pulse in **Figure 5.2**: 5, 20, and 40 mW.[15]

These simulations were performed using 3-dimensional heat transfer equations to calculate the heat dissipation and the temperature gradient in the surrounding environment (details of the simulation are provided in Section 2-7.3). Initially, there is a large increase in temperature of the AuNP core and AuNP surface, which is very short lived (**Figure 5.1b** and **Figure 5.2**). This heat is transferred to the protein locally, at the point of attachment, heating this local region of the enzyme. At longer times the energy is dissipated over a larger volume, including the full protein structure and the surrounding solution, such that the net change in temperature is quite small (**Figure 5.1c-d**), especially for ns excitation. Therefore, a critical feature of the pulsed laser excitation is the substantial transient heating that occurs in a small region of the protein structure. The initial rise and decay of the transient heating are much faster than the actual turnover rate of the enzyme, but if they occur on the timescale of protein motions coupled to catalysis, they can still affect the net turnover rate.

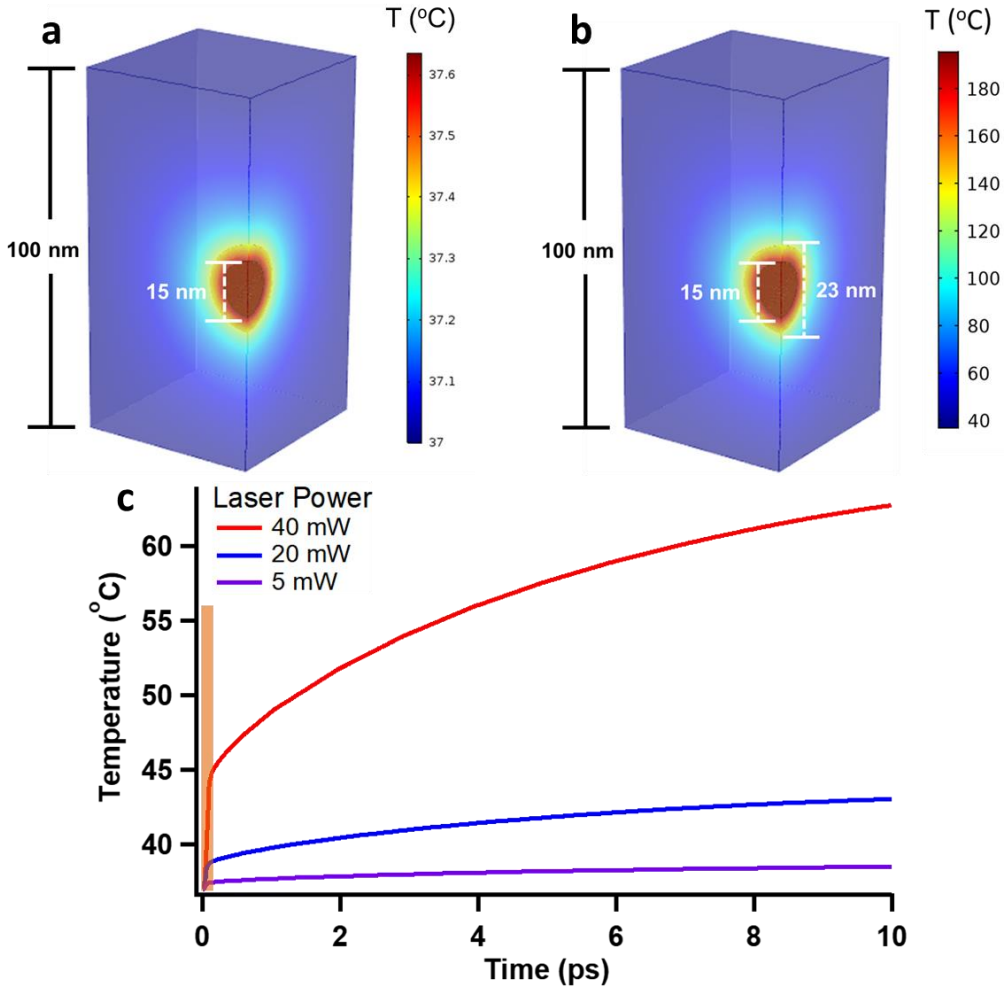

Figure 5.2: COMSOL Modeling Images.

COMSOL model. **a.** Model for 20 ns laser excitation. **b.** Model for 80 fs laser excitation. **c.** Early time profile for fs laser excitation upon 15 nm AuNP. The orange shaded box is the laser pulse duration. The longer timescale can be seen in **Figure 5.1**.[15]

The temperature on the immediate surface of the AuNP increases by 0.4°C for 100 mW of 20 ns pulsed laser power, and even at the highest laser power performed of 200 mW, the temperature increase is only 0.8°C. The enzyme layer is approximately 4 nm in thickness, so for 100 mW power, the temperature gradient across the enzyme would be roughly 37.4°C to 37.25°C compared to the surrounding temperature of 37.0°C. This

makes physical sense because the laser pulses are 20 ns, the dissipation of heat from the AuNP occurs on the order of hundreds of ps, and the repetition rate of the pulses is 5 kHz (one pulse every 200 μs). All of the heat from a single pulse has dissipated well before the next pulse arrives.

There is a much higher initial jump in temperature with the 80 fs excitation, as expected (**Figure 5.1d**). With 40 mW of laser power, the temperature at the AuNP core is roughly 200°C. The heat dissipates as it transfers through the surroundings, reaching the bulk solution temperature of 37°C about 15 nm away from the AuNP core. All of the heat in the 4 nm enzyme layer dissipates within 2 ns after the initial fs pulse (**Figure 5.1b**). The laser pulse duration is 80 fs, and the repetition rate is 1 kHz, or one pulse every millisecond. While the peak pulse power is very high in an 80 fs pulse, the 1 kHz pulse rate allows for complete cooling before the next pulse arrives, meaning that there is no cumulative heating over the course of the experiment.

Section 5-2.2: Temperature Dependent Kinetics of DHFR-AuNP Conjugates

To see the rate changes that would need to be observed in the COMSOL simulations, temperature-dependent kinetics and an Arrhenius analysis were used to characterize the effects of bulk heating on the enzyme activity. The temperature dependence of DHFR kinetics on the bulk temperature of the solution is typical of an activated process. The standard activity assays were run at different temperatures, 22°C, 27°C, 32°C, 37°C, 42°C, and 47°C, and the kinetics data were fit to linear or exponential curves (**Figures 5.3**). This Arrhenius relationship was investigated with each of the free protein mutants and their respective conjugates (**Figure 5.4 and Figure 5.5**).

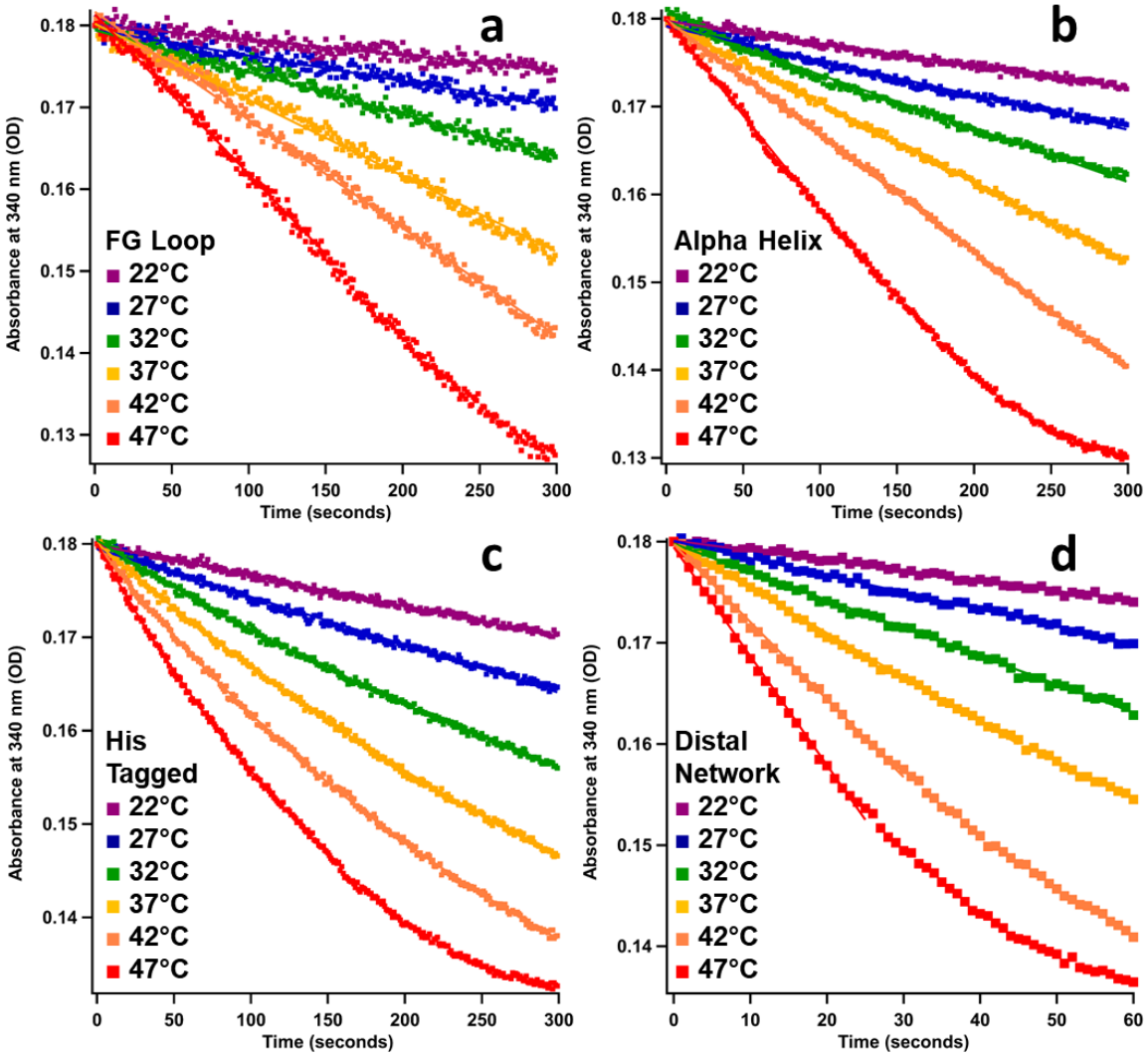

Figure 5.3: Temperature-Dependent Traces for DHFR-AuNP Conjugates.

Individual temperature Arrhenius traces. Each trace is an average of 3 measurements. **a.** FG Loop-15 nm AuNP conjugates. **b.** Alpha Helix-15 nm AuNP conjugates. **c.** His Tagged-15 nm AuNP conjugates. **d.** Distal Network-15 nm AuNP conjugates.[15]

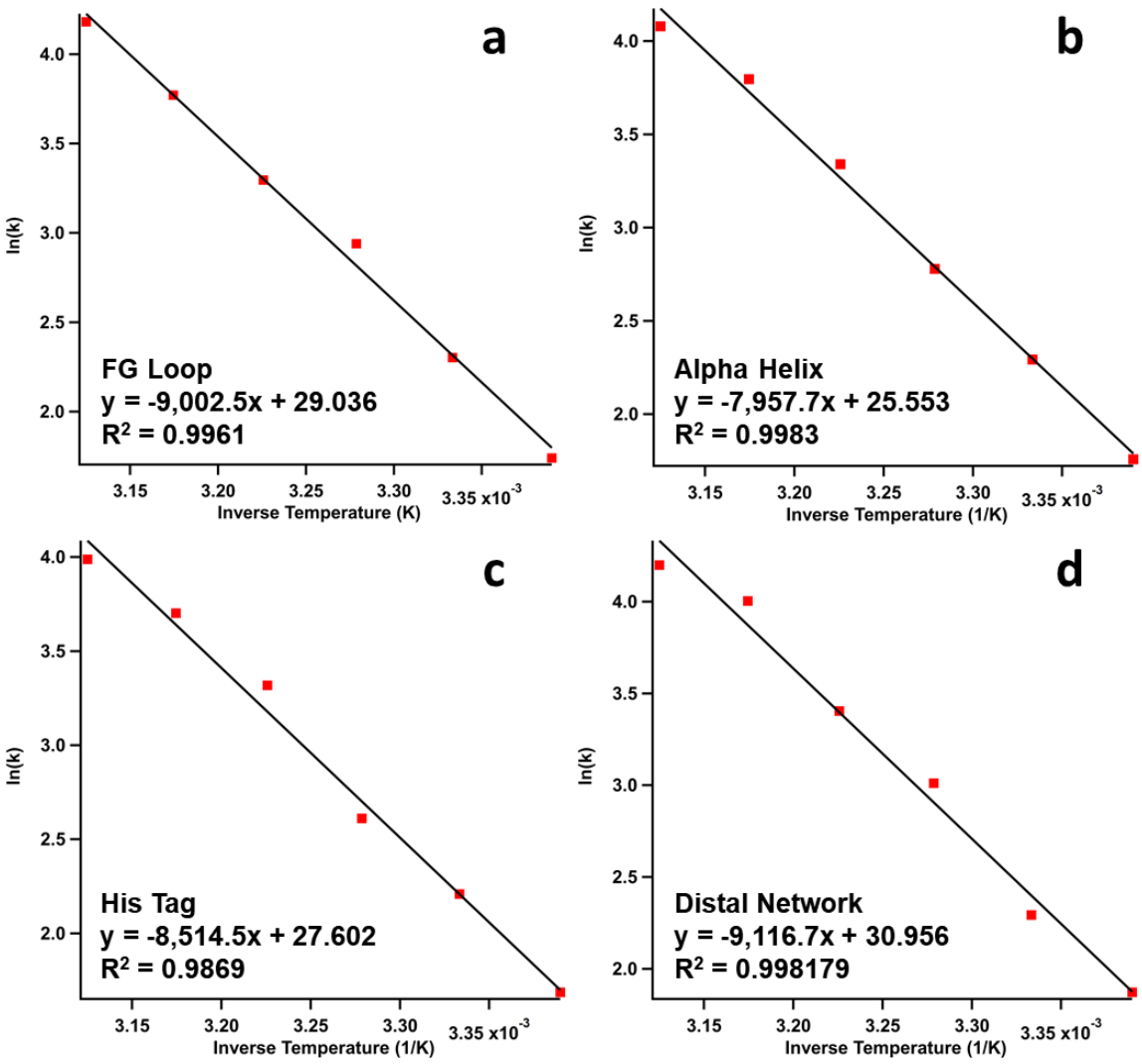

Figure 5.4: Arrhenius Analysis for Free DHFR.

Arrhenius plots of free protein at 22°C, 27°C, 32°C, 37°C, 42°C, and 47°C. **a.** WT DHFR. **b.** FG Loop mutant. **c.** Alpha Helix mutant. **d.** His Tagged mutant.[15]

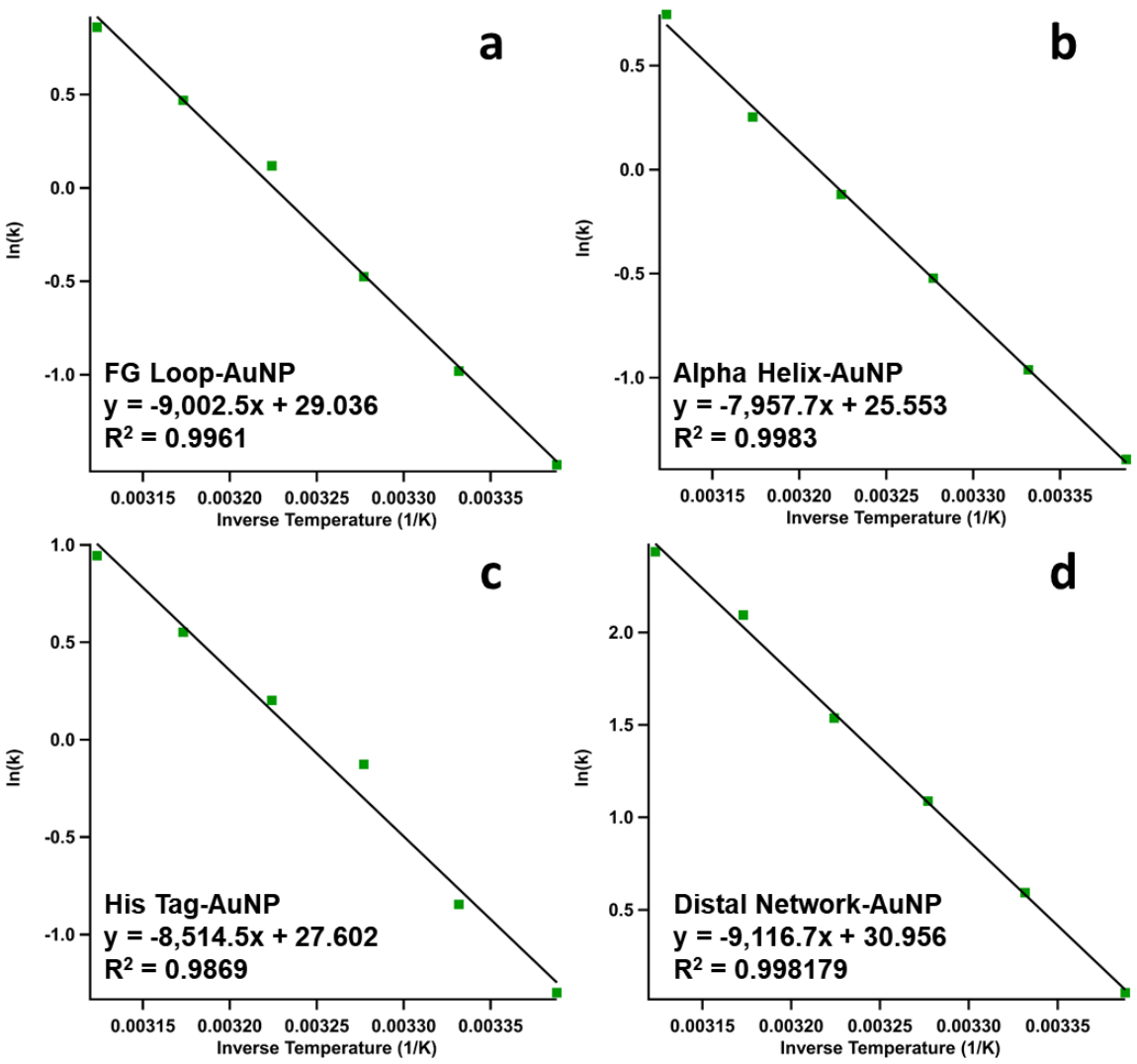

Figure 5.5: Arrhenius Analysis for DHFR-AuNP Conjugates.

Arrhenius kinetics of DHFR-AuNP conjugates. **a.** FG Loop-15 nm AuNP conjugates. E_a = 74.8 kJ/mol. **b.** Alpha Helix-15 nm AuNP conjugates. E_a = 66.2 kJ/mol. **c.** His Tagged-15 nm AuNP conjugates. E_a = 70.8 kJ/mol. **c.** Distal Network-15 nm AuNP conjugates. E_a = 75.8 kJ/mol.[15]

The DHFR-AuNP conjugate activation energies are shown in **Table 5.1**. The activation energies of the conjugates are all similar to each other, and they are also similar to the respective free protein E_a (**Table 5.1**), indicating that there is no substantial difference in bulk heating effects between any of the mutants or their respective conjugates.

From the COMSOL simulations, we see that the heat has dissipated within 2 ns, which means the net increase in temperature is negligible during the duration of enzyme turnover. Therefore, the amount of heat generated is much too small to generate the observed turnover acceleration.

Table 5.1: Activation Energies of DHFR and DHFR-AuNP Conjugates.

Activation Energies for All Free Mutant Enzymes and DHFR-15 nm AuNP Conjugates.[15]

	Activation Energy (kJ/mol)	
Sample Type	**Free Enzyme**	**Enzyme-15 nm AuNP Conjugates**
FG Loop	76.2	74.8
Alpha Helix	74.9	66.2
His Tagged	79.4	70.8
Distal Mutant	77.1	75.8

Activation energies were determined by measurement of activity at 6 different temperatures, with N = 3 for all temperatures.

Section 5-2.3: TEM of Conjugates Before and After Laser Excitation

In order to ensure that the DHFR-AuNP conjugates were not destroyed in the process of the heating experiment, transmission electron microscopy (TEM) measurements were taken of the FG Loop-15 nm AuNP conjugates before and after a typical 40 mW pulsed fs excitation experiment, the potentially most damaging experiment (**Figure 5.6**).

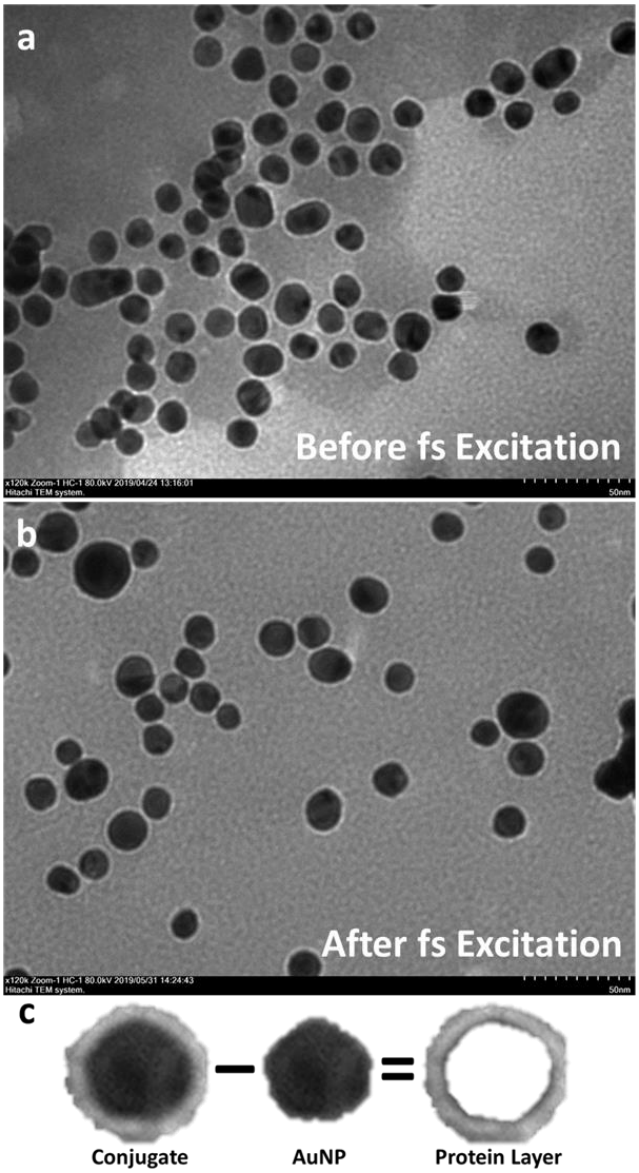

Figure 5.6: TEM Image Analysis Before and After fs Pulsed Excitation.

TEM image analysis of FG Loop-15 nm AuNP conjugates. **a.** Conjugates before fs laser excitation. AuNPs are very electron dense and are the dark spots, which are roughly spherical and measure approximately 14 ± 1.4 nm in diameter. The sample was stained with phosphotungstate, which can be seen as the gray background. The white outline around the AuNPs is the protein layer, which measures 3.48 ± 1.01 nm. **b.** Conjugates after 5 continuous minutes of fs laser excitation. There is no deformation of the AuNPs and the enzyme layer remains intact, indicating that the laser excitation does not damage the conjugates. **c.** Zoom in on a single conjugate to demonstrate protocol for TEM size measurement. Conjugate diameter was measured, then the AuNP diameter was measured and subtracted from the total conjugate diameter to obtain the size of the protein layer.[15]

The conjugates imaged before and after are not identical but instead random samples due to the limitations in that the samples had to be dried on the TEM grid, so a different liquid sample was used in the heating experiment. Therefore, this does not completely rule out the possibility that AuNPs could have been destroyed, but our control experiments show evidence that there was minimal destruction, if any. Before excitation, the TEM images show monodisperse AuNPs with a surrounding monolayer of protein. The layer of protein was measured to be 3.5 nm, which is consistent with the known size of DHFR (**Figure 5.7**). After the fs excitation experiment, the FG Loop-AuNP conjugates appear identical to the before excitation conjugates. The AuNPs appear to not be deformed, and the protein layer remained intact and of identical size.

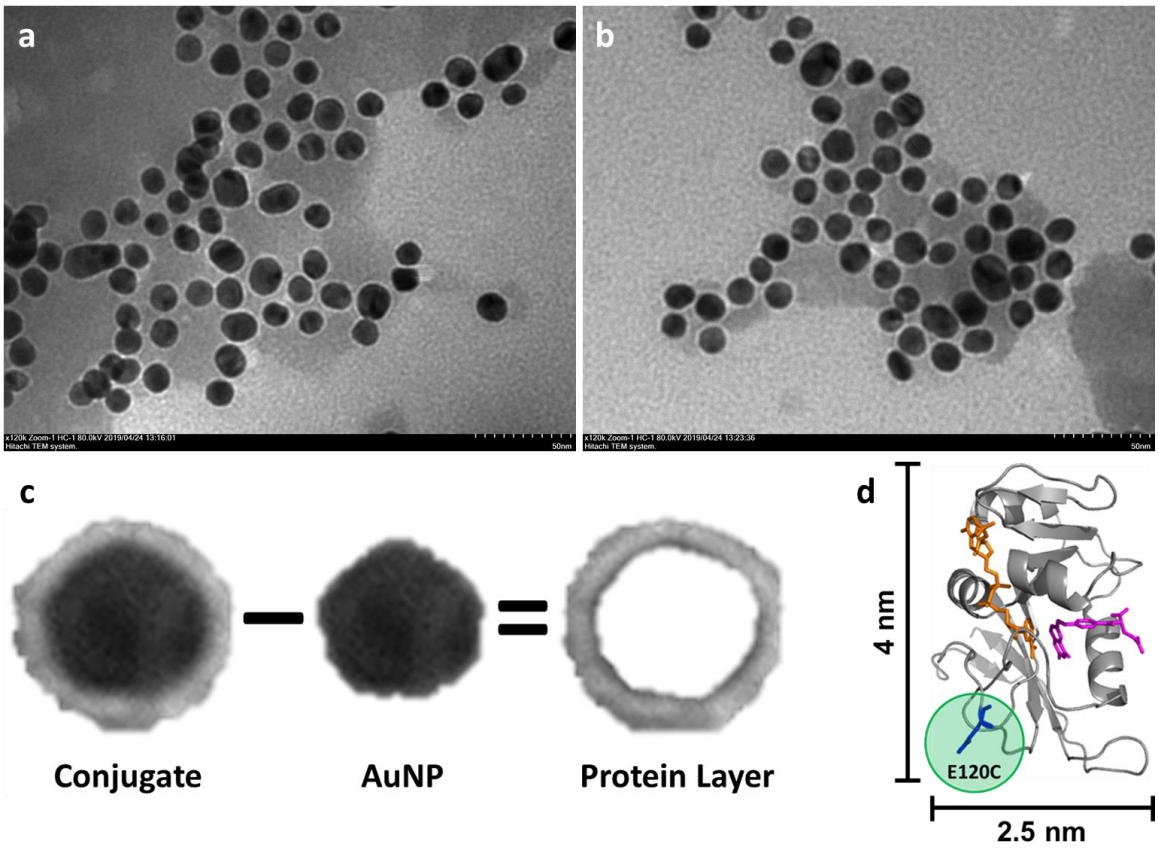

Figure 5.7: Additional TEM Images and Comparison to DHFR Size.

a and b. Additional TEM images of FG Loop-15 nm AuNP conjugates before laser excitation, allowing for the determination of the protein layer size. A total of 208 conjugates were measured. **c.** Process of measuring the size of the protein layer. See below for calculations. **d.** Dimensions of DHFR, showing that the size of the DHFR layer is equivalent to the size of DHFR, indicating the presence of a monolayer of enzyme on the AuNPs.[15]

208 measurements of conjugates and AuNPs from 4 images:

Average conjugate size = 19.82 ± 1.51 nm

Average AuNP size = 12.87 ± 1.35 nm

2x DHFR = Conjugate – AuNP

DHFR Layer = (Conjugate – AuNP) / 2

Average DHFR Layer = 3.48 ± 1.01 nm

This TEM result in conjugation with the Distal Mutant and His Tag controls indicates that the laser does not seem to cause enzymes to unbind from the AuNP surface. With the Distal Mutant and His Tag controls, there was no activity acceleration with any of the laser heating conditions tested. If enzymes were dissociating from the AuNP surface, there would be a rate acceleration with these mutants, especially the His Tagged-AuNP conjugate, as the His Tag is not covalently bound and would more easily unbind from the AuNP surface. Therefore, the observed turnover enhancement in the laser heating experiments is likely not due to unbound enzyme; we think it is due to the dynamics of the enzyme and heating near the network of coupled motions in DHFR.

Section 5-3: Chapter 5 Conclusions

In this chapter, we perform control experiments to demonstrate that the laser heating effects are due to the role of dynamical motions in DHFR catalysis through site-directed heating via attached AuNPs. AuNPs are biologically compatible heaters that allow a large amount of energy to be put into the protein site-specifically. The energy of a single 527 nm photon is 227 kJ/mol, and the activation barrier of DHFR is approximately 75 kJ/mol based on our Arrhenius analysis, so there is a lot of energy being put into the protein from the AuNP. A lot of the energy from the AuNP gets dissipated, but it appears that the enzyme has a way of coupling some of that energy to the active site, specifically through the network of coupled motions. The key is that the energy needs to be input into the network and on the appropriate timescale, such that the coupling outcompetes the energy dissipation. Energy transport and dissipation in proteins is known to occur on the 100s of ps timescale,[1-4] and in DHFR, MD simulations have shown that correlated motions occur

on a timescale up to at least 10 ns.[16] The input of the heat energy must also be on a similar timescale. The timescale of energy dissipation from AuNPs or gold nanorods (AuNRs) to the surrounding solution has been measure with time-resolved infrared spectroscopy, and it is known to be on the 10s of ps to 400 ps depending on the AuNP or AuNR size and the capping ligand, be it citrate, a thiol, or a protein.[5, 6] For the system used here, the energy dissipation time is likely on the slower end of this range due to AuNP size and the capping ligands being enzymes. Additionally, the protein motions that are excited must also be on this timescale. In general, all proteins have an energy landscape,[17-19] and the usual implication of rate acceleration is a consequence of lowering the transition barrier. However, if the catalytic landscape is rough, such that there are multiple peaks and valleys,[17] some of the population could become trapped in local minima that have high barriers to reaction. The input of heat into a specific part of the protein structure might help transfer the population to more reactive conformations, or basins on the landscape from which the transition barrier is much lower. Thus, if this is the case, we are speeding up the search for reactive conformations by pushing the system from trapped unreactive states by the site-specific addition of energy.

We showed that the rate acceleration is not due to bulk heating with the combination of COMSOL simulations and temperature-dependent kinetics. TEM imaging in conjunction with the Distal Mutant and His Tagged mutant controls demonstrated that there was no observed unbinding of enzyme or deformation of AuNPs.

Thus, we demonstrated important advances and new approaches for monitoring the effect of site-directed protein attachment on AuNPs, including heat transfer via AuNPs to attached enzymes. This can be broadly applied to other enzyme systems, especially those

to which have known networks of motions, such as Cyclophilin A and Triose Phosphate Isomerase.[20-22] This type of work regarding heat flow through enzymes can change how we study enzyme dynamics, providing experimental evidence for energy transfer through networks of motions in enzymes and furthering our knowledge of the role of motions in enzyme catalysis.

Section 5-4: Chapter 5 References

1. Hill, J. R.; Dlott, D. D.; Rella, C. W.; Peterson, K. A.; Decatur, S. M.; Boxer, S. G.; Fayer, M. D., Vibrational Dynamics of Carbon Monoxide at the Active Sites of Mutant Heme Proteins. *J. Phys. Chem.* **1996,** *100* (29), 12100-12107.

2. Fujisaki, H.; Straub, J. E., Vibrational energy relaxation in proteins. *Proc. Natl. Acad. Sci. U.S.A.* **2005,** *102* (19), 6726-6731.

3. Leitner, D. M., Energy flow in proteins. *Annu. Rev. Phys. Chem.* **2008,** *59*, 233-59.

4. Xie, A.; Meer, A. F. G. v. d.; Austin, R. H., Excited-State Lifetimes of Far-Infrared Collective Modes in Proteins. *Phys. Rev. Lett.* **2001,** *88* (1), 018102.

5. Hu, M.; Hartland, G. V., Heat Dissipation for Au Particles in Aqueous Solution: Relaxation Time versus Size. *J. Phys. Chem. B* **2002,** *106* (28), 7029-7033.

6. Nguyen, S. C.; Zhang, Q.; Manthiram, K.; Ye, X.; Lomont, J. P.; Harris, C. B.; Weller, H.; Alivisatos, A. P., Study of Heat Transfer Dynamics from Gold Nanorods to the Environment via Time-Resolved Infrared Spectroscopy. *ACS Nano* **2016,** *10* (2), 2144-2151.

7. Fan, Y.; Cembran, A.; Ma, S.; Gao, J., Connecting Protein Conformational Dynamics with Catalytic Function As Illustrated in Dihydrofolate Reductase. *Biochemistry* **2013,** *52*, 2036-2049.

8. Helbing, J.; Devereux, M.; Nienhaus, K.; Nienhaus, G. U.; Hamm, P.; Meuwly, M., Temperature Dependence of the Heat Diffusivity of Proteins. *J. Phys. Chem. A* **2012,** *116* (11), 2620-2628.

9. Reddish, M. J.; Peng, H.-L.; Deng, H.; Panwar, K. S.; Callender, R.; Dyer, R. B., Direct Evidence of Catalytic Heterogeneity in Lactate Dehydrogenase by Temperature Jump Infrared Spectroscopy. *The Journal of Physical Chemistry B* **2014,** *Articles ASAP*.

10. Glowacki, D. R.; Harvey, J. N.; Mulholland, A. J., Taking Ockham's razor to enzyme dynamics and catalysis. *Nat. Chem.* **2012,** *4* (3), 169-176.

11. Arora, K.; Brooks, C. L., Functionally Important Conformations of the Met20 Loop in Dihydrofolate Reductase are Populated by Rapid Thermal Fluctuations. *JACS* **2009,** *131* (15), 5642-5647.

12. Hassan, S.; Schade, M.; Shaw, C. P.; Levy, R.; Hamm, P., Response of villin headpiece-capped gold nanoparticles to ultrafast laser heating. *J. Phys. Chem. B* **2014,** *118* (28), 7954-62.

13. Schade, M.; Moretto, A.; Donaldson, P. M.; Toniolo, C.; Hamm, P., Vibrational Energy Transport through a Capping Layer of Appropriately Designed Peptide Helices over Gold Nanoparticles. *Nano Lett.* **2010,** *10* (8), 3057-3061.

14. Blankschien, M. D.; Pretzer, L. A.; Huschka, R.; Halas, N. J.; Gonzalez, R.; Wong, M. S., Light-Triggered Biocatalysis Using Thermophilic Enzyme-Gold Nanoparticle Complexes. *ACS Nano* **2013,** *7* (1), 654-663.

15. Kozlowski, R., Driving Enzyme Dynamics with Light in Dihydrofolate Reductase-Gold Nanoparticle Conjugates. *Nat. Chem.* **to be submitted in 2020**.

16. Radkiewicz, J. L.; Brooks III, C. L., Protein Dynamics in Enzymatic Catalysis: Exploration of Dihydrofolate Reductase. *J. Am. Chem. Soc.* **2000,** *122*, 225-231.

17. Benkovic, S. J.; Hammes, G. G.; Hammes-Schiffer, S., Free-energy landscape of enzyme catalysis. *Biochemistry* **2008,** *47* (11), 3317-3321.

18. Swint-Kruse, L.; Fisher, H. F., Enzymatic reaction sequences as coupled multiple traces on a multidimensional landscape. *Trends Biochem. Sci.* **2008,** *33* (3), 104-112.

19. Boehr, D. D.; McElheny, D.; Dyson, H. J.; Wright, P. E., The dynamic energy landscape of dihydrofolate reductase catalysis. *Science* **2006,** *313* (5793), 1638-42.

20. Eisenmesser, E. Z.; Millet, O.; Labeikovsky, W.; Korzhnev, D. M.; Wolf-Watz, M.; Bosco, D. A.; Skalicky, J. J.; Kay, L. E.; Kern, D., Intrinsic dynamics of an enzyme underlies catalysis. *Nature* **2005,** *438*, 117 – 121.

21. Konuklar, F. A. S.; Aviyente, V.; Haliloğlu, T., Coupling of structural fluctuations to deamidation reaction in triosephosphate isomerase by Gaussian network model. *Proteins* **2006,** *62*, 715-727.

22. Nashine, V. C.; Hammes-Schiffer, S.; Benkovic, S. J., Coupled motions in enzyme catalysis. *Curr. Opin. Chem. Biol.* **2010,** *14* (5), 644-651.

Chapter 6 – Conclusions

Although the contribution of protein motions to enzymatic catalysis has been heavily studied both experimentally and computationally, experimental evidence reporting on the exact role of enzyme dynamics in catalysis is unknown. In this dissertation, we presented a new methodology to probe the dynamic motions in enzymes during catalysis and determine if the motions represent preferred energy pathways. To interrogate the connection between enzyme catalytic motions and preferred energy pathways, dihydrofolate reductase was conjugated to AuNPs via site-specific bioconjugation of a cysteine residue to the AuNP.

The first steps in this process were designing DHFR mutants and determining how to conjugate the enzyme to gold nanoparticles. Single cysteine mutants of DHFR were engineered, where the site-specific locations were either near the network of coupled motions or distal to the network. A Histidine Tagged mutant with no cysteine residues was also used as a control conjugate, as the His Tag strongly associates with the AuNPs. The single cysteine mutants underwent a TEV cleavage to cleave the His Tag, and then they were covalently conjugated to AuNPs with diameters of 5 nm, 15 nm, and 30 nm, which each provided different surface curvatures. Binding of different regions of the protein was investigated: on the FG loop versus a rigid alpha helix. An integrated characterization methodology was developed and included SDS-PAGE, UV/Vis absorbance spectrophotometry, Dynamic Light Scattering, and a novel methodology for accurate determination of low protein concentration on AuNPs. An accurate determination of both protein and AuNP concentration in conjugate samples allowed for the precise calculation

of surface coverage, which was found to be related to the surface curvature of the AuNP. We presented an integrated approach to characterize protein-AuNP conjugates, where we addressed the currently lacking knowledge of surface coverage of protein on AuNPs. Further, this unique methodology is important for understanding functionality in protein-AuNP bioconjugates, such as enzyme activity.

These conjugates were then used in the study of heat flow through enzymes via laser excitation of AuNPs. Heat transfer was initiated by excitation of the AuNP's SPR band at 527-531 nm with both continuous wave and pulsed laser excitations. Enzyme activity was monitored as a function of the protein attachment site (distance to/from the network of coupled motions) on the AuNP, as well as of the timescale of laser pulsing. Enzyme activity when attached to the AuNP close to the network (on the FG loop) was accelerated when excited by the pulsed lasers. When attached near the cofactor binding site network residue E101 (on an Alpha Helix), turnover was accelerated to a lesser extent. There was a greater degree of acceleration with fs pulsed laser than with ns pulses in both mutants. There was no rate acceleration when attached away from the network (Distal Mutant) or via the histidine tag (also away from the network). There was no rate acceleration observed for any attachment site with the continuous wave excitation. When the excitation timescale was fast enough, the heat flow into the protein affected the enzyme motions in catalysis, which are likely the motions involved in the search for reactive conformations, and the heat eventually thermalizes after these motions take place.

Through multiple controls, we demonstrated that the effect of rate acceleration is likely due to the enzyme's dynamic motions and energy pathways. The Distal Mutant and His Tagged mutant demonstrate that there is no rate acceleration when the enzyme is not

attached near the network of coupled motions in DHFR. The CW laser excitation shows that the laser excitation must be pulsed in order to observe rate acceleration upon excitation. Temperature-dependent kinetics in conjunction with COMSOL simulations and the distal mutant controls proved that the rate acceleration is not due to the bulk heating of solution. Further, TEM imaging along with the distal network mutant controls demonstrated that there was no or minimal unbinding of enzyme or deforming of AuNPs. Therefore, we determined that site-specific heating of DHFR attached to AuNPs through different attachment sites, being near or distal to the network of coupled motions in DHFR, can lead to new knowledge on dynamics of DHFR. Overall, this work demonstrates a useful methodology for studying protein motions in enzyme catalysis, allowing us to investigate energy pathways in catalysis.